DESIGN AND REALIZATION OF A BROAD BAND ANTENNA LOADED WITH A METAMATERIAL-INSPIRED LENS FOR SUBSURFACE MICROWAVE IMAGING APPLICATIONS

A THESIS SUBMITTED TO

THE GRADUATE SCHOOL OF NATURAL AND APPLIED SCIENCES

OF

MIDDLE EAST TECHNICAL UNIVERSITY

BY

ÖMER YEŞİLYURT

IN PARTIAL FULFILLMENT OF THE REQUIREMENTS

FOR

THE DEGREE OF MASTER OF SCIENCE

IN

ELECTRICAL AND ELECTRONICS ENGINEERING

FEBRUARY 2019

Approval of the thesis:

DESIGN AND REALIZATION OF A BROAD BAND ANTENNA LOADED WITH A METAMATERIAL-INSPIRED LENS FOR SUBSURFACE MICROWAVE IMAGING APPLICATIONS

submitted by **ÖMER YEŞİLYURT** in partial fulfillment of the requirements for the degree of **MASTER OF SCIENCE in ELECTRICAL AND ELECTRONICS ENGINEERING Department, Middle East Technical University** by,

Prof. Dr. Halil Kalıpçılar
Dean, Graduate School of **Natural and Applied Sciences** _____

Prof. Dr. Tolga Çiloğlu
Head of Department, **Electrical and Electronic Eng.** _____

Prof. Dr. Gönül Turhan Sayan
Supervisor, **Electrical and Electronic Eng., METU** _____

_____

Examining Committee Members:

Prof. Dr. Gülbin Dural
Electrical and Electronics Eng. Dept.,METU _____

Prof. Dr. Gönül Turhan Sayan
Electrical and Electronic Eng., METU _____

Prof. Dr. Nilgün Günalp
Electrical and Electronics Eng. Dept., METU _____

Prof. Dr. Asım Egemen Yılmaz
Electrical and Electronics Eng. Dept., Ankara University _____

Prof. Dr. Özlem Özgün
Electrical and Electronics Eng. Dept., Hacettepe University _____

Date: 22.02.2019

I hereby declare that all information in this document has been obtained and presented in accordance with academic rules and ethical conduct. I also declare that, as required by these rules and conduct, I have fully cited and referenced all material and results that are not original to this work.

Name, Surname: Ömer Yeşilyurt

Signature:

ABSTRACT

DESIGN AND REALIZATION OF A BROAD BAND ANTENNA LOADED WITH A METAMATERIAL-INSPIRED LENS FOR SUBSURFACE MICROWAVE IMAGING APPLICATIONS

Yeşilyurt, Ömer

Master of Science, Electrical and Electronics Engineering

Supervisor: Prof. Dr. Gönül Turhan Sayan

February 2019, 119 pages

Ultra-wideband antennas are critical sensors for microwave imaging. In this work, radiation performance of an antipodal Vivaldi antenna is enhanced by using a broadband metasurface lens structure in 1-6 GHz bandwidth. Radiation pattern for the lens integrated antenna is more directive due to electromagnetic properties of the metasurface lens. In order to create such a lens, electrically responsive metamaterial unit cells with high effective permittivity values are designed. As we want to obtain a broadband antenna performance, metamaterial unit cell dimensions are adjusted to avoid the resonance regions of the metasurface over the desired operation bandwidth of the antenna. Overall lens structure is etched over the same substrate containing the antipodal Vivaldi antenna resulting in a compact design. Far-field radiation patterns indicate that more directive beam is radiated from the antenna with metasurface lens. Measurement and simulation results show that directivity is increased considerably without affecting the efficiency characteristics of the antenna. Microwave image of a shallowly buried conducting object is constructed by using with metasurface integrated antenna and also by using the conventional antipodal Vivaldi antenna as sensors. Two-dimensional microwave images are constructed by using the total energy values of the time signals measured at each spatial sampling point. Due to its more directive radiation

pattern, the images obtained by the antenna with metasurface lens are observed to have better resolution.

Keywords: metasurface, antipodal Vivaldi Antenna, high directivity, ultra-wideband, microwave imaging

ÖZ

METAMALZEMELERDEN ESİNLENİLMİŞ LENS DESTEKLİ GENİŞ BANTLI BİR ANTENİN TASARIMI, GERÇEKLENMESİ VE YERALTI MİKRODALGA GÖRÜNTÜLEME UYGULAMALARINDA KULLANIMI

Yeşilyurt, Ömer

Yüksek Lisans, Elektrik ve Elektronik Mühendisliği

Tez Danışmanı: Prof. Dr. Gönül Turhan Sayan

Şubat 2019, 119 sayfa

Ultra geniş bantlı antenler, mikrodalga görüntüleme için kritik sensörlerdir. Bu çalışmada, bir antipodal Vivaldi anteninin radyasyon performansı, 1-6 GHz bandı içerisinde, geniş bant metayüzey lens yapısı kullanılarak geliştirilmiştir. Lens entegre edilmiş antenin ışınım deseni, metayüzey lensinin elektromanyetik özellikleri nedeniyle daha yönlü hale gelmiştir. Bu lens yapısını oluşturmak için, yüksek dielektrik katsayısı değerlerine sahip, elektrik alan ile uyarılan metamateryel birim hücreler tasarlanmıştır. Geniş bantlı anten davranışı hedeflendiği için, istenen anten çalışma bandı üzerinde metayüzeyin rezonansa girmeyeceği şekilde metamalzeme birim hücre boyutları ayarlanmıştır. Genel lens yapısı, antipodal Vivaldi anteni de içeren aynı taban malzemesi üzerine yerleştirilmiş ve kompakt profilli bir tasarım ortaya çıkmıştır. Uzak alan ışınım deseni, metayüzey lense sahip antenden daha direktif bir ışınımın yayıldığını göstermiştir. Ölçüm ve simülasyon sonuçları, metayüzey lensin tasarıma dahil edilmesinden dolayı antenin verimlilik özelliklerinin etkilenmediğini ve ışınım yönlülüğün önemli ölçüde arttığını göstermektedir. Toprak yüzeyinin hemen altına gömülü iletken nesnelerin mikrodalga görüntüleri metayüzey entegre edilmiş anten ve standart antipodal Vivaldi antenin sensor olarak kullanılması ile iki ayrı biçimde elde edilmiştir. İki boyutlu mikrodalga görüntüleri, her bir uzaysal örnekleme noktasında ölçülen zaman sinyalinin toplam enerji değeri kullanılarak elde edilmiştir. Metayüzey lensli antenin

ışınım yönlülüğünün daha iyi olması nedeniyle, bu anten ile elde edilen görüntünün daha iyi bir çözünürlüğe sahip olduğu gözlemlenmiştir.

Anahtar Kelimeler: Metayüzey, Antipodal Vivaldi anten, yüksek yönlülük,ultra geniş bant, mikrodalga görüntüleme

To my brothers

ACKNOWLEDGMENTS

I would like to offer my sincere gratitude to my supervisor, Prof.Dr.Gönül Turhan Sayan for her insightful and invaluable guidance over my research career as well as for this thesis. I could not complete this work without her endless support and encouragement.

I would like to thank to Prof.Dr. Mustafa Kuzuoğlu, Prof.Dr. Tuncay Birand and Prof. Sencer Koç. Their excellent in course teachings and contributions to my research constitutes important part of my research.

I am very grateful to my fellow researchers at METU EE. I would like to thank Kadir Üstün and Mesut Doğan for their help and contributions to my academic career. Their personal guidance and support facilitated my humble endeavors to pursue a career in science.

I am very grateful to my colleagues Alper Ünal, Alp Manyas and Doğancan Eser. Their endless support and tolerance enabled me to complete my work. I would like to thank Alper Ünal specially for his support and teachings which enabled me to pursue a career in electromagnetics research both in academia and industry.

I would like to acknowledge Meteksan Defence Industries for financial and engineering support to my research. Without help and work place tolerance of Meteksan, I would not be able to complete my research.

I would like thank and offer my sincerest gratitude to my parents, Mehmet and Cemile Yeşilyurt, who took care of me all my life and throughout my MsC training as well. Without their help, I could not overcome the hard times I had endured in the last couple years.

TABLE OF CONTENTS

LIST OF TABLES

TABLES

LIST OF FIGURES

FIGURES

CHAPTER 1

INTRODUCTION

1.1. Metamaterials

Metamaterials are artificial structures that can have properties that are not available for natural materials. In terms of electromagnetic (EM) properties, metamaterials can bring extraordinary features into practice such as zero/near zero and negative constitutive parameters. These sort of properties lead to several exciting physical phenomena such as negative refraction, evanescent wave propagation, and anti-parallel group and phase velocities. In his groundbreaking work, Russian physicist Victor Veselago introduced electrodynamics of a hypothetical medium having simultaneously negative permittivity and permeability values [1]. He also pointed out the implications of such media such as reverse-Cerenkov radiation, backward wave propagation, and inverse Doppler effect. For nearly three decades, horizon signaled in Veselago's work remained unexplored. Pendry et al. realized the first medium having negative permittivity below plasma frequency by using wires aligned periodically inside a volume [2]. Later, Pendry's team created the first medium with the negative magnetic permeability below plasma frequency with split ring resonator as unit cells instead of wires. Both these works enabled the realization of negative index material in microwave regions which then applied to numerous microwave component [3]. Smith et al. combined individual unit cell topologies to suggest the first double negative index metamaterial where effective permittivity and permeability of the medium are negative [4]. Experimental verification of the first negative index metamaterial was made possible by Shelby et. al [5] where the intersection of the negative band for the two constitutive parameters was corresponding to a narrow bandwidth [5]. In a prism-shaped medium with a negative

index of refraction was utilized to verify findings of [4] by measuring the deviation of the propagation direction of an EM field in the microwave frequency band.

After verification of artificial material with such properties, researchers around the world had turned their faces to applications of this extraordinary phenomena. Initially, metamaterials with different effective EM response are studied such as single/double negative index materials and zero/near zero-index materials [6,7,8-9,10,11]. Cloaking devices, lenses going beyond optical limits and wideband absorbers are exciting applications of the metamaterials [12, 13, 14, 15, 98, 99].

1.2. Metamaterials for Antenna Applications

The advent of metamaterials has led to the development and improvement of numerous microwave components including antennas in terms of performance characteristics such as radiation pattern, efficiency, operation bandwidth and physical size [16, 100, 101]. Since the physical size of the antenna is the main limitation for the lower end of operation frequency, metamaterials can be incorporated into the antenna system to reduce their size by affecting their near-field characteristics. Many other applications deal specifically with alteration of the radiation pattern for far field of the antenna systems [17]. Several major research pathways in metamaterial applications to antennas are examined in the rest of this chapter.

A metamaterial shell consisting of negative index unit cells is used to increase the radiation efficiency and the operating bandwidth of the electrically small antennas [18]. It has been shown that such a metamaterial shell can achieve complete matching of the antenna to 50-ohm port without any matching circuitry [19, 20]. An electrically small dipole antenna is enclosed by a negative permeability material in [19]. Excited dipole radiates electric field into free space enclosed by the shell which leads to a capacitive behavior. The electric field driven by dipole also excites the shell which exhibits an inductive characteristic due to the negative permittivity of the

shell. Overall, metamaterial shell acts as an RLC resonator by interacting with the antenna in the near the field in the manner described before. The resonance frequency of the whole antenna system is;

$$f_r = \frac{1}{2\pi\sqrt{L_r C_r}} \tag{1}$$

C_r and L_r are effective capacitance and inductance respectively. The result obtained with the negative permeability shell allows the antenna to operate efficiently at larger wavelengths. Similar research was carried out with negative permeability metamaterial in which an enclosing shell is constructed around the antenna [21]. A negative permeability shell is constructed around an electrically small loop antenna to achieve matching without an external matching network. Since losses present in each unit cell structure were considerably large, hypothesized increase in the efficiency was not achieved. In[22], it is proposed that the Chu lower bound [23] can be achieved by loading a small spherical magnetic dipole antenna with very large permeability metamaterial. In essence, magnetic energy stored inside the enclosing shell would be reduced to zero which enables the antenna to reach Chu lower bound limit. Although bright ideas and improvements are presented theoretically, there are several obstacles in the way of practical applications. Putting aside fabrication difficulties of such physically small unit cells, losses related with each unit cell is high and offer very narrow bandwidth of operation. Only after negating loss effects, one can realize practical negative permittivity/permeability metamaterial shells for antenna systems.

Besides dispersion models, the transmission line model is a widely utilized method to characterize metamaterial structures. Symmetrical metamaterial unit cells can be modeled mathematically by implementing the right-handed effect into a left-handed circuit. In Fig 1.1, a composite right/left-handed metamaterial unit cell is modeled with the equivalent circuit model. The unit cell allows wave propagation in a backward and forward direction.

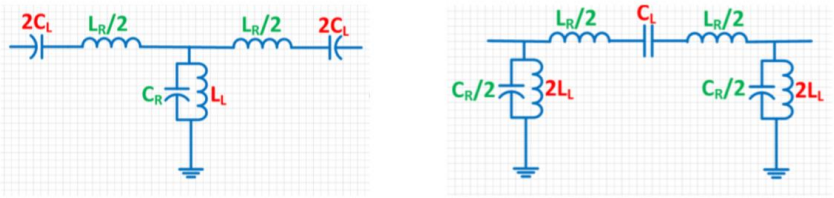

Figure 1.1. Equivalent transmission line circuit for composite right-/left-handed unit cells, T-type model (left), π-type mode (right)

The operation mode of the composite right-/left-handed transmission line antenna are zeroth and negative order resonance modes. Zeroth resonance corresponds to a frequency value which is not constrained by the physical size of the antenna. Fig 1.2 illustrates a composite right/left-handed transmission line antenna. Four unit cells operating in zeroth-order resonance constitutes the antenna. Antenna provided a return loss of 11 dB at 4.88 GHz which corresponds to a size reduction of 75% in comparison with the conventional patch with identical substrate [24].

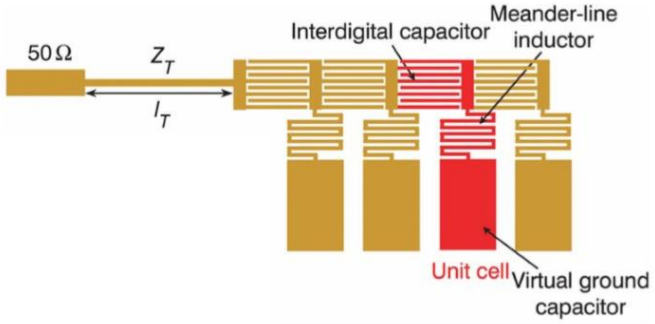

Figure 1.2. Composite right-/left-handed transmission line antenna operating at zeroth order resonance mode

Mushroom type metamaterial structure is also a widely used composite right-/left-handed structure. In this type of engineered material, vias connecting patches and ground plane provides inductance effect while the capacitive effect is produced in the spaces between patches. Figure 1.3 shows the zero-resonance-mode mushroom structure included in an antenna system.

Considerable size reduction is achieved by the antenna with the mushroom structure at 3.38 GHz with a very narrow bandwidth of 1% having a return loss of -12.34 dB [25]. Overall system size is 0.167λ x 0.167 λ x 0.018 λ of the operation wavelength. Further improvement has been reported in which the size of the antenna-mushroom structure is reduced to 0.104 λ x 0.104 λ x 0.056 λ by incorporating additional lumped elements [26].

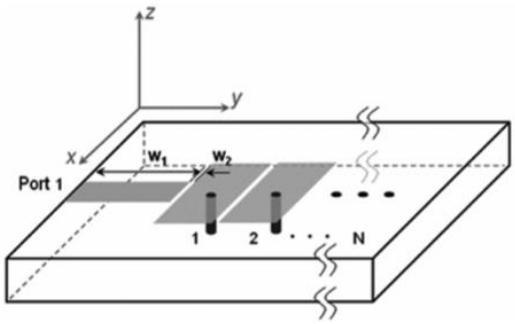

Figure 1.3. Mushroom zeroth order resonance antenna [26]

A reactive impedance surface is placed under the antenna to improve the radiation efficiency of a patch antenna. Measurement results display a resonance frequency of 2.58 GHz for the radiator with an electrical size of 0.1777 λ x 0.181 λ x0.025 λ. The radiation efficiency of the overall system reaches up to 72% inside fractional operation bandwidth of 4.5 percent, while obtaining a peak gain of 3dBi [27].

Metasurfaces are structures consisting of a periodic array of metamaterial unit cells placed on a single surface. Microwave components and antennas have found novel design applications [28,29,30] with the use of metasurfaces such as planar photonic band gap structures [31,29], reactance impedance surface[81-83] and electromagnetic band gap structures [28,32].

Periodic unit cells having bandgap between two consecutive resonant modes create a metasurface called electromagnetic band gap structure. This structure, also known as the Artificial Magnetic Conductor, does not allow surface waves with the frequency in the band gap to propagate. It has been shown that smoother radiation

pattern and enhancement in the front-to-back ratio can be achieved through the use of EBG structure. In [33], a reactive impedance surface is applied to a patch antenna. Metasurface is placed between the patch and ground plane. Antenna miniaturization is reported alongside with augmentation in operation bandwidth and radiation characteristics. The metasurface substrate is etched over trans-tech MCT-25 (with 4mm substrate thickness) which has the dielectric constant of 25. At 1.92 GHz operation frequency, overall antenna system had the gain of 4.5 dBi, radiation efficiency of 90% and fractional operation bandwidth of 6.7% with a microstrip patch having electrical size of $0.102\lambda \times 0.128\lambda \times 0.038\lambda$ [33].

Ferisidis et al. proposed a low profile patch antenna loaded with metasurfaces [34] where an artificial magnetic conductor covers the top surface of the patch while a partially reflective surface is located 0.25 wavelength away from the artificial magnetic conductor surface. Thus, these metasurfaces resulted in a cavity with half of the size relative to the conventional cavity. Measurement results indicate 19 dBi gain with artificial magnetic conductor and partially reflective surface area of $7.1\lambda \times 7.1\lambda$ and $5\lambda \times 5\lambda$ respectively inside 2% fractional operation bandwidth.

1.3. Metamaterial Applications for Vivaldi Antenna

Vivaldi antenna is one of the most popular endfire antennas because of its ultra-wideband operation, low cost, compact size and medium directivity characteristics [35]. These attributes enable its use in a wide spectrum of applications including wireless communication, microwave imaging, radar et cetera. Despite its attractive qualities, Vivaldi antenna may experience undesired effects for ultra-wideband operation such as split/tilted main beam and gain decrease with increasing frequency as suggested in [36].

Several types of metamaterial structures have been incorporated into Vivaldi antennas to increase the performance of the radiator as well as solving problems mentioned beforehand. Zero index metamaterial in one particular direction (anisotropic material) is applied to enhance the gain of the Vivaldi radiator. The

gain increment of 3.8 dBi is reported in the operation bandwidth of 9.5-10.5 GHz bandwidth [37]. The fractional bandwidth over which gain enhancement takes place is relatively narrow due to the resonant behavior of the unit cells near-zero index region. Double negative index metamaterial is inserted perpendicularly into the Vivaldi antenna substrate in [38]. Experimental results suggested an increase in the gain up to 4 dBi in the operation bandwidth of 6.5-20 GHz. Despite its wideband operation, the overall antenna system is electrically large concerning the lower end of the operation bandwidth (6.5 GHz) which is $2.08\lambda \times 1.04\lambda \times 0.69\lambda$. Unfortunately, metamaterial characterization methods used in these works do not provide desired results near and after resonance point. Presented constitutive parameter results conflict with the 2nd law of thermodynamics as to be elaborated in Chapter 2. Therefore, the physical mechanism that causes antenna gain increase is unclear for these studies.

In this thesis, a broad band antenna loaded with a metasurface lens is designed, fabricated and measured. In Chapter 2, design and characterization of an antipodal Vivaldi antenna is investigated. Underlying theory of tapered slot antennas and simulation results for the designed Vivaldi antenna are presented. In Chapter 3, different metamaterial unit cell topologies are designed and simulated. Using the metamaterial unit cells, a broad band metasurface lens is realized. Simulation results for the antipodal Vivaldi antenna loaded with the metasurface lens are presented. In Chapter 4, fabrication methods and measurement results of the conventional and metasurface loaded antipodal Vivaldi antenna are given. In addition, two dimensional (2-D) microwave images of buried targets are retrieved experimentally by the designed antennas. In Chapter 5, overall conclusions are presented. The chapter is concluded with a brief discussion on the future work.

CHAPTER 2

THEORY, DESIGN AND CHARACTERIZATION OF VIVALDI ANTENNA

2.1. Tapered Slot Antennas

Traveling wave antennas are characterized by their current or voltage distribution where they travel through the antenna instead of creating standing waves. Inherently, traveling wave antennas are non-resonant due to their current distribution across the radiator [39]. Traveling waves are either reflected or partially absorbed by a matched termination at the end of the structure. An electrically long wire antenna terminated by a matched load is a typical traveling wave structure as shown in Figure 2.1.

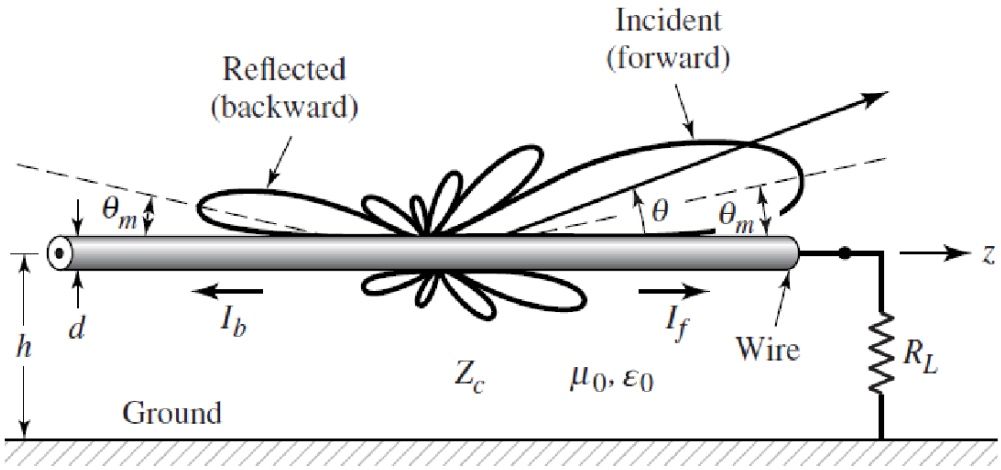

Figure 2.1. The radiation pattern of long wire antenna with a matched termination

Traveling wave antennas are divided into two groups in terms of the traveling wave's phase velocity, namely fast and slow wave structures. Waves traveling across fast wave structures possess phase velocity higher than the speed of light in a vacuum whereas waves inside slow wave structure have phase velocity lower than

light in vacuum. Tapered slot antennas are a type of surface wave antennas. Surface wave radiators are generally recognized as slow-wave structures where radiation takes place at curvatures and discontinuities alongside the radiator. A wave traveling across the antenna must be interrupted by the aforementioned physical imperfections along the whole structure to radiate. These types of antennas are end-fire radiators where electromagnetic waves are launched from the end of the traveling wave's path [40].

Few characteristics mark tapered slot antennas. Low profile, low weight, and ease of fabrication are inherent physical features for these types of antennas. Broadband operation and compatibility with integrated microwave circuits make them suitable for many applications including microwave imaging and ultra-wideband communications.

2.1.1. Radiation Characteristics of Tapered Slot Antennas

Tapered slot antennas can be manufactured by etching slot line over a dielectric material. Gap across the sides of slot line widens throughout its length. EM waves traveling through separation of metallizations inside antenna are radiated at the end of the substrate thus resulting in end-fire radiation. Electric field lines are formed between metal parts of the radiator as depicted in Figure 2.2. Therefore, one can easily conclude that E-Plane of tapered slot antennas is parallel to substrate material. As expected, magnetic field lines are perpendicular to electric field lines thus H-Plane of these structures are perpendicular to the substrate. Dielectric constant and thickness of substrate material, taper profile and electrical size are key physical features deciding the radiation pattern of TSAs, since guided wavelength inside antenna structure is dependent on these physical features. Antenna radiation mode (traveling wave or resonant) and directivity characteristics critically depend upon the ratio of antenna length (L) and guided wavelength. Also, electrical size and substrate properties have a direct impact over radiation pattern, side-lobe levels and cross-

polarization of TSA. When designed properly, TSA can operate over considerably large bandwidths with moderate gain and narrow beamwidths thanks to its traveling wave properties. E and H-plane radiation patterns are nearly symmetric over broad frequency bands. The polarization of TSAs is generally linear for conventional structures. [41]

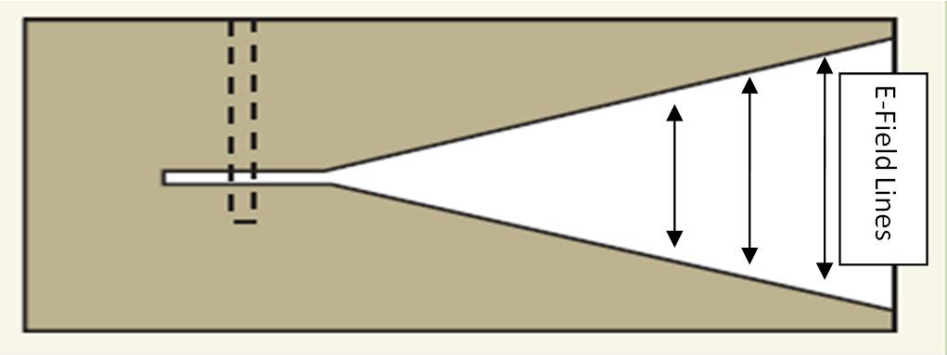

Figure 2.2. Tapered slot antenna electric field lines

2.1.2. Bandwidth Characteristics of Tapered Slot Antennas

Ideally, TSA operates over a large bandwidth. The higher end of the antenna operating frequency range is dictated by matching at feed transition and aperture (slot) termination. A good matching at the input of TSA can easily provide several octaves of operation. Numerous methods and taper profiles were invented to increase the bandwidth of TSA. Changing guided wavelength abruptly by loading antenna aperture with dielectric may result in small bandwidth of operation [41].

2.1.3. Tapered Slot Antenna Taper Profiles

Tapered slot antennas are classified according to their taper profiles as illustrated in Figure 2.3. Exponentially tapered (known as Vivaldi), constant width and linear tapered slot profiles are widely known classical geometries for TSA. While the radiation mechanism is similar, each has specific advantages which are useful for decision making in certain applications. Constant width slot profile possesses the narrowest beamwidth for the same electrical size and substrate material which is followed by linearly tapered slot and Vivaldi respectively [42]. Vivaldi has a

considerably large bandwidth, first design by Gibson [43] had a usable bandwidth of 2-20Ghz. Sidelobe levels are lowest for Vivaldi followed by linear slot and constant width slot respectively [42].

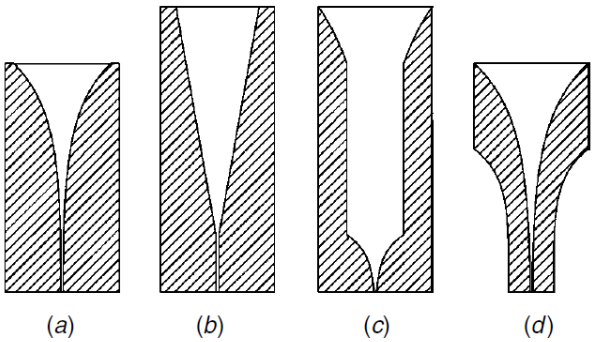

Figure 2.3. Different taper profiles; (a) exponential taper, (b) linear taper, (c) continuous width taper, (d) dual exponential taper

In planar tapered slot antennas, radiation slot act as a ground plane and generally a balanced slotline is used to excite the antenna. Usually, planar tapered slot antennas are etched over low permittivity substrate. Therefore, slotline feed section displays a high input impedance. Microstrip to slot line feed transition can be utilized to achieve impedance matching at 50 ohms.

2.2. Exponentially Tapered Slot Antennas

In 1979, Philips engineer Peter J. Gibson introduced exponentially tapered slot antenna at 9th European Microwave Conference. The original design was capable of providing a stable radiation pattern from 2 to 20 GHz having 10dBi gain and -20dB sidelobe level. It was designed to be used in the 8-40 GHz video receiver module. In his article, Gibson describes the antenna as aperiodic continuously scaled antenna structure theoretically having unlimited instantaneous bandwidth. As a member of traveling wave antenna class, Vivaldi is an ultrawideband antenna capable of operating over several octaves. Exponential taper enables the structure to realize wideband radiation with an aperiodic continuously scale geometry. As separation

distance of slot increases, the electric field between them weakens and leaks away from the antenna at the end of the aperture [43].

Vivaldi antenna is relatively easy to manufacture. It can either be printed (etched) over copper laminated dielectric material or can be made from sheet conductors. Conductor thickness and dielectric constant of the substrate have an impact over antenna properties. Also, array structures can be simply printed over the same material which can expedite the manufacturing process. Due to its simplicity, the Vivaldi antenna is generally low cost. Inherently, this structure has extraordinary radiation characteristics such as low side lobes, high gain and constant beamwidth over a relatively wide bandwidth — increasing length of antenna results in higher directivity which can go up to 17dB [42].

Vivaldi antenna resembles a 2-D exponentially flared horn antenna due to its planar structure with a tapered slot at the end. Similar to other TSAs, it has linear polarization for which the field lines are parallel to the aperture. Another linear polarization can be achieved by using a second Vivaldi perpendicular to the first structure. This type of array arrangement is widely used for microwave imaging applications as shown in Figure. 2.4 [44,45].

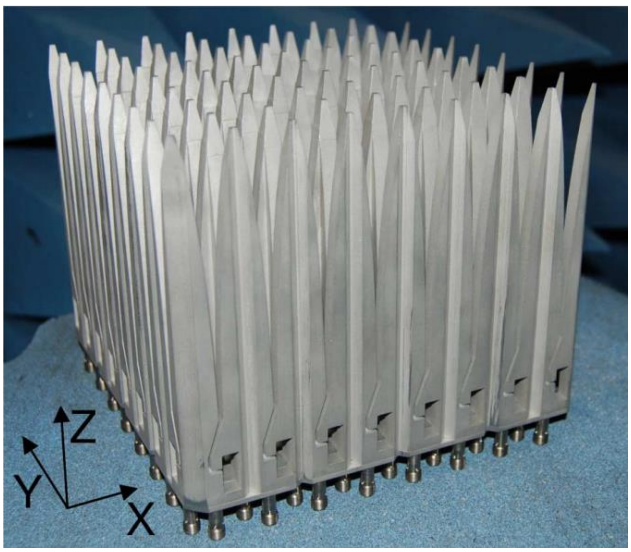

Figure 2.4. Egg crate Vivaldi antenna array

In numerous applications requiring wide bandwidth operation, Vivaldi antenna has been selected for array element including electronic beam scanning structures [46, 47]. Vivaldi antenna is classified as a frequency independent antenna which can effortlessly achieve 10 octaves of bandwidth or even more for return loss lower than -10dB [48]. The lower end of operation bandwidth is limited by the aperture width of the antenna. Although Vivaldi is classified as a frequency independent antenna, the higher end of the operation frequency depends on matching at feed structure.

Most common types of Vivaldi antenna are coplanar, antipodal and balanced antipodal as illustrated in Figure 2.5. Coplanar Vivaldi is the original design of Gibson where both of radiating flares are on the same side of the substrate material. In this type, feeding can be achieved through aperture coupling. A balun structure is required to make a proper transition from the unbalanced transmission line (microstrip, stripline, etc.) to balanced slotline to feed the antenna [43]. Antipodal design circumvents unbalanced to balanced feeding transition problem with an inherently balanced feeding structure. By printing two exponential flares to each side of substrate material in opposite directions, the feeding line becomes a balanced structure [48].

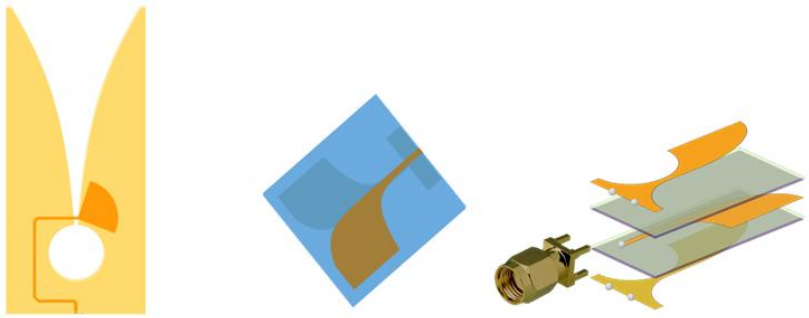

Figure 2.5. Vivaldi antenna types: Coplanar, Antipodal, Balanced Antipodal respectively

Feeding this structure is relatively easy since the whole process only consists of soldering a connector to both flares. Langley et al proposes a three metallic layers Vivaldi having two balanced ground planes, to overcome high cross-polarization of antipodal Vivaldi [49]. This type of Vivaldi balances currents on each radiating

element thereby negates E-field skew. It solves radiation problems in antipodal Vivaldi at the cost of complex production.

2.3. Effects of Physical Parameters over Radiation for Vivaldi Antenna

Each geometrical parameter of the Vivaldi antenna shown in Figure 2.6 affects a different aspect of performance characteristic. When designed correctly, this structure can achieve excellent radiation over large bandwidths. The phase velocity of waves traveling inside a slotline aperture is determined by permittivity and thickness of substrate material. Since Vivaldi antenna is a surface wave structure, it requires waves having phase velocity lower than the light's in vacuum. Therefore, antennas with air as a substrate may not be able to radiate efficiently, since wave traveling inside the antenna might have nearly equal phase velocity of light. This condition necessitates the use of substrate materials with higher dielectric constants compared to air. While antenna with air as substrate has varying impedance over large frequency bands, higher dielectric constant substrates possess relatively constant impedance concerning a wavelength which significantly eases impedance matching.

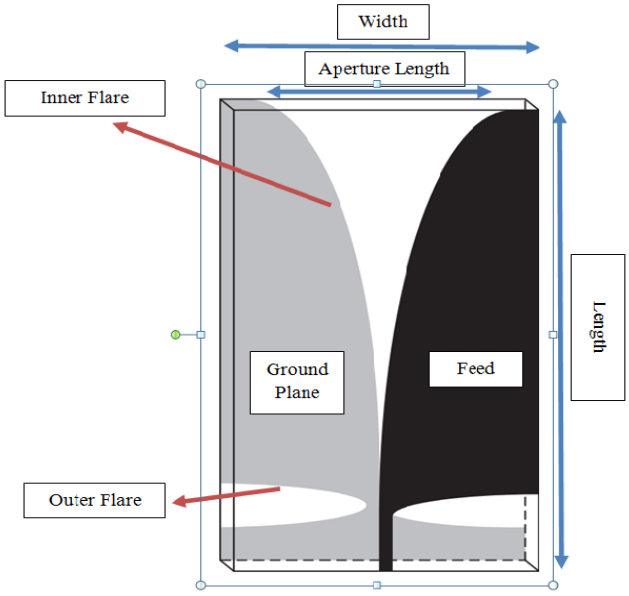

Figure 2.6. Main physical features of antipodal Vivaldi antenna

Radiation characteristics such as directivity and sidelobe levels are severely affected by the substrate. Lower permittivity material results in a wider bandwidth and more efficient operation.

On the other hand, a higher dielectric constant substrate reduces antenna dimensions. Plus, lower dielectric constant material minimizes spurious radiation along the antenna. In the higher frequency band, the dielectric loss becomes the dominant loss mechanism inside a properly designed antenna. Thus, ultra-wide bandwidth antenna design should take account for this effect in the selection of substrate material. Substrate thickness plays an important role in deciding antenna impedance. Thicker substrates increase the total efficiency of the antenna by reducing reactance. The thicker dielectric material can obtain higher directivity at the cost of sidelobes. In the wide bandwidth antennas, thick substrates can be critically detrimental to radiation performance since electrically thicker transmission lines may allow modes different from fundamental one to be excited. In that case, the antenna pattern is the vector sum of all modes radiated from the antenna concerning their energy levels.

Traveling wave antennas radiate energy of surface currents on their metallic parts continuously while surface wave propagates along them. Due to this mechanism, the length of Vivaldi antennas should be at least greater than one wavelength of lowest operation frequency. Thus, antenna length is one of the deciding factors in bandwidth. Designs longer than one wavelength generally produce well radiation characteristics. Directivity can be controlled with antenna length which can go up to 17dB for a single element [42]. Antenna width greater than half-wavelength of operation frequency ensures the standard end-fire radiation from Vivaldi antenna. For narrower structures, surface current can easily couple to the outer flare of the antenna which is naturally radiate in other directions apart from aperture normal. While increasing antenna width does not increase directivity proportionally, it should be higher than the threshold above to attain desired radiation characteristics.

Taper rate of flares affects almost all of radiation characteristics including operation bandwidth, directivity, and sidelobe levels. While increasing the taper rate and creating a larger aperture can lead to a lower operation frequency, it may deteriorate return loss characteristics in the middle to high frequencies. Although a fine tuning should result in VSWR<2 throughout the whole frequency band for Vivaldi antenna, better input matching may be required for specific designs. Aperture size should be greater than half wavelength at the minimum frequency to radiate energy efficiently especially in the lower band. Enlarging aperture width does not guarantee an increase in radiation efficiency necessarily. Electric field traveling along Vivaldi is tightly bound between flares. Larger taper rates result in a weaker electric field with a larger cross-section to be spread out. By this manner, 3dB beamwidth increases in the expense of directivity. In extreme cases, electric filed may break down into several independent phase fronts which may lead secondary beams having nearly equal power to the main beam. Therefore taper rate should be carefully selected to acquire best in the trade off between radiation efficiency and directivity for the structure. Sidelobe levels share a similar behavior where the designer should find an optimum taper rate to minimize unwanted radiation.

2.4. Literature Survey on Vivaldi Antenna Radiation Performance Enhancement

Vivaldi is a suitable antenna for many EM applications due to its planar, simple and compact structure with high-efficiency ultra-wideband operation [51, 52, 53, 54]. In spite of its favorable attributes, it suffers from the skewed beam, low and irregular directivity et cetera [55, 56, 57]. In this section, several techniques to overcome these shortcomings are reported.

Placing dielectric material between flares of Vivaldi was tested to improve its directivity [58, 59]. The idea was to slow waves inside the director so that waves traveling on the edges might have equal optical path length to form a planar wavefront. Inspired by this method, [60] utilized a triangular dielectric material at

the end of the aperture which led up to 4.4dB at a 7.5GHz gain and narrower radiation beamwidth in the 2-15Ghz operation bandwidth. Nassar et al. [61] placed an elliptically shaped metal between the flares to enhance field coupling between the flares to produce more focused radiation as shown in Figure 2.7. The study reports gain enhancement up to 5.5dB at 15Ghz. Front to back ratio was augmented for certain bandwidths. A similar study incorporates a diamond-shaped metallic patch in the aperture resulting 1 dB increase in the gain at 9.5Ghz [62]. Li et al. applied this idea into a balanced antipodal Vivaldi which increased gain up to 4.8 dB in the frequency range of 20 to 30 GHz [63].

Figure 2.7. Parasitic metal patch inside antipodal Vivaldi antenna

Another widely used and researched method is to employ corrugations in the flares of the antenna. Corrugations can be formed by removing small parts of metallic flares. Corrugations along the antenna alter the current distribution inside flares which affects the radiation characteristics. In electrically smaller Vivaldi antennas, surface current may not be able to radiate effectively due to short traveling distance for surface current. Corrugations in the antenna can overcome this problem by forming slot edges around antenna thereby increasing effective length that surface currents travel. Numerous studies investigated this effect and reported good results [64, 65, 66]. De Oliveria et al. reported a 3.3dB gain increase at 6 GHz with better

return loss characteristic [67]. 5 degrees of beam squint in the original design was completely negated with the help of corrugations. Different types of corrugations have been investigated as well. An elliptical slot corrugation was incorporated on the flares of antipodal Vivaldi antenna as shown in Figure 2.8 [68]. The corrugation lowered the minimum operation frequency significantly (570Mhz from 1.69 GHz to 2.26 GHz) thus reducing antenna size.

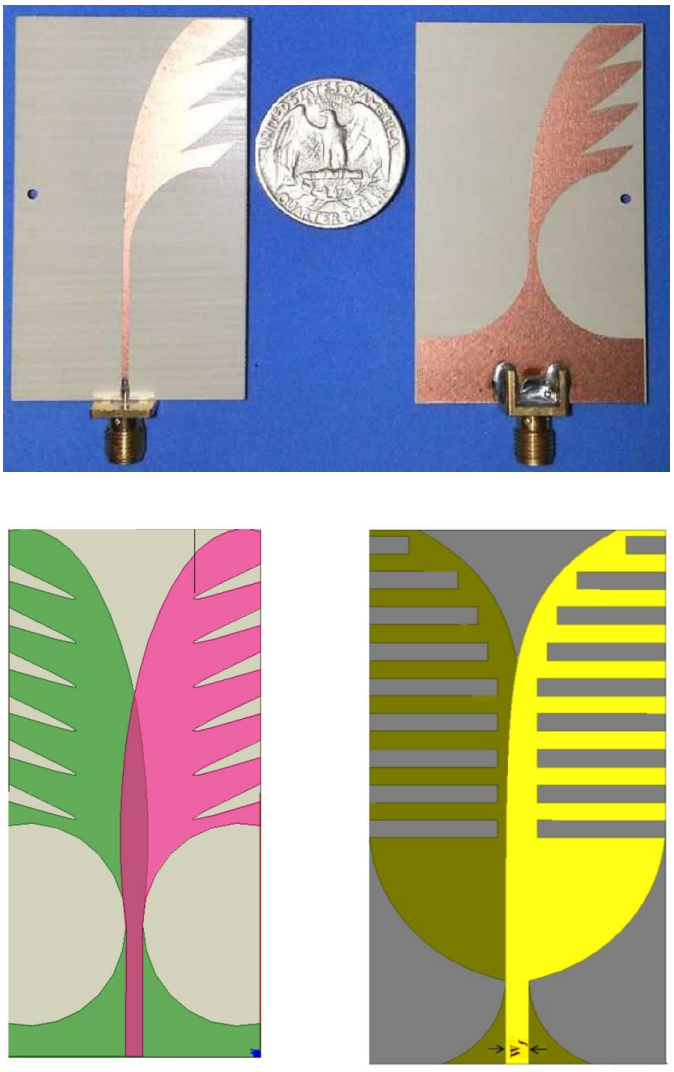

Figure 2.8. Different corrugation types for antipodal Vivaldi antenna

Modifications in outer flare have been reported to boost antenna performance. Antipodal Vivaldi antenna with rounded corners and metallic back plate increased gain 1-2dB in between 6-18 GHz overall [54]. While back plate improved H-plane directivity of the proposed design, round corners facilitated a better current distribution which reduced VSWR below 2 which was 2.2 for the original design. In [70], metallic strips were placed in the aperture of Vivaldi alongside rectangular tapered corrugations in the outer flares which enhanced gain up to 68% at 5.2 GHz. Lower side and back lobes were observed which improved radiation efficiency for 2.9 to 11 GHz operation band.

L.Yao et al. etched trapezoid comb slots over metallic flares of coplanar Vivaldi antenna and included grating elements in the aperture which led to gain increase up to 3dB around 5.25 GHz in the 2-14Ghz operation band. Furthermore, a capacitively loaded loop was added to obtain band notch in the WLAN band to negate interference from commercial systems [71]. Using stepped edge corrugations for dual exponentially tapered Vivaldi antenna, T.J.Huang et al. realized nearly 3dB maximum gain enhancement at 3Ghz for 3-18 GHz operation bandwidth. E-plane and H-plane beamwidth were reduced to lead to more directive pattern in the end-fire direction [72].

2.5. Antipodal Vivaldi Antenna Design

In the scope of this thesis, a novel radiating section of a microwave imaging system shall be developed. As mentioned earlier, the antenna system should be operating over very large bandwidths with directive beam patterns. Radiation efficiency, low profile and compact design are critical for the mission. Therefore, the Vivaldi antenna is selected as a base design for ultra-wide bandwidth metasurface integrated antenna. Apart from the known advantages of Vivaldi for such an application, this structure has a specific predisposition for metasurface applications. Fields radiated from the antenna are tightly bound in the tapered slot aperture and spherically expand as they move outwards from the antenna. By this means, the field has an

excellent avenue to interact with the 2-D metasurface structure since it propagates along substrate material where unit cells are present. Production-wise thinking, it is rather trivial and inexpensive to manufacture such antenna on a single substrate material with a laser cutting machine. Coplanar Vivaldi does not offer the required bandwidth due to the limiting behavior of feeding structure. Although balanced antipodal Vivaldi offers a nearly same bandwidth with more symmetrical patterns for E and H-planes, beamwidth increases with a frequency which can hinder target detection at higher frequencies since shorter wavelengths expand and scatter more compared to longer wavelengths. Thus, antipodal Vivaldi was chosen to facilitate large bandwidth operation with relatively unchanging beamwidth. The only disadvantage this selection introduces is high sidelobe levels. For this particular study, sidelobes are not a crucial factor thereby won't affect the study significantly.

The designed structure consists of two dual exponentially tapered flares where one operates as ground and the other acts as radiating part. In the ground plane flare, there is an exponentially tapered impedance matching section which provides a smooth transition from microstrip to the parallel strip transmission line. The antenna is fed from this structure by a coaxial connector as shown in Figure 2.9.

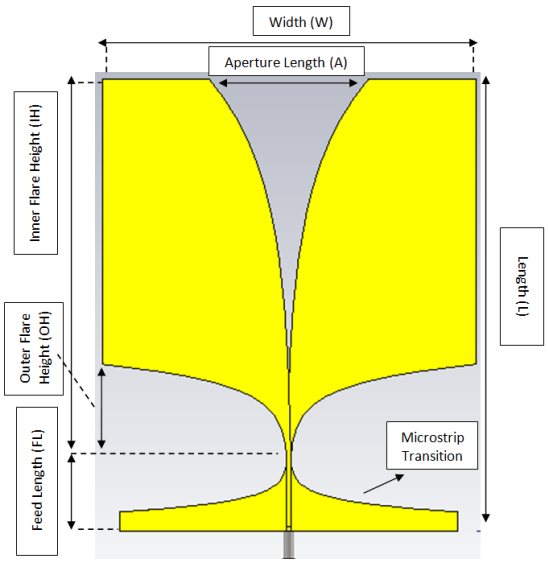

Figure 2.9. Designed antipodal Vivaldi antenna without a dielectric substrate

Main physical features of Vivaldi antennas are exponentially tapered slots. Curvatures of slots are defined by equation [73] below where "R" denotes opening rate of slots. $P_1(x_1, y_1)$ and $P_2(x_2, y_2)$ are first and last points of exponential curves. $c_1\ and\ c_2$ are coefficients determined by length and width of antenna to appropriate a suitable curvature profile for given dimensions.

$$y = c_1 e^{Rx} + c_2 \tag{2}$$

$$c_1 = \frac{y_2 - y_1}{e^{Rx2} - e^{Rx1}} \tag{3}$$

$$c_2 = \frac{y_2 e^{Rx2} - y_1 e^{Rx1}}{e^{Rx2} - e^{Rx1}} \tag{4}$$

In this design, dual elliptically tapered antipodal slot antenna [48] (antipodal Vivaldi) is chosen which has elliptical tapering on the outer edges in addition to inside flare. This dual exponentially tapered structure has advantages over classical design which makes it a favorable choice. An additional tapering in the outer edge can bring multiple benefits to antenna radiation performance and impedance matching. It can offer a degree of freedom to optimize antenna structure by isolating impedance matching in the feeding section.

The radiating flares are excited by a parallel strip line. A coaxial line is soldered on the microstrip transition section. Inherently, parallel strip line combined with slotline radiators constitutes a high input impedance where matching to 50 ohms with good return loss characteristics is fairly hard or even impossible for large bandwidths. A microstrip beginning section which transitions into parallel strip line accommodates matching at lower impedance for very large operation bandwidth [74]. Outer edge and microwave transition parts are both elliptically tapered. Taper exponent rates are optimized to give best input matching between 1-6 GHz for a given length of the curvature.

Antenna length is chosen to accommodate enough distance for feed and inner flare height. Feed length (FL) is optimized to a minimum value which can enable microwave transition to provide a good matching inside the operation bandwidth.

Inner flare height (IH) is selected to facilitate surface currents of the lowest wavelength have minimal distance to travel antenna and be able to radiate, thus provide good radiation efficiency. The trade-off here is between production capabilities and radiation efficiency. Outer flare height (OH) has a sweet-spot where the designer should optimize as reported in [74]. While longer OH brings outer and inner flares too close for a slotline radiator to maintain its slotline characteristics, the shorter length can disrupt exponential taper which allows the wide operation bandwidth.

Antenna width is dictated by half wavelength of the lowest frequency in the operating frequency. Although it is beneficial for radiation efficiency to enlarge the width of the antenna yet, it may conflict with production capabilities. Width is chosen by maximum production capability at hand. Aperture length (AL) is adjusted by antenna width and inner flare exponent rate (R). Since antenna width is fixed in this design, the exponent rate plays an important role in radiation characteristics [75]. Proportional to exponent rate, longer AL leads to weaker field coupled between flares which may even divide into several phase fronts concerning AL and the wavelength. Minimal values of the inner exponent rate may preclude radiation since discontinuities that launch the wave from the antenna may become rather small and cannot be able to radiate energy. Also, too narrow aperture length can spoil S11 characteristics in the lower frequency band.

Table 2.1. *Designed antipodal Vivaldi antenna geometrical parameters*

Parameters	*Distance(mm)*	*Parameters*	*Distance(mm)*
Width	199.07	Outer Flare Exponent	0.095
Length	240	Inner flare exponent	0.019
Aperture Length	85.11	Inner Flare Height	200
Feed Length	40	Ground Base Width	180.33
Feed Line Width	2.3	Ground Base Height	10

Arlon Iso 917 (Epsilon=2.2, El.tand= 0.0013) is used as substrate material for the designed structure. As mentioned earlier in the design considerations section, materials with dielectric constant close to air can be detrimental to radiation performance whereas higher dielectric constant can lead to severe dielectric losses for high operating frequencies. This material was found to be an optimum solution for such an application having a convenient permittivity and very low loss characteristics. Substrate thickness is 0.762mm (30mil), and copper thickness over dielectric is nearly 0.018mm. Substrate thickness plays a significant role for such large bandwidth devices since thicker substrates can enable excitation of modes other than the fundamental one which can disrupt radiation pattern dramatically.

Simulation results for the design show exceedingly well return loss characteristic as depicted in Figure 2.10 and Figure 2.11 in terms of S11 and VSWR respectively. S11 is below -10dB (VSWR<2) between 1-10 GHz having a margin in the lower end of the band that stretches up to 900 MHz approximately. The higher limit of the band for input matching has not been reached in this frequency band.

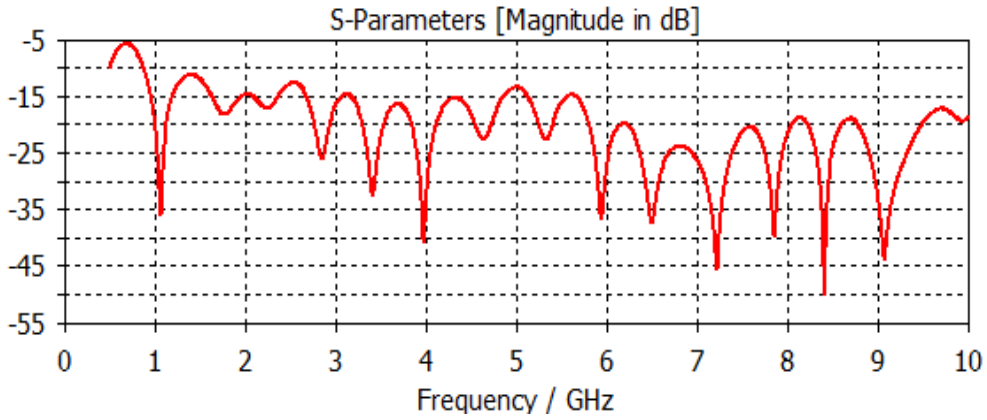

Figure 2.10. Return loss for designed antipodal Vivaldi antenna

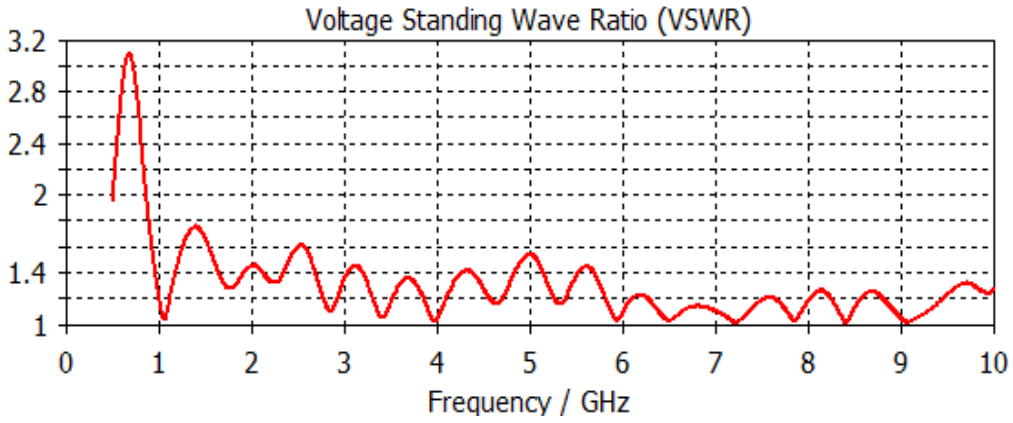

Figure 2.11. VSWR for designed antipodal Vivaldi antenna

Both radiation and total efficiencies are remarkably high over entire operation bandwidth (1-6GHz) and even extending to 10 GHz. It can be seen that efficiency is over 90% for the designed structure. Also, nearly planar efficiency behavior as illustrated in Figure 2.14 over a very large bandwidth ensures stable operation in the whole bandwidth.

Figure 2.13 shows the maximum gain over the selected frequencies. There is a steady increase between 4 and 10 GHz. The flat gain characteristic can be observed between 2 and 4 GHz. A steep increase is observed in 1-2 GHz bandwidth. This dramatic increase is strongly related to the electrical size of the antenna. The wavelength at 1 GHz is longer than the antenna which does not allow the surface current to travel and radiate alongside antenna efficiently.

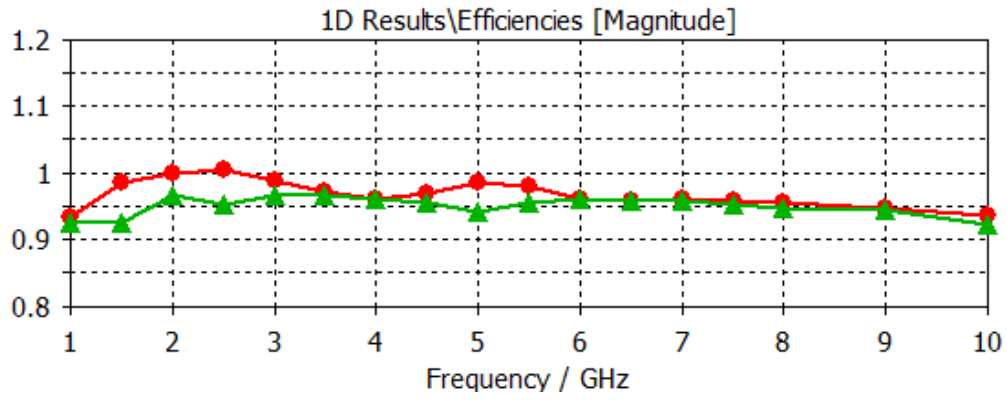

Figure 2.12. Radiation (red line) and total (green line) efficiencies of antipodal Vivaldi antenna

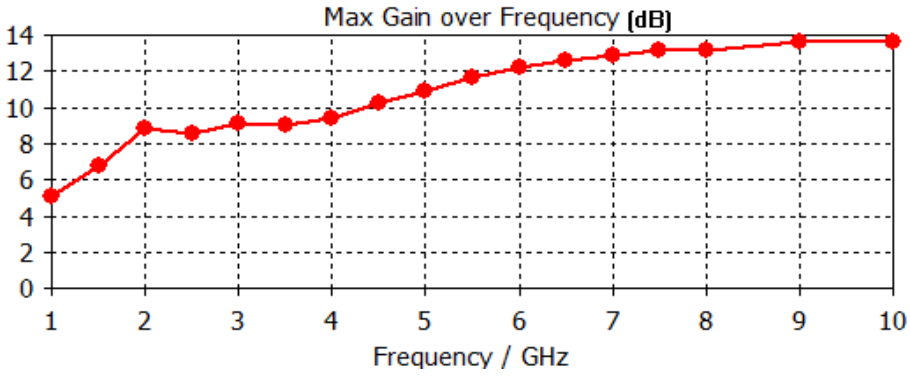

Figure 2.13. Maximum gain over the frequency of antipodal Vivaldi antenna

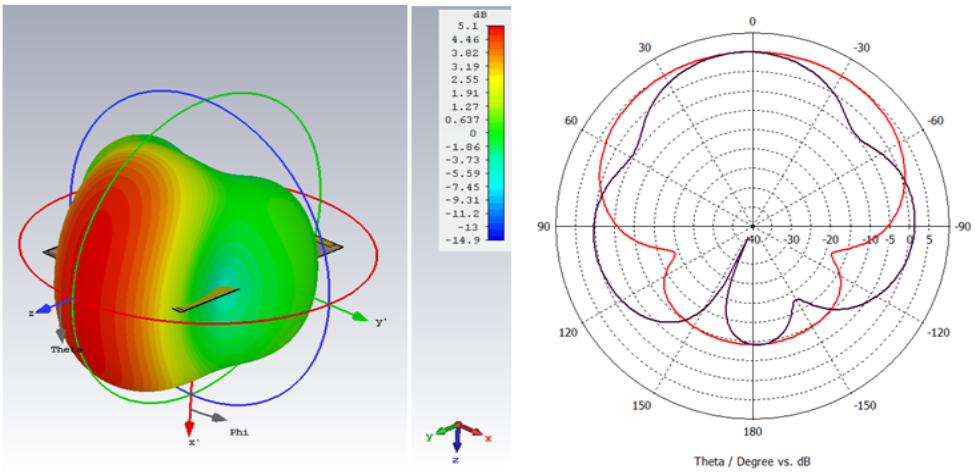

Figure 2.14. 3-D and polar far-field pattern of the designed antipodal antenna at 1 GHz (red line elevation and black line azimuth cut)

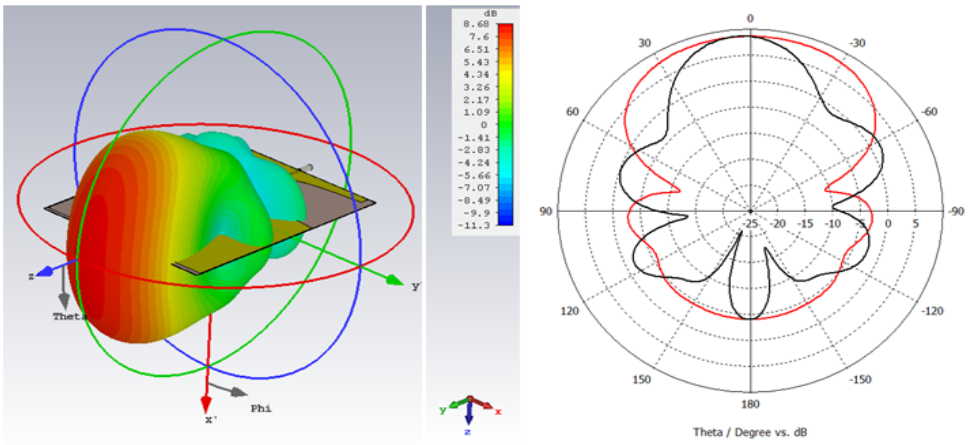

Figure 2.15. 3-D and polar far-field pattern of the designed antipodal antenna at 2 GHz (red line elevation and black line azimuth cut)

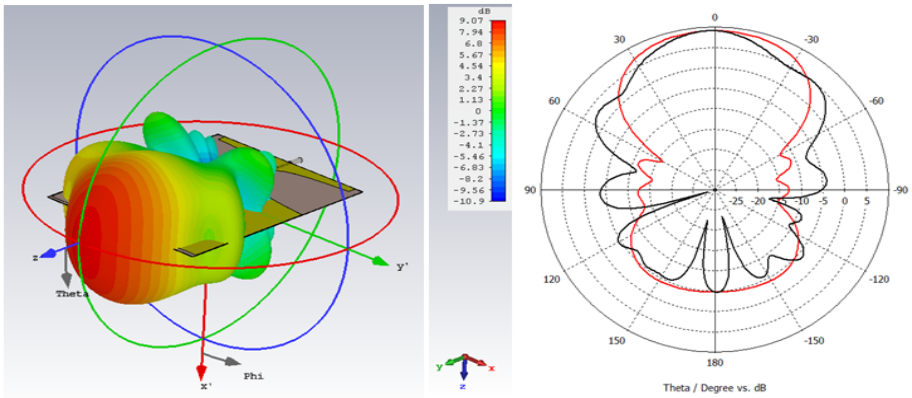

Figure 2.16. 3-D and polar far-field pattern of the designed antipodal antenna at 3 GHz (red line elevation and black line azimuth cut)

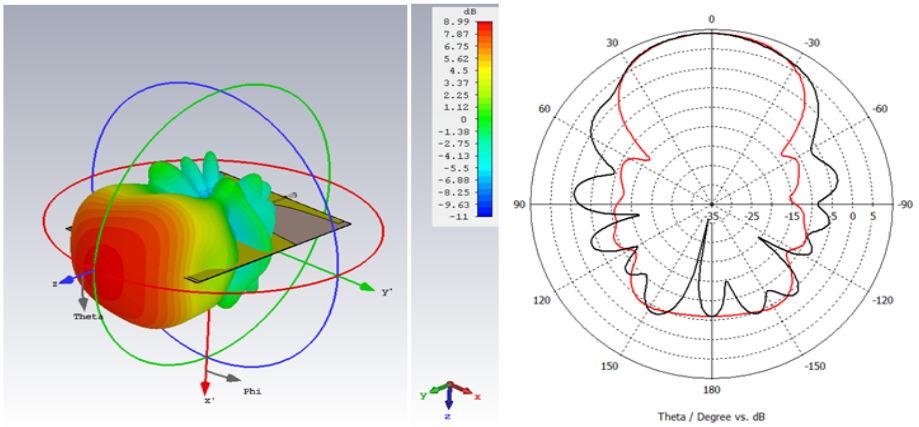

Figure 2.17. 3-D and polar far-field pattern of the designed antipodal antenna at 3.5 GHz (red line elevation and black line azimuth cut)

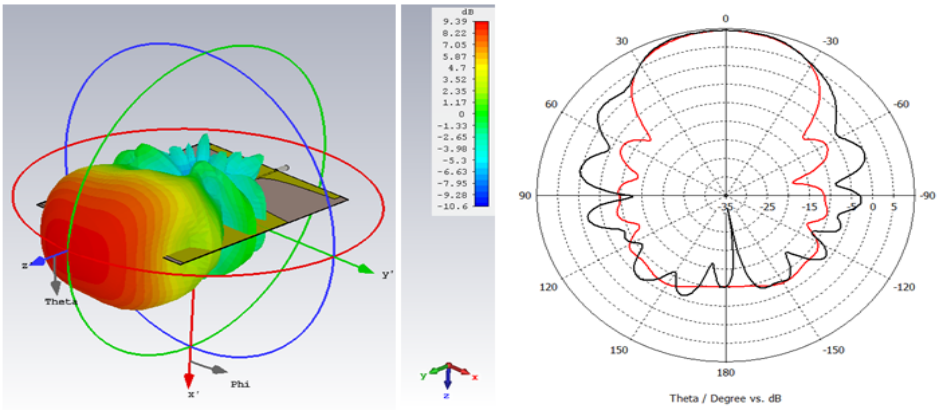

Figure 2.18. 3-D and polar far-field pattern of the designed antipodal antenna at 4 GHz (red line elevation and black line azimuth cut)

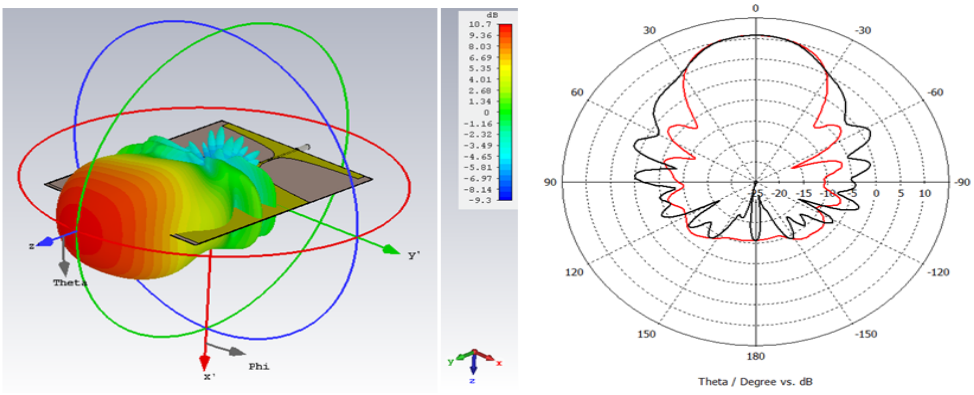

Figure 2.19. 3-D and 2-D far-field pattern of the designed antipodal antenna at 5 GHz (red line elevation and black line azimuth cut)

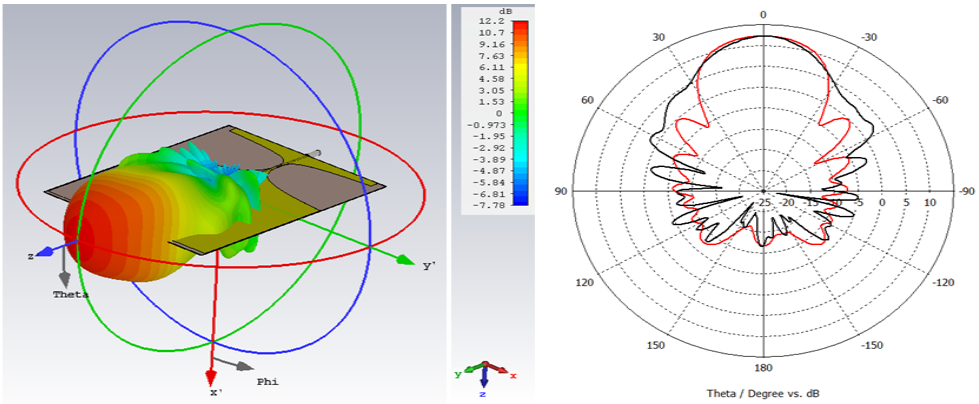

Figure 2.20. 3-D and polar far-field pattern of the designed antipodal antenna at 6 GHz (red line elevation and black line azimuth cut)

Table 2.2. *3dB beamwidth of antipodal Vivaldi antenna versus frequency for azimuth and elevation cuts*

Frequency (GHz)	Azimuth 3dB BW (degree)	Elevation 3dB BW (degree)
1	**56.4**	**131.6**
2	**38.9**	**92.5**
3	**45**	**67.3**
3.5	**62.8**	**58.7**
4	**55.9**	**55.2**
5	**44.3**	**47**
6	**35.9**	**40.3**

While operating over large bandwidths and relatively directive radiation pattern with acceptable sidelobe levels, the antenna performance meets the expectations. 3-D and polar radiation patterns do not indicate anomalies or problematic beam behavior such as split or erratic beam shape. 3-D far-field pattern illustrates that beam shape converges into a pencil beam as the frequency progresses. E and H-plane patterns are more similar after 3GHz compared to 1-3GHz bandwidth which is quite the expected result since electrical size over 3GHz is sufficient for the antenna to possess traveling wave structure properties fully. Few modifications to improve radiation characteristics were undertaken in the scope of this work. Initially, corrugation was incorporated in flares of the antenna. As suggested in the literature [26,27,28], corrugations on the flares extend effective path length of the surface currents which can increase radiation efficiency in the lower frequency band. Rectangular slit type slots were etched over antenna flares as shown in Figure 2.21.

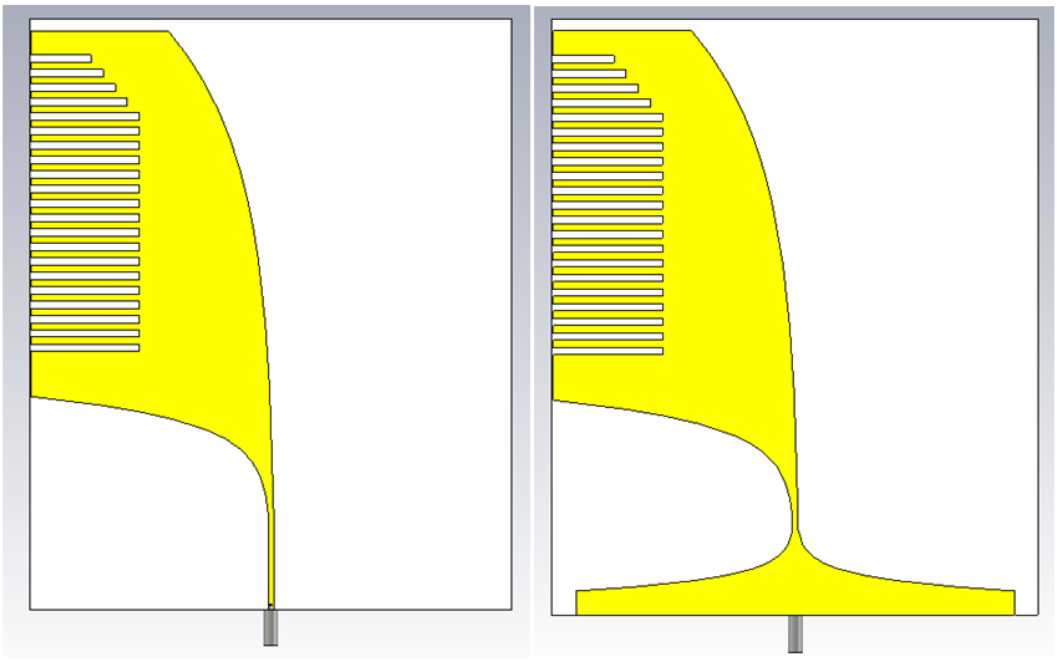

Figure 2.21. Top and bottom view of corrugated Vivaldi antenna

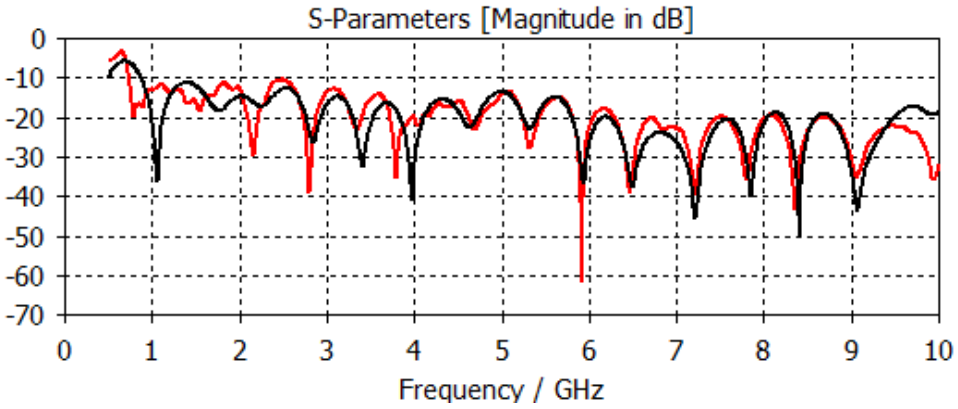

Figure 2.22. Return loss for original and corrugated antipodal Vivaldi antenna (red line corrugated and black line original respectively)

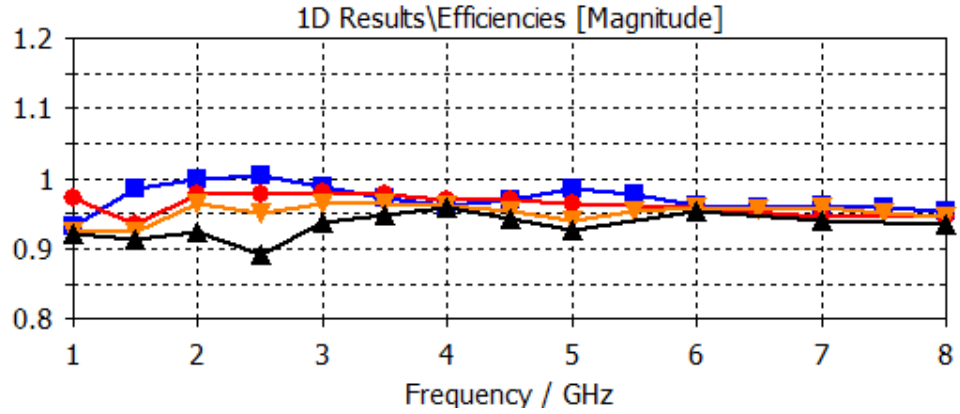

Figure 2.23. Return loss for original and corrugated antipodal Vivaldi antenna (yellow and blue line total and radiation efficiencies of original design respectively, black and redline total and radiation efficiencies of corrugated design respectively)

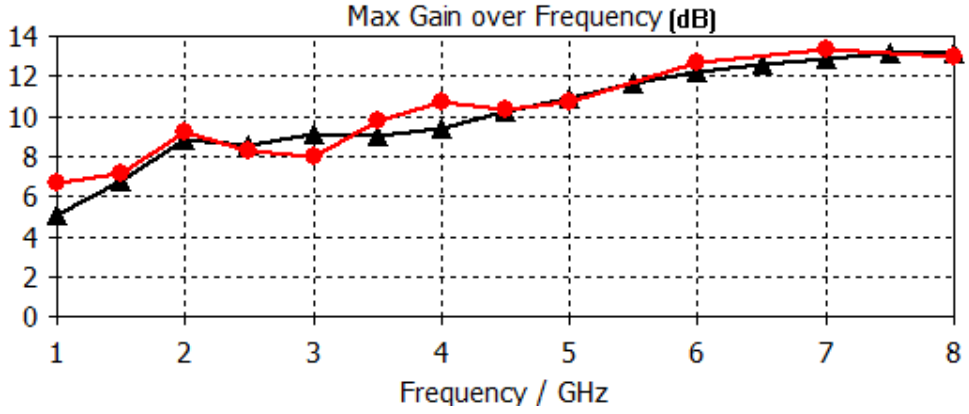

Figure 2.24. Maximum gain over frequency for original and corrugated antipodal Vivaldi antenna (red line corrugated and black line original respectively)

Corrugations improved lower side of operation bandwidth and extended S11<-10dB range to 750MHz which nearly translates into 150MHz bandwidth extension which is a quite meaningful result at these frequencies. There is no considerable change in efficiency which reaches 95% at most in a relatively small bandwidth. Radiation patterns clarify the degradation in radiation efficiency at those frequencies.

Radiation patterns at 3.5 and 4GHz show a beam split in the azimuth direction. Although in the literature lucrative sides of corrugation on Vivaldi antenna have been published, the modification comes at the cost of beam split no matter the configuration and sizes are. This behavior explains fluctuations in maximum gain over frequency graph as opposed to an expected steady gain increase trend. Despite performance enhancement it provides, corrugation in this particular design is not utilized for the sake of beam integrity. A split beam can cause multiple problems in microwave imaging which can preclude detection and imaging.

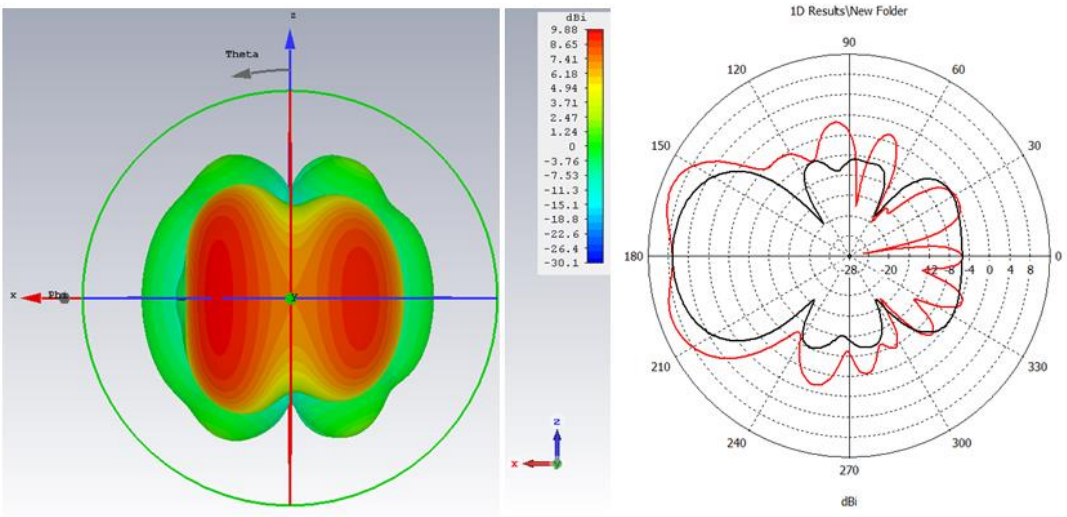

Figure 2.25. 3-D and polar far-field pattern of corrugated antipodal Vivaldi antenna at 3.5 GHz (red line azimuth and black line elevation cut)

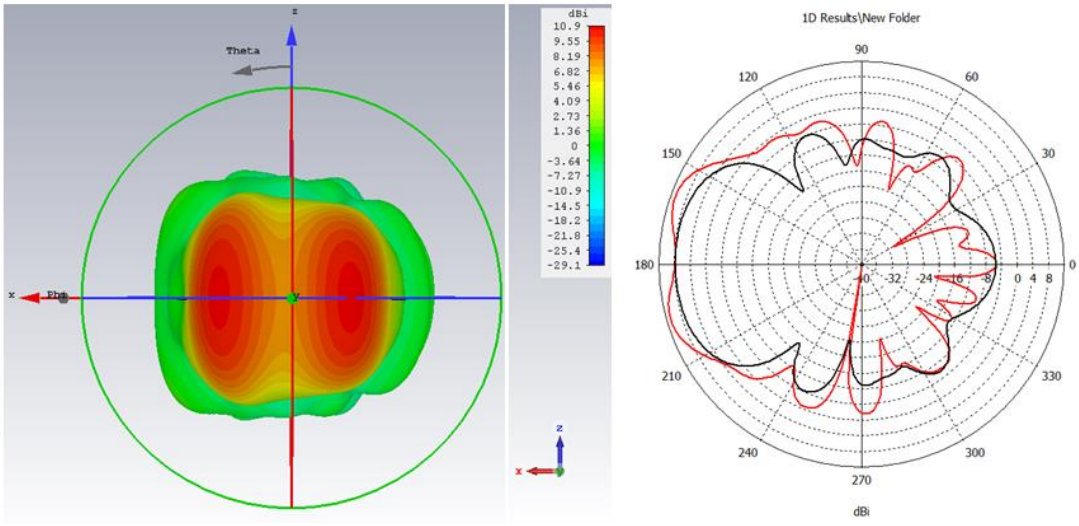

Figure 2.26. 3-D and polar far-field pattern of corrugated antipodal Vivaldi antenna at 4 GHz (red line azimuth and black line elevation cut)

CHAPTER 3

METASURFACE LENS DESIGN AND INTEGRATION FOR ANTIPODAL VIVALDI ANTENNA

3.1. Metamaterials and Metasurfaces at Microwave Frequency

Metamaterials (MM) are artificially engineered materials possessing extraordinary properties which are not available in their natural counterparts. Their periodically arranged unit cells resemble the molecular structure of natural crystals. Unlike the natural materials, building blocks of metamaterials are unit cells, which are macroscopic structures compared to atoms or molecules. They are small metallic inclusions in the dielectric which can intensively interact with electromagnetic waves. Interaction style between unit cells and the incident EM wave determines the EM characteristics of the engineered material [76]. In this manner, extreme EM properties that are not found in nature such as negative or zero permittivity/permeability can be realized with the correct use of natural materials [2, 3,4]. In the literature, metamaterials are classified mainly by their effective EM properties inside a unit cell $\varepsilon_{eff} = \varepsilon_0\varepsilon_r$ and $\mu_{eff} = \mu_0\mu_r$. To allow such notation, unit cells should be much smaller than incident wavelength. This condition ensures homogeneity of the EM response of the material. Thus, ε_{eff} and μ_{eff} do not vary with the wavevector nor on the response of neighboring unit cells. In this case, spatial dispersion can rightfully be overlooked [77].

Light-matter interaction must be clarified on a fundamental level to develop a physical understanding of artificial materials with controllable properties. A monochromatic plane wave incident on a surface is considered.

$$\vec{E}(\omega, k) = \overrightarrow{E_0}\exp(-j\vec{k}.\vec{r} + j\omega t) \quad (5)$$

$$\vec{H}(\omega, k) = \overrightarrow{H_0}\exp(-j\vec{k}.\vec{r} + j\omega t) \quad (6)$$

$\vec{E}$ and $\vec{H}$ are the electric and magnetic fields of the plane wave respectively where $\vec{k}$ is the wavevector and ω is the angular frequency. Maxwell's equations in differential form can be written as;

$$\nabla \times \vec{E} = -\frac{\partial \vec{B}}{\partial t} \quad (7)$$

$$\nabla \times \vec{H} = \vec{J} + \frac{\partial \vec{D}}{\partial t} \quad (8)$$

$$\nabla.\vec{D} = \rho \quad (9)$$

$$\nabla.\vec{B} = 0 \quad (10)$$

Where $\vec{B}$ and $\vec{D}$ are flux densities of magnetic and electric fields respectively. Charge and current densities are denoted as ρ and $\vec{J}$. Fields and flux densities are interlinked via constitutive equations in an isotropic linear medium.

$$\vec{D} = \varepsilon\vec{E} = \varepsilon_0\varepsilon_r\vec{E} \quad (11)$$

$$\vec{B} = \mu\vec{H} = \mu_0\mu_r\vec{E} \quad (12)$$

where ε_0 and μ_0 are permittivity and permeability in free space whereas ε_r and μ_r are relative permitivity and permeability of the medium in comparison with vacuum. In the absence of sources (free charges (ρ) and currents $(\vec{J})$), phasor form of Maxwell's equations for a monochromatic wave can be reduced to,

$$\vec{k} \times \vec{E} = \mu\omega\vec{H} \quad (13)$$

$$\vec{k} \times \vec{H} = -\varepsilon\omega\vec{E} \quad (14)$$

In this context, permittivity is expressed as complex dielectric function of the material where $\varepsilon = \varepsilon_{real} - j\varepsilon_{imag}$. This is the most common form associated with Maxwell's equations. However, a more useful and physical representation for material property is complex refractive index where $n = n_{real} - j\kappa$. Here, index of

recfraction n is the ration of speed of light in vacuum to material and κ denotes the extinction coefficient of light inside medium.

$$\varepsilon_{real} = n_{real}^2 - \kappa^2 \tag{15}$$

$$\varepsilon_{imag} = 2n_{real}\kappa \tag{16}$$

$$n = \sqrt{\varepsilon_{real}},\ for\ \mu_{real} = 1 \tag{17}$$

$$\kappa = \frac{\varepsilon_{imag}}{2n} \tag{18}$$

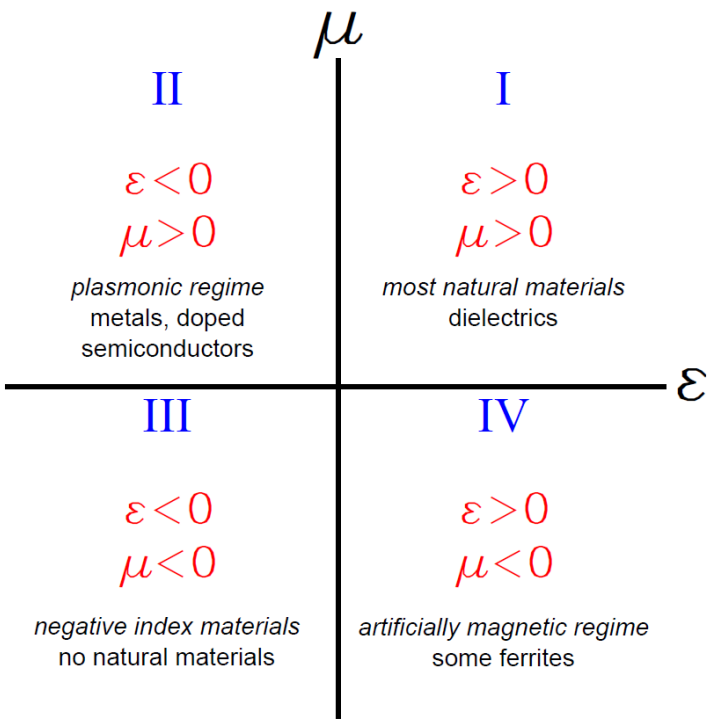

Figure 3.1. EM properties of materials

Materials can be classified in terms of their EM properties. In Figure 3.1, first quadrant contains most of the natural material where ε and μ are positive. Second quadrant is the plasmonic regime where ε is negative and μ is positive. In the third quadrant, negative refractive index materials are present for which both constitutive parameters are negative. Lastly, fourth quadrant encapsulates artificial magnetism

materials where ε is positive and μ is negative. Materials in second and fourth quadrant yield an imaginary wavenumber for the EM waves which means propagation of EM wave inside this medium is not possible. On the other hand, first and third quadrant constitutive parameters yield a real wavenumber where propagation is possible. Of course, there is a fundamental difference in terms of propagation of EM wave in these mediums which shall be explained later in this text.

3.2. Design Procedure form Metamaterial with Artificial EM Characteristics

Veselago's extraordinary work on metamaterial foundations [1] had remained unexplored for nearly three decades. Pendry et al. realized the theoretical premise of Vesalago by incorporating metallic resonators inside the dielectric medium [2,3]. In this section, the design of structures with selected permittivity and permeability values is discussed. Using standard EM models, constitutive parameters of microscopic structures can be determined. Drude-Lorentz model is commonly used in both metamaterials and plasmonics research due to its relevance to the structures. In this model, carriers are considered as damped harmonic oscillators which are driven by incident EM waves [78].

$$\varepsilon_r(\omega) = 1 - \frac{\omega_{p,e}^2}{\omega^2 - \omega_{0,e}^2 + j\gamma_e\omega} \tag{19}$$

$$\mu_r(\omega) = 1 - \frac{\omega_{p,m}^2}{\omega^2 - \omega_{0,m}^2 + j\gamma_m\omega} \tag{20}$$

Losses of materials are denoted with damping coefficient γ while ω_p and ω_0 are the plasma frequency and resonance frequency, respectively. In equations (19) and (20), e and m denotes the electric and magnetic responses of the medium. For most materials available in nature, there are certain limits in terms of EM properties. As mentioned earlier, provided that subwavelength unit cells are much smaller than incident wavelength, EM characteristics of material can be described as $\varepsilon_{r,eff}$ and $\mu_{r,eff}$. By employing intelligent design, these properties can be determined at a

macroscopic level. As a preliminary instruction on design procedure, one of the earliest metamaterial architecture called split-ring resonator (SRR) is analyzed here. This type of structure can enable control over both electrical and magnetic responses of the medium depending upon the type of EM excitation. Using engineering approach, resonators are modeled with equivalent circuit theory in this analysis. SRR is modeled by an LC circuit with a resonance frequency of $\omega_0 = \sqrt{\frac{1}{LC}}$. Here, L and C are effective inductance and effective capacitance of the SRR array, respectively. For $\gamma = 0$ i.e lossless materials, when the incident wave frequency is equal to the natural resonance frequency, effective magnetic response of the structure changes drastically according to Drude-Lorentz model in equation (20). When incident upon the resonator, EM wave with a magnetic field component that is perpendicular to SRR surface can excite a circulating current at frequency of ω_0 inside resonator which induces a strong magnetic moment. In the rest of this section, derivation of effective permeability outlined in Pendry et al.[3] is followed. Related physical dimensions are shown in Figure 3.2, where C denotes capacitance for unit area.

$$C = \frac{\varepsilon_0}{d} = \frac{1}{dc^2\mu_0} \tag{21}$$

Thus, $\mu_{r,eff}$ can be written as;

$$\mu_{r,eff}(\omega) = 1 - \frac{F\omega^2}{\omega^2 - \omega_0^2 + j\Gamma\omega} \tag{22}$$

Here, F represents the ratio of the resonator volume to the unit cell volume.

$$F = \frac{\pi r^2}{a^2} \tag{23}$$

$$\omega_0 = \sqrt{\frac{3dc^2}{\pi^2 r^3}} \tag{24}$$

$$\Gamma = \frac{2}{r\sigma\mu_0} \tag{25}$$

In the expressions above, Γ denotes damping term and σ represents conductivity of the metal. In the microwave frequencies, dimensions of resonator are in the order millimeters. Such SRR example with physical dimensions suited to microwave frequency is shown in Figure 3.2. In the figure, a=3.5mm, d=0.25mm, r=1.5mm. These dimensions yield a resonant frequency of 7.165 GHz. One can observe wavelength at this frequency (41.87mm) is nearly 12 times larger than unit cell size which is a good ratio to approximate this artificial medium as homogenous in terms of EM properties.

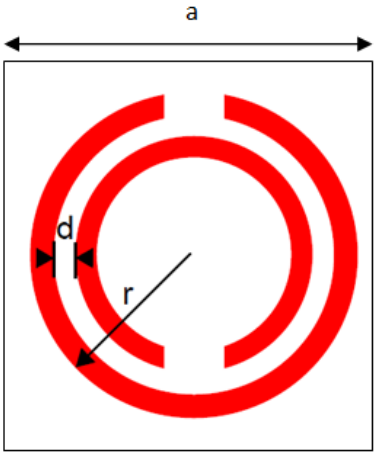

Figure 3.2. SRR design as originally introduced by Pendry et al. Black line indicates borders of unit cell and red lines represent split ring resonators

3.3. Effective Medium Theory and Homogenization Methods

It is desired to model a medium with scattering inclusions as a homogenous medium in terms of EM properties, if possible, because the complexity of the analysis would be drastically reduced due to the homogenous model of the medium. This equivalence is assumed to be valid when the wavelength of the incident field is much larger than the size of local inclusions. Composite materials can be characterized in terms of effective parameters in the same manner done for homogenous materials by solving the Maxwell's equations relating local sources (charge and current) to fields (electric and magnetic). In most cases, complexities of composite materials preclude determination of EM response of the material by analytical methods. Various

numerical techniques are proposed to obtain critical information about the material to solve this problem. Apart from their qualitative merits, they do not provide experimental characterization. There are several different homogenization methods proposed in the literature [79, 80] which aims to model composite structures with resonant inclusions as bulk materials.

Nichols-Ross-Weir (one of the earliest and simplest technique in the literature) is a retrieval method which extracts effective constitutive parameters from scattering matrices of the material. Although it was not originally proposed for metamaterials, modified versions quickly became the dominant retrieval methods for engineered materials. In essence, these methods assume that material with a complex structure such as metallic resonator inclusions inside dielectric can be treated as a homogenous material with effective parameters [81, 82]. Often appealing for its simplicity, this method yields unphysical constitutive parameters especially when the homogeneity condition is violated. Complex permittivity and permeability values with unrealistic values and unphysical frequency dispersion around the resonance frequencies often plague results retrieved with this method. Experiments utilizing such schemes [82, 83, 84] violate causality and passivity conditions dictated by fundamental laws such as Kramers-Kronig [85] relations and the second law of thermodynamics, respectively, that requires

$$\varepsilon_{imag} > 0 \ , \frac{\partial \varepsilon_{eff}}{\partial \omega} \geq 0 \tag{26}$$

$$\mu_{imag} > 0 \ , \frac{\partial \mu_{eff}}{\partial \omega} \geq 0 \tag{27}$$

for $e^{j\omega t}$ time convention. Even though this method can provide useful insight to EM response of metamaterials and resonance frequency of the unit cells, sign problems in the non-physical imaginary parts of retrieved parameters and anti-resonant artifacts indicate the inadequacy of this method. Also, effective parameters change with excitation and boundaries which makes it quite hard to determine to select a correct solution [86, 87]. The anomalies in the retrieved parameters are closely

related to strong spatial dispersion. This effect must be taken into account with improved homogenization models.

Analytical/semi-analytical methods have been devised to solve homogenization rigorously. A generalized Clausius-Mossotti model has been extended to complex inclusions to model inclusion interaction accurately [88, 89]. This method can take bianisotropic effects and a possible presence of spatial dispersion. Another successful method proposed in literature averages the planar sheet of composite medium considering the interaction among layers of inclusion as Bloch lattice [90, 91]. Despite their rigorous approach, strong spatial dispersion induced unphysical artifacts in the effective parameters.

Additionally, results of both methods depend on excitation and boundary conditions same as NRW based methods. Another successful approach to the homogenization of composite structures based on the Floquet representation used in crystal structures [92, 93] to circumvent these problems. Handling bianisotropy, higher-order spatial dispersion and polarization effects intelligently, this method introduces a single generalized effective permittivity tensor. Unfortunately, this method is only valid for dielectric metamaterials and relating bianisotropic effects to weak spatial dispersion proves a challenging task.

Provided that wavelength is too large compared to inclusion size, i.e. the operation frequency is well below the unit cell resonance frequency, methods discussed above can be utilized to characterize a subset of engineered materials if not all of them. This assumption is only valid when spatial dispersion is negligible which is the situation in the long wavelength limit. In this work, metamaterial characterization is handled by two separate methods and results were cross-checked for accuracy. First method is a modified version of NRW for composite structures. In this technique, imaginary parts of effective parameters are obtained from scattering parameters. Then, the real part is calculated by using the Kramers-Kronig relationship [94]. Therefore, the causality problem mentioned earlier is circumvented

by the smart use of a fundamental relationship. As long as the guided wavelength inside the material is too large compared to average array granularity, we can expect physically valid results out of this method. The second method does not calculate ε_{eff} and μ_{eff} directly, yet it does provide n_{eff} which provides a degree of accuracy for comparison purposes. In this method, the eigenmode analysis of the single cell structure is utilized to obtain the dispersion diagram of the material. Afterwards, it is a trivial task to determine the refractive index of the material.

3.4. Unit Cell Design

As mentioned earlier, the GPR system requires a microwave sensor with large operation bandwidth and a directive antenna beam. Although the candidate antenna shown in the second chapter has a quite wide bandwidth, 3dB beamwidth, i.e. half power beamwidth (HPBW) needs to be reduced for better resolution. Also, the detection of objects buried in soil with a high loss coefficient is much harder due to the low power of the received signal. In this case, an antenna with a higher gain can be helpful for better detection. Therefore, a metasurface structure to be integrated with the antenna should be operating in the entire operation bandwidth of the antenna and enhance its radiation characteristics. In this section, several metamaterial cell topologies are designed and tested. The results of both material characterization to be used in the design process for the antenna system.

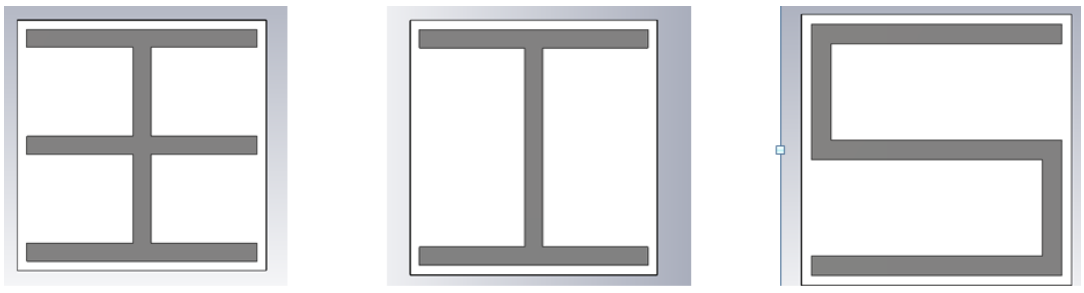

(a) (b) (c)

Figure 3.3. Candidate unit tell topologies for metasurface antenna, (a) capital I with stroke (CIWS), (b) capital I (CI), (c) meanderline (ML)

There are numerous topologies for the unit cell structure in the literature. Each one possesses either electric or magnetic response (or both in some cases) which is determined by their geometry and by the characteristics of the incident wave. The operation range of their response is closely related to dimensions of metallic inclusion and dielectric host medium. Three candidate unit cell topologies are illustrated in Figure 3.3. To the best knowledge of the author, "capital I-shape with stroke (CIWS)" topology has never been reported so far in the literature. The CST [106] simulation scheme used in this study is displayed in Figure 3.4. In this setup, the unit cell has a long conducting strip parallel to the computational medium. We call this configuration as resonator setup for the reasons which will be clear later in this section. In the figure, the red rectangular cross-sections of the computation medium represent input and output ports and computational medium is shown by the black rectangular prism.

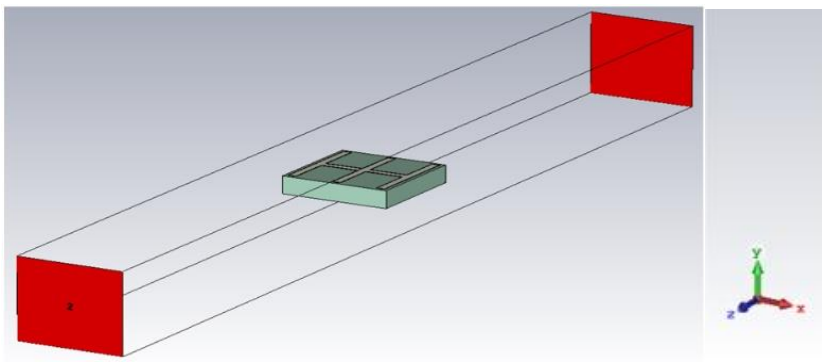

Figure 3.4. Resonator excitation configuration

The walls of the computational medium control the polarization of the incident wave. Walls in the –x-direction are PEC and in the –y-direction are PMC in Figure 3.5. Naturally, excitation polarization is perpendicular to PEC walls. The bounding box is filled with vacuum which will ensure the correct characterization device under test. However, the incident wave travels along the entire waveguide which will provide erroneous information about the phase of the wave. Therefore, a deembeding procedure is applied to the scheme to retrieve the phase only over the unit cell.

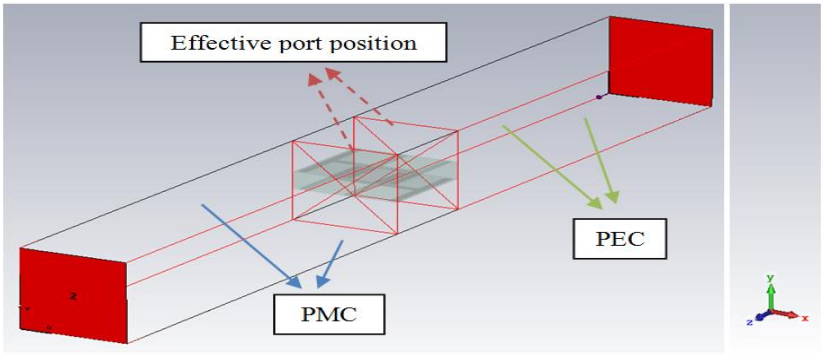

Figure 3.5. Waveguide walls and phase deembedding

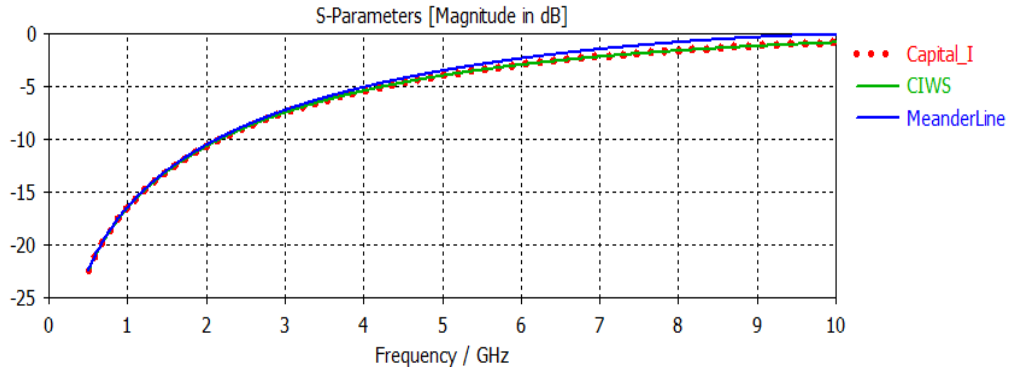

Figure 3.6. Return loss (S11) for unit tell topologies

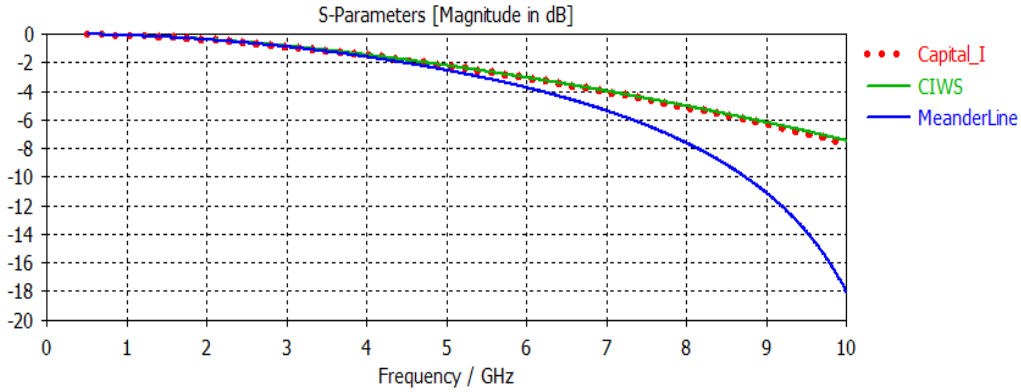

Figure 3.7. Transmission loss (S21) for unit tell topologies

The scattering parameters (S11 and S21) of simulated array of unit cells are shown in Figures 3.6 and 3.7 for different unit cell structures. Capital I (CI) and CIWS topologies have similar transmission characteristics whereas the meander line (ML) displays a steep decline in S21 curve after 8 GHz. Therefore, it is expected to see

similar frequency dispersion effects in the effective parameter curves to be obtained for CI and CIWS topologies as demonstrated in Figure 3.8 through Figure 3.13.

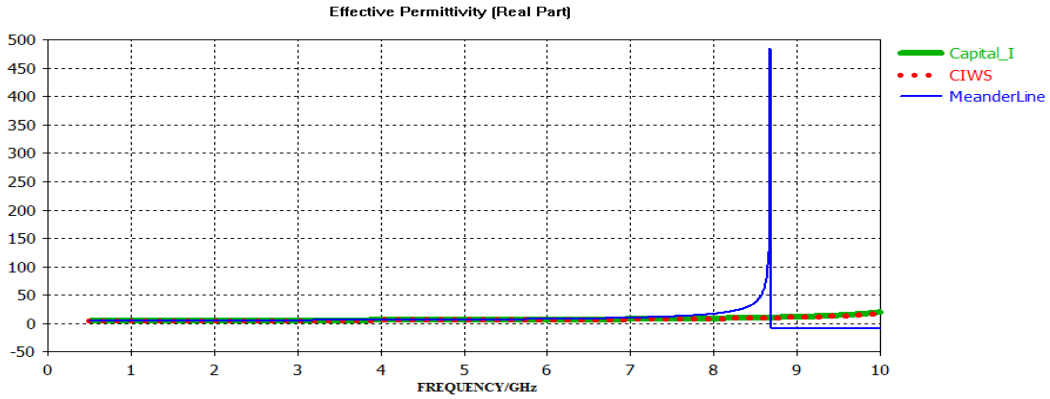

Figure 3.8. Real part of effective permittivity for unit tell topologies

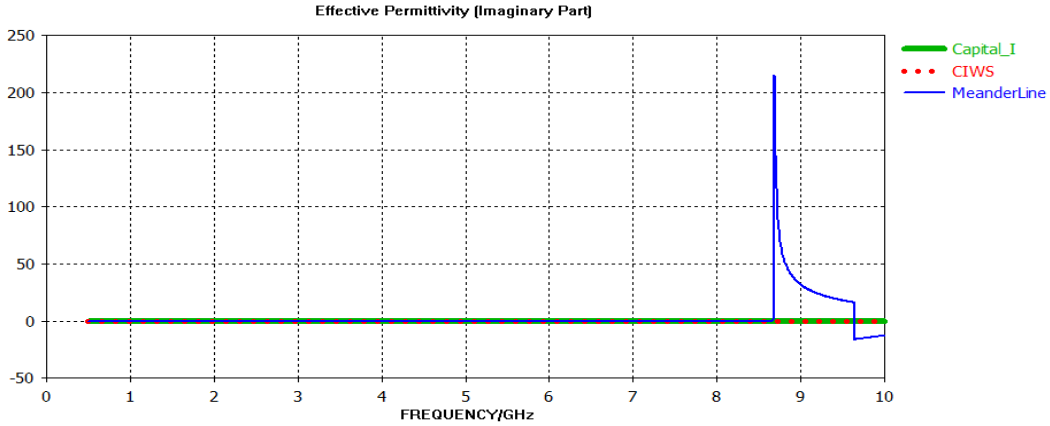

Figure 3.9. The imaginary part of effective permittivity for unit tell topologies

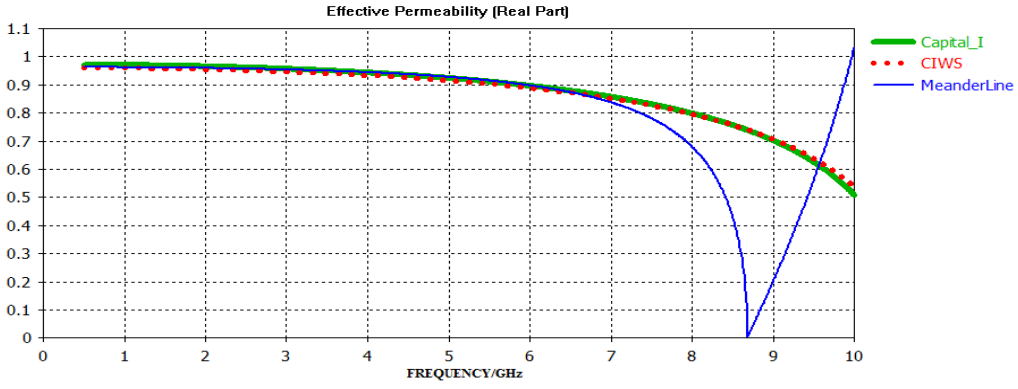

Figure 3.10. The real part of effective permeability for unit tell topologies

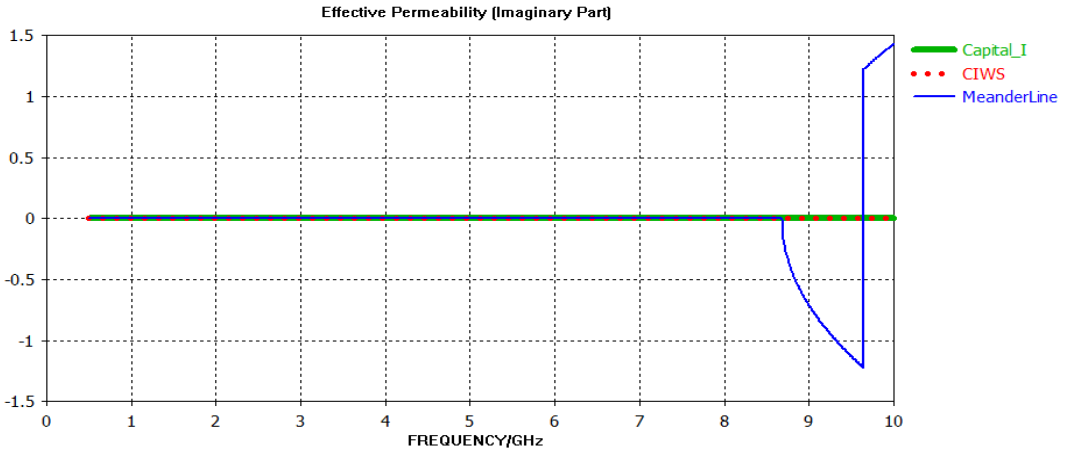

Figure 3.11. The imaginary part of effective permeability for unit tell topologies

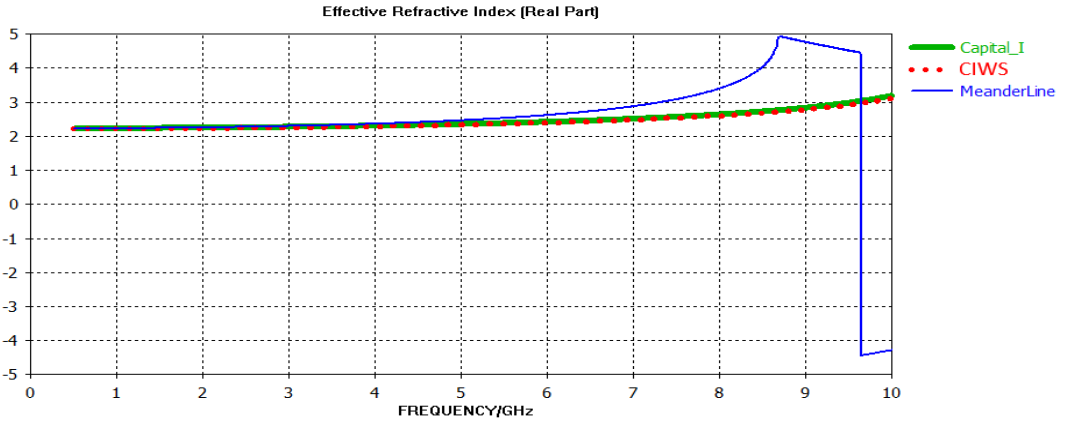

Figure 3.12. The real part of effective refractive index for unit tell topologies

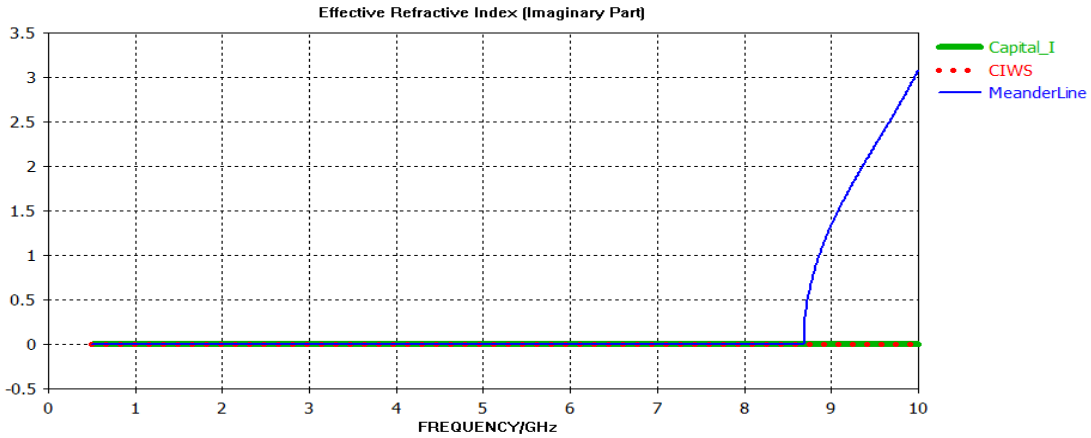

Figure 3.13. The imaginary part of effective refractive index for unit tell topologies

As expected, CIWS and CI topologies share similar frequency dispersion for constitutive parameters. Retrieved parameters for CIWS and CI structures are physically acceptable results since their imaginary parts are positive. Also, the retrieval method uses the Kramers-Kronig relationship to calculate real and imaginary parts of complex parameters. Therefore, effective parameters extracted for these array structures obey passivity and causality conditions. For the ML case, we observe negative amplitudes for imaginary parts of constitutive parameters which suggest an active medium producing energy on its own. These results violate the 2nd law of thermodynamics, hence they are incorrect. Frequency dispersion graphs of the ML structure indicate a resonance around 8.5 GHz. Negative signs for imaginary parts and "anti-resonant" response for permeability occurs near the resonance region. The retrieval method omits spatial dispersion effects which are most impactful around the resonance frequency. For this reason, the retrieval method should be used at frequencies far below the resonance point to yield physical results. Eigenmode analysis is incorporated into characterization efforts to cross-check results provided by the retrieval method and add a degree of accuracy.

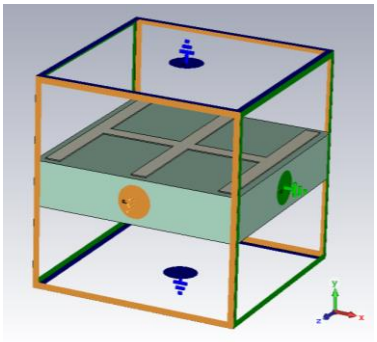

Figure 3.14. Resonator eigenmode analysis configuration

Simulation scheme used for the eigenmode analysis is shown in Figure 3.14. Walls in the –x-direction(outlined with green lines) and –y-direction(outlined with blue lines) are PEC and PMC, respectively. In the –z-direction (gold lines), the boundary condition is periodic which indicates that phase of the incident wave (a hypothetical wave since eigenmode analysis assumes the absence of the sources) progresses

alongside –z-direction. Thus, simulation configurations for both methods are identical.

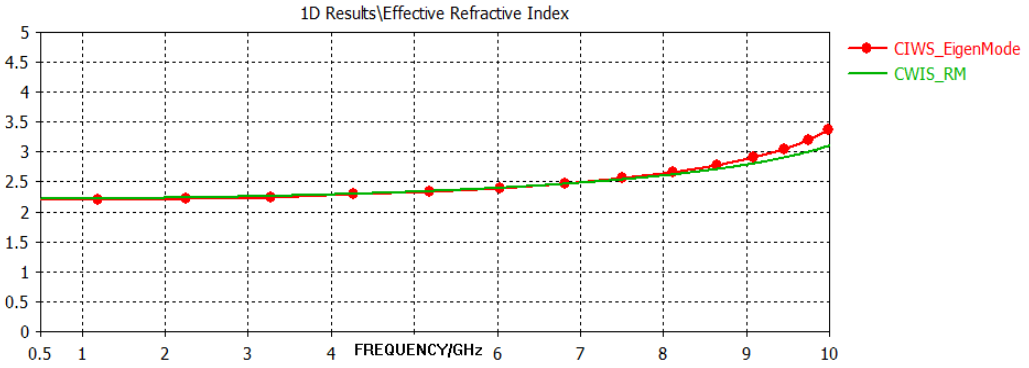

Figure 3.15. The retrieved refractive index of the CIWS unit cell for the retrieval method (RM) and for the eigenmode analysis

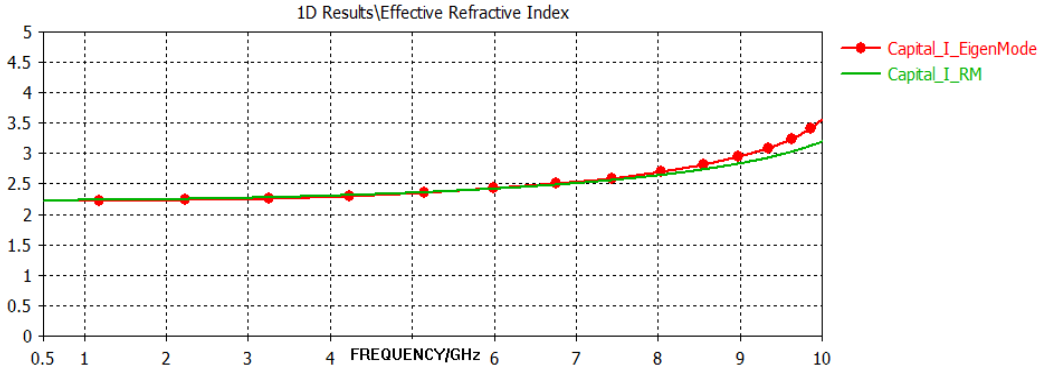

Figure 3.16. The retrieved refractive index of the Capital I unit cell for the retrieval method (RM) and for the eigenmode analysis

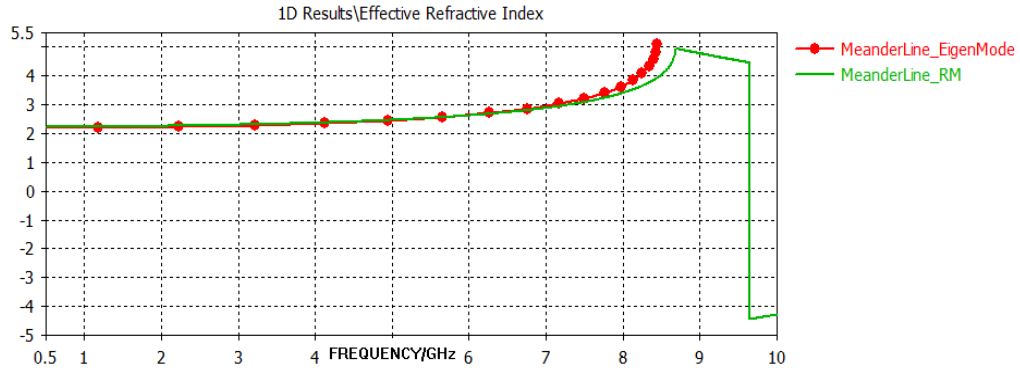

Figure 3.17. The retrieved refractive index of the Meanderline unit cell for the retrieval method (RM) and for the eigenmode analysis

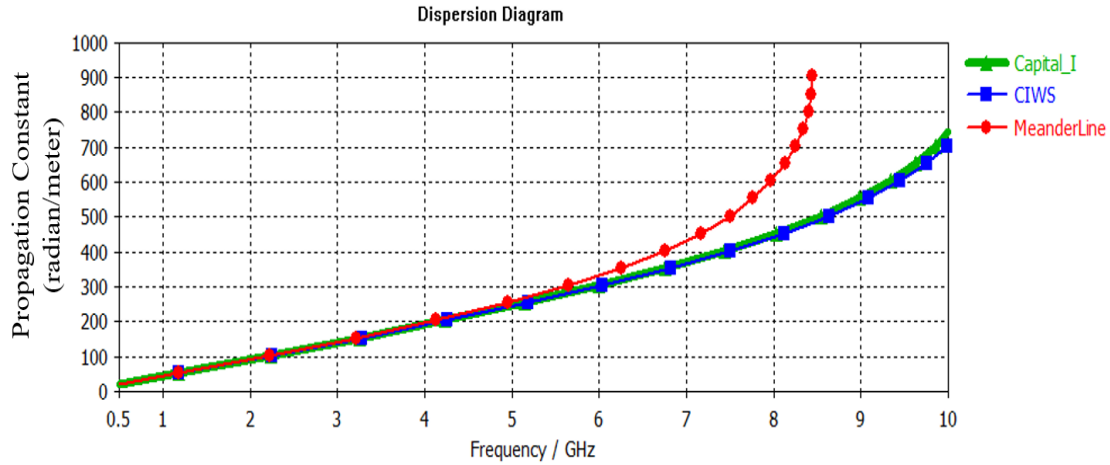

Figure 3.18. Dispersion diagram for different unit cell topologies

Effective refractive indices for both models are shown in Figure 3.15-17. For CIWS and CI topologies, refractive indices over frequency obtained by both methods are fairly close in 1-9 GHz band. There is a small deviation between them in 9-10 GHz band implying proximity to the resonance frequency.

On the other hand, the ML unit cell array displays a considerable discrepancy amongst results of both methods. In the dispersion diagram for the ML topology, it can be observed that cut-off frequency for the first eigenmode corresponds to a resonance point in the retrieval method around 8.4 GHz. This indicates the beginning point of another mode which is expected since metamaterials display extraordinary behavior around and after their resonance frequency. Therefore, the retrieved resonance frequency of the ML array is quite reliable in terms of accuracy. After the resonance point, the refractive index extracted by the retrieval method displays unphysical frequency dispersion where the sign of the imaginary part is negative. As demonstrated for these simulation results, the retrieval method coupled with eigenmode analysis yields more reliable information than the retrieval method regarding the extraction of medium parameters. Further analysis is carried out by inspecting electric-magnetic fields and surface currents over the unit cells.

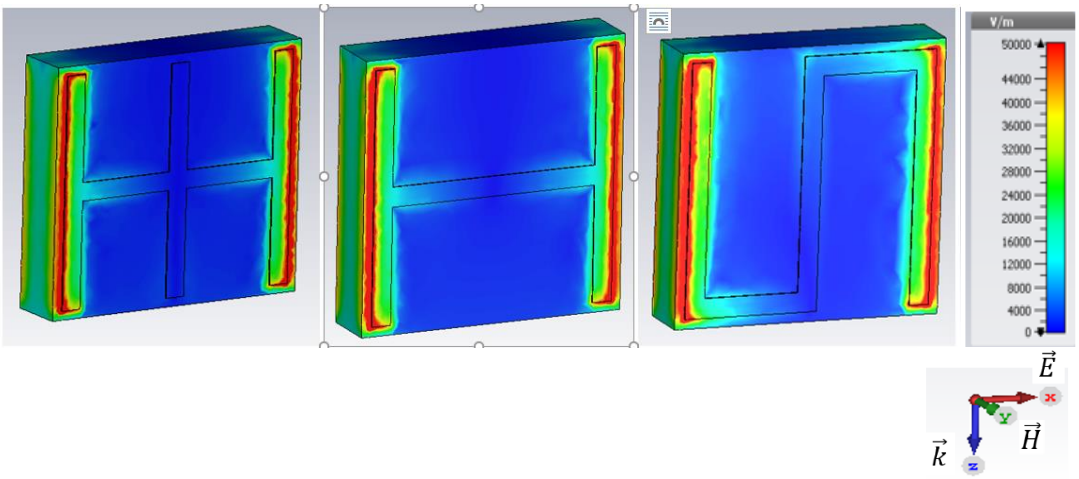

Figure 3.19. Electric field distribution for three different unit cell topologies at 6 GHz

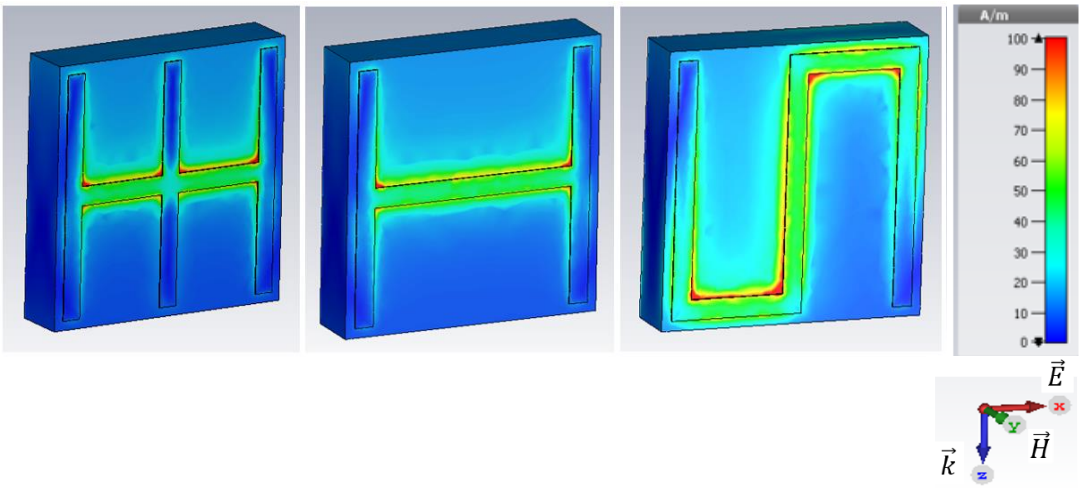

Figure 3.20. Magnetic field distribution for three different unit cell topologies at 6 GHz

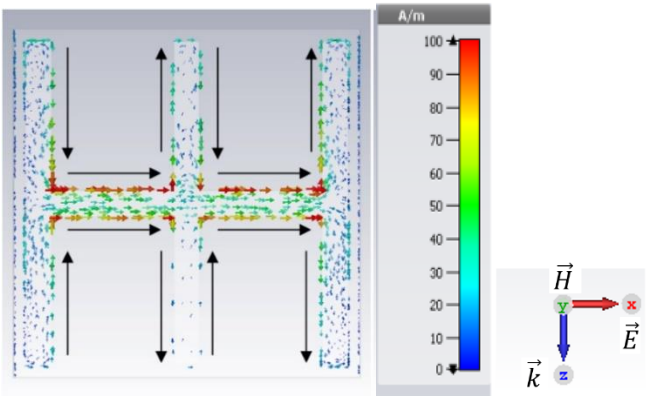

Figure 3.21. Surface current distribution for the CIWS unit cell topology at 6 GHz

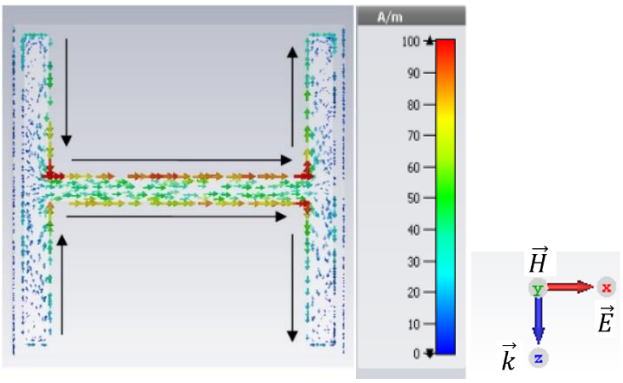

Figure 3.22. Surface current distribution for the CI unit cell topology at 6 GHz

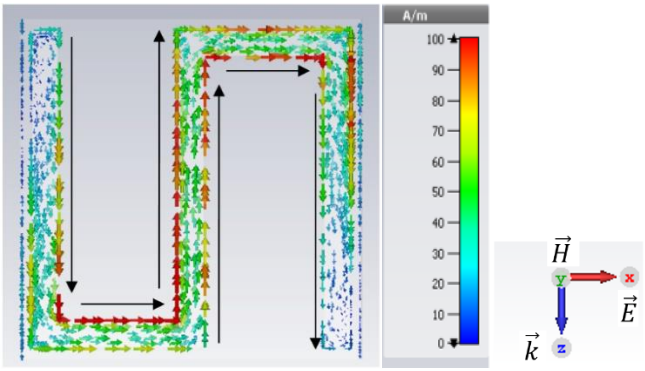

Figure 3.23. Surface current distribution for the ML unit cell topology at 6 GHz

For all these topologies, the electric field is directed along the x-axis, at the long edges of structures. The incident EM wave is –x polarized and propagates along–z-axis. Incident upon metallic inclusion, EM wave excites positive and negative charges on the surface of the unit cell which in response accumulate alongside the opposite edges of structure to create a countering electric field against the incident field. As seen in surface current plots, excited charges move towards the edges thereby creates surface currents over metallic inclusions. Positive and negative charges accumulated along the right and left edges create a strong electric field with opposite sign charges of the neighboring unit cell edges. This effect is clearly shown in electric field distribution plots for all specimens where E-field is massively concentrated along the longitudinal edges of the unit cells. On the contrary, the magnetic field is not particularly confined over any area of the cells. A close inspection over surface current directions can enlighten this result in particular.

Dividing unit cell in subareas (2 for CI and ML and 4 for CIWS), it is seen that circulating surface which are induced by the incident electric field creates a secondary magnetic field (primary fields are related to excitation EM field) for each subarea. Furthermore, the direction of the magnetic field formed by these currents in the subareas is opposite, which results in the cancellation of magnetic fields in the subareas. There is an asymmetry present in the surface current amplitudes circulating the subareas due to combined effect of primary and secondary magnetic fields. Therefore, full cancelation of the magnetic response of the unit cells is not observed. Thus, magnetic responses of unit cells are significantly lesser compared to electric responses. Therefore, we can conclude that these structures in this excitation configuration over this frequency band are mostly electrically responsive. This conclusion is supported by the retrieved parameters of the unit cells where permittivity of the structures increase with frequency and permeability is fairly stable along this specific operation bandwidth.

Same unit cells are simulated with 90-degree rotation concerning the normal axis of the structures to observe the effects of orientation. New simulation scheme is called broadband configuration and illustrated in Figure 3.24. The polarization of incident field, boundary conditions in each direction and effective phase distance (deembbeding procedure) are identical for both setups. The major difference between two excitation configurations is that horizontal edges are perpendicular to PEC walls and parallel to incident E-field in the new scheme.

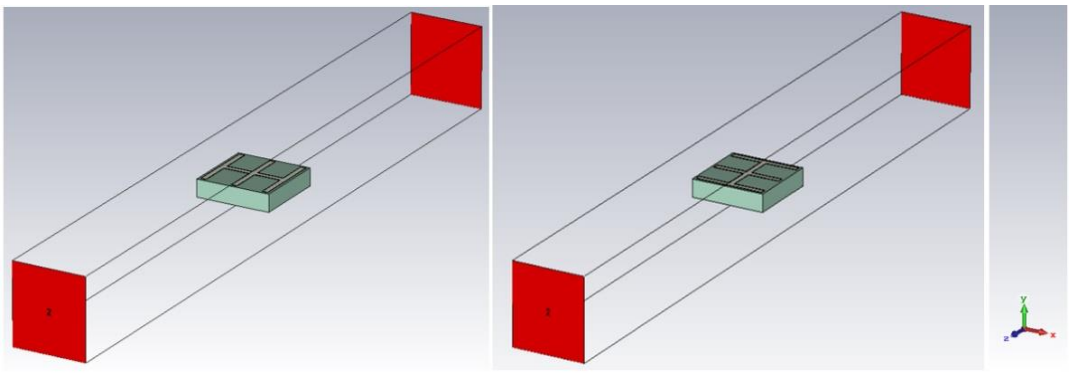

Figure 3.24. Simulation configurations for broadband and resonant settings

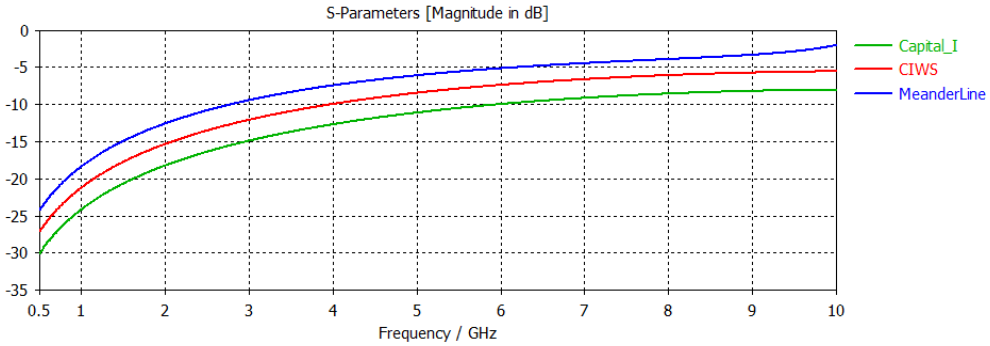

Figure 3.25. Return loss (S11) for unit tell topologies

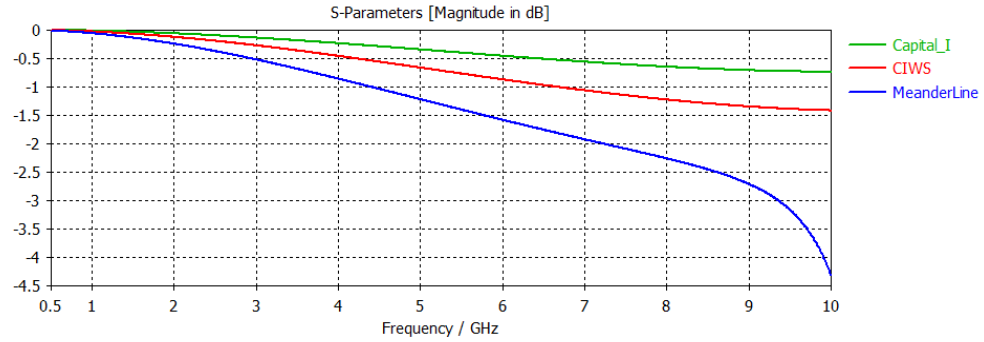

Figure 3.26. Transmission loss (S21) for unit tell topologies

Scattering parameters over frequency for the broadband setup is displayed in Figure 3.25-26. Compared to the resonant counterpart, more energy is transmitted to the receiving port. There are no visible spikes in the scattering parameters as opposed to the resonant scheme. It is reasonable to expect that these unit cells may not be resonant under this excitation configuration in this bandwidth.

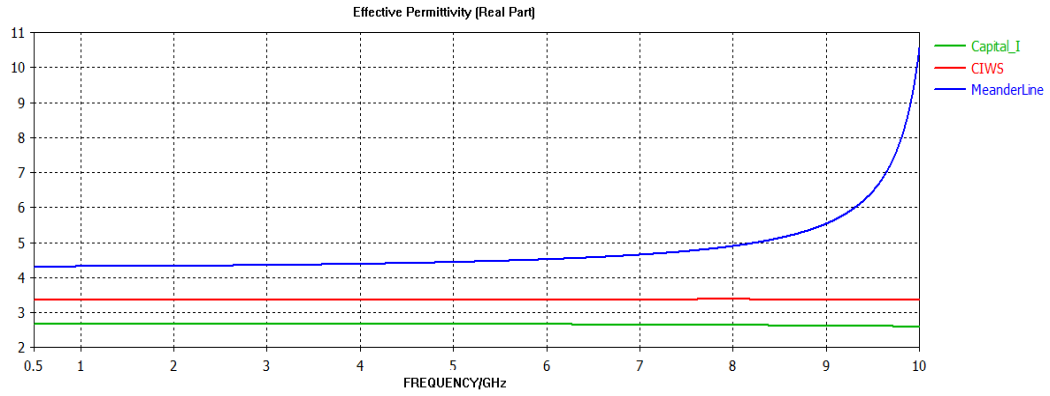

Figure 3.27. The real part of effective permittivity for unit tell topologies

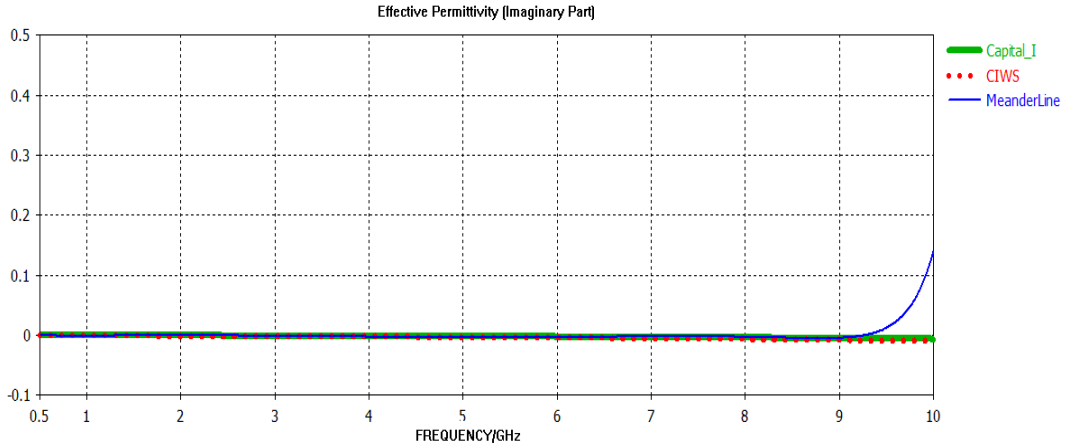

Figure 3.28. The imaginary part of effective permittivity for unit tell topologies

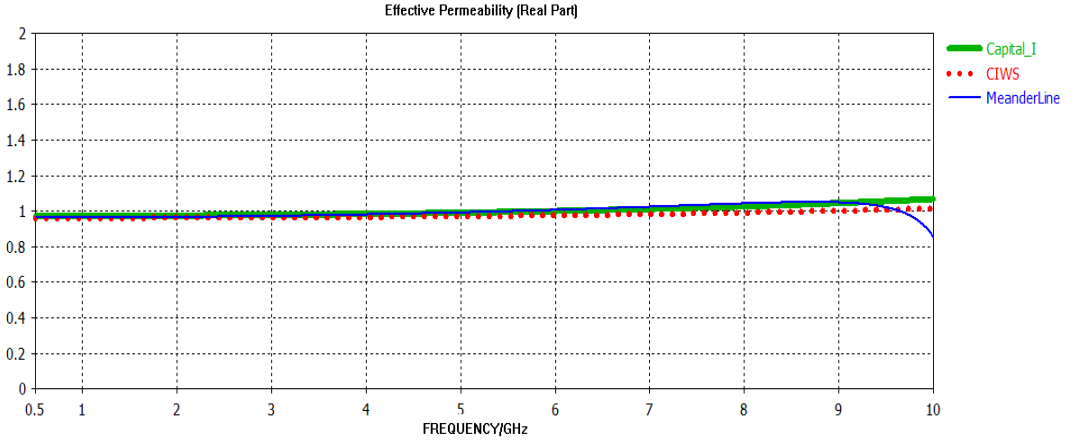

Figure 3.29. The real part of effective permeability for unit tell topologies

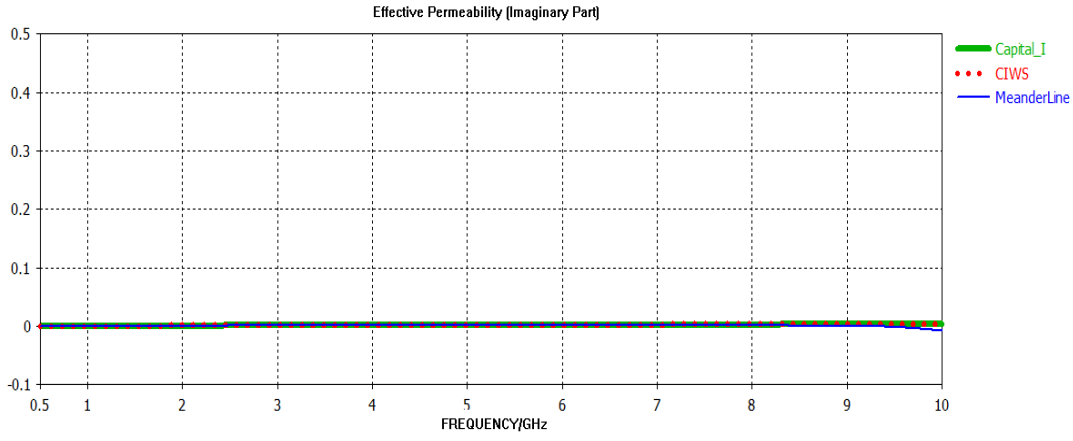

Figure 3.30. The imaginary part of effective permeability for unit tell topologies

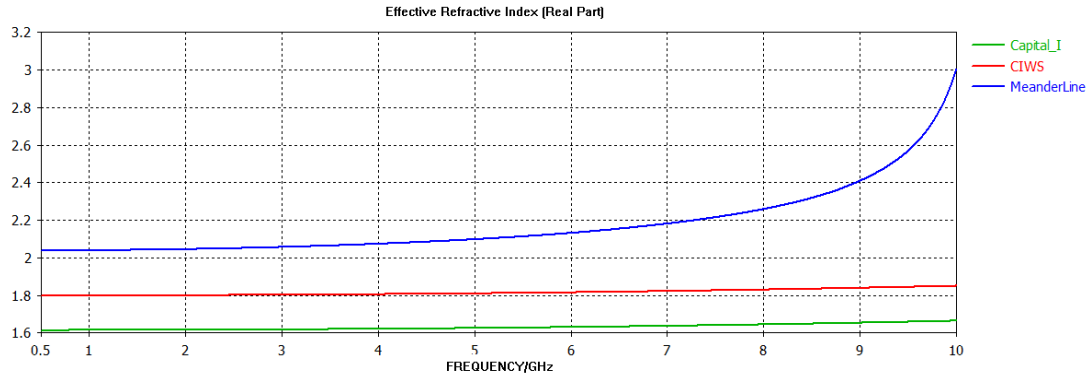

Figure 3.31. The real part of effective refractive index for unit tell topologies

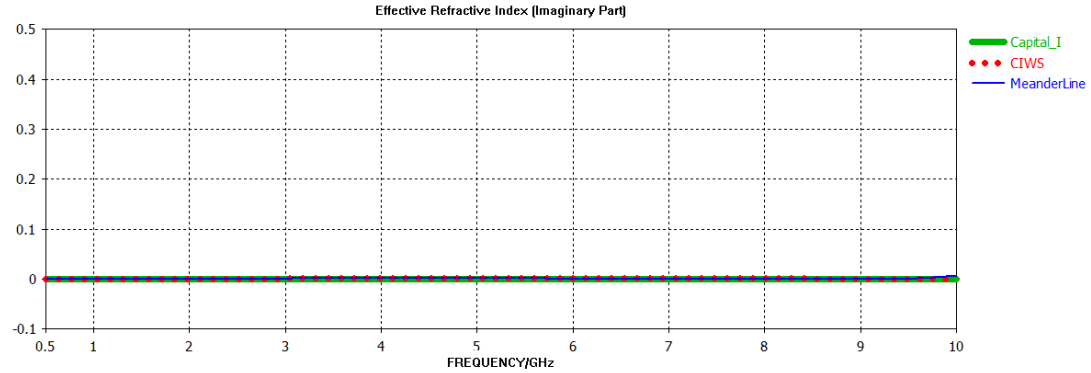

Figure 3.32. The imaginary part of effective refractive index for unit tell topologies

Frequency dispersion for effective parameters is alike if not the same for three topologies. Naturally, CIWS and CI share more similar behavior amongst each other with some amplitude difference in real part of effective permittivity. ML structure displays a steep increase for effective permittivity near 10 GHz and a decrease for effective permeability which can suggest proximity to the resonance frequency. One striking difference for retrieved parameters of the different orientations is that resonant configuration has considerably larger values for effective permittivity and refractive index. Effective permeability is slightly larger in the broadband configuration. CIWS and CI geometries display imaginary physical parts throughout the operation bandwidth. As opposed to the resonant scheme, ML structure displays negative sign imaginary parts for effective parameters only nearby of 10 GHz. In the rest of the band, retrieved parameters of all specimens are physical in terms of

passivity and causality conditions. Broadband simulation scheme is shown in Figure 3.33. Simulation configurations are identical with a single difference in orientation of the unit cell.

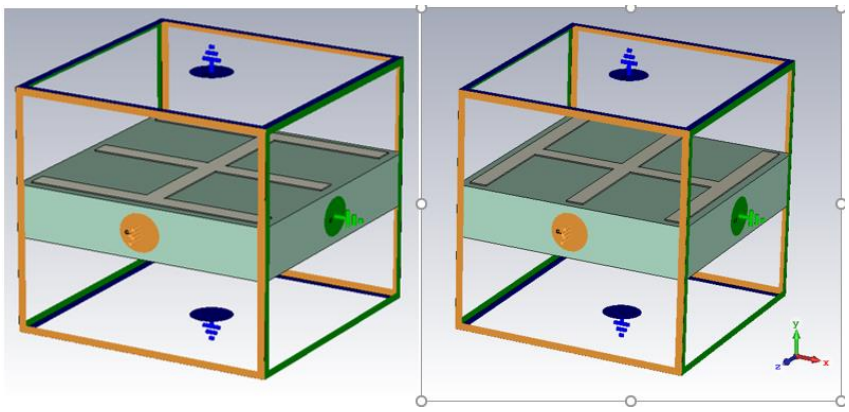

Figure 3.33. Eigenmode simulation configurations for broadband (left) and resonant (right) settings

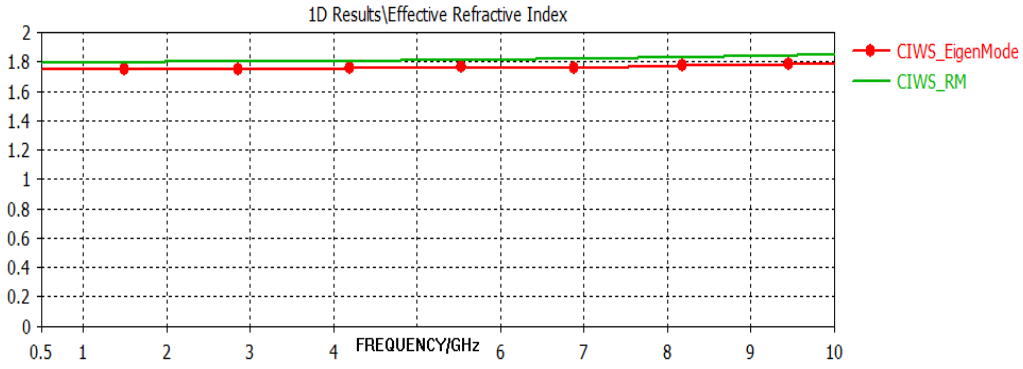

Figure 3.34. The retrieved refractive index of the CIWS unit cell for the retrieval method and eigenmode analysis

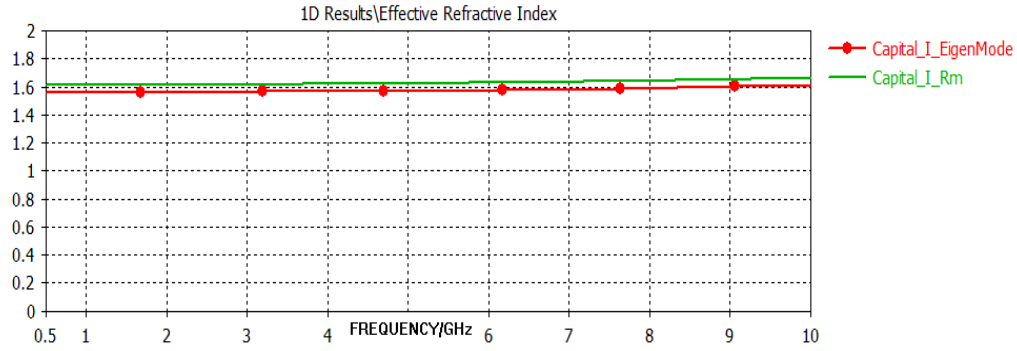

Figure 3.35. The retrieved refractive index of the Capital I unit cell for the retrieval method and eigenmode analysis

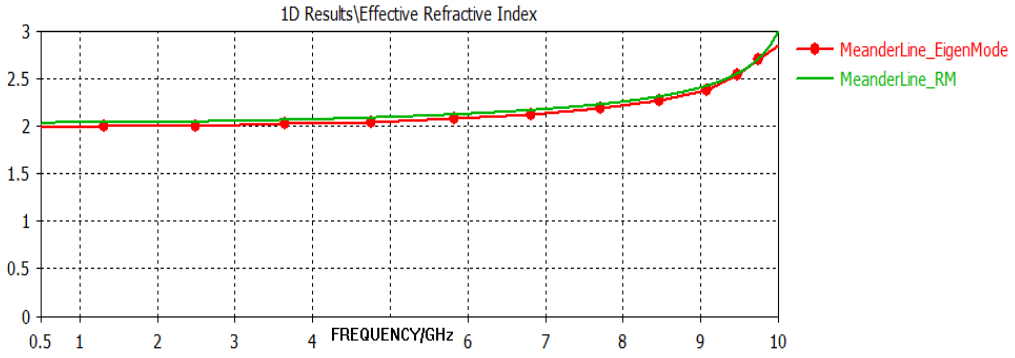

Figure 3.36. The retrieved refractive index of the Meanderline unit cell for the retrieval method and eigenmode analysis

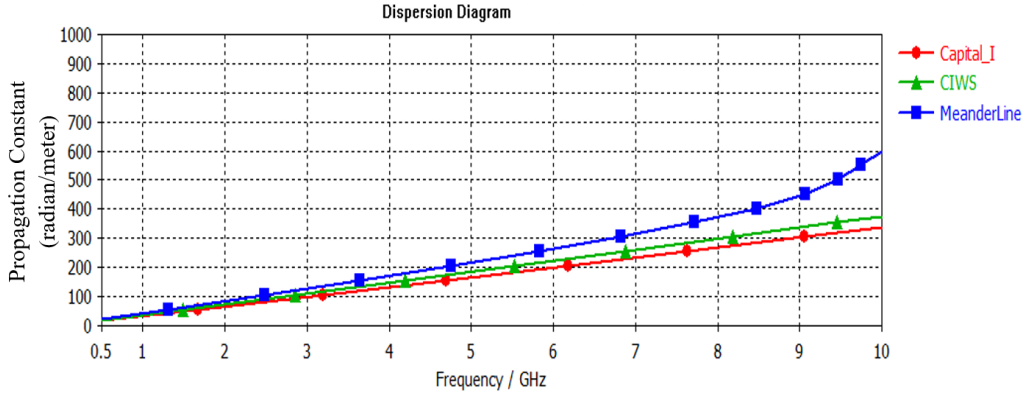

Figure 3.37. Dispersion diagram for the unit cells

Effective refractive indices for broadband orientation retrieved by both characterization methods are shown in Figure 3.34 through Figure 3.36. For all specimens, refractive indices over frequency obtained by both methods are fairly close in 1-10 GHz band. Unlike the resonant orientation, the ML unit cell does not display a discrepancy for the results of both methods. Parallel with findings from the resonant scheme, cut-off frequency for the first eigenmode is not in 1-10 GHz bandwidth which was expected since there is no resonance in the bandwidth. Since metallic inclusions are fairly small compared to the wavelength and excited far below resonance frequencies of each specimen, eigenmode analysis, and retrieval method yielded close results which are abiding passivity and causality conditions. Further analysis is carried out by inspecting electric-magnetic fields and surface currents over the unit cells.

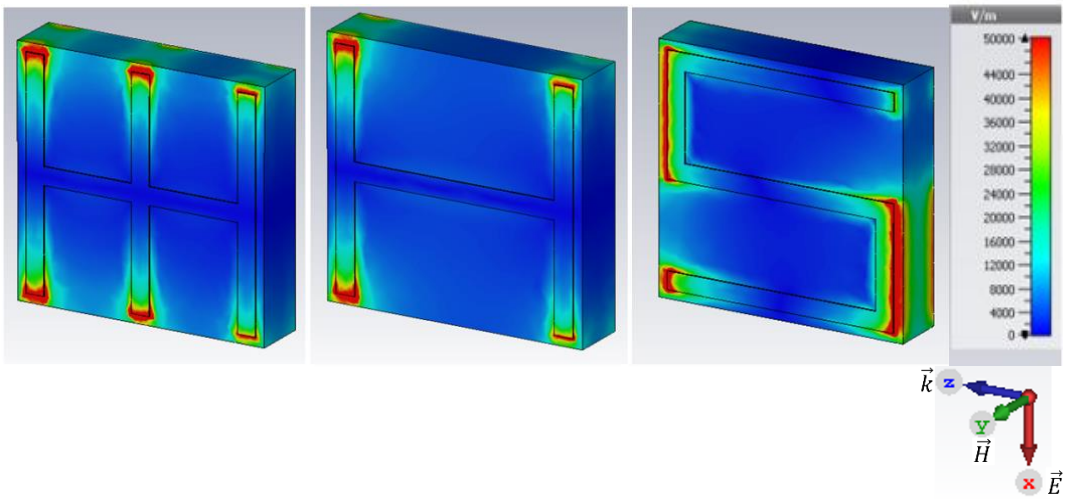

Figure 3.38. Electric field distribution for three different unit cell topologies at 6 GHz

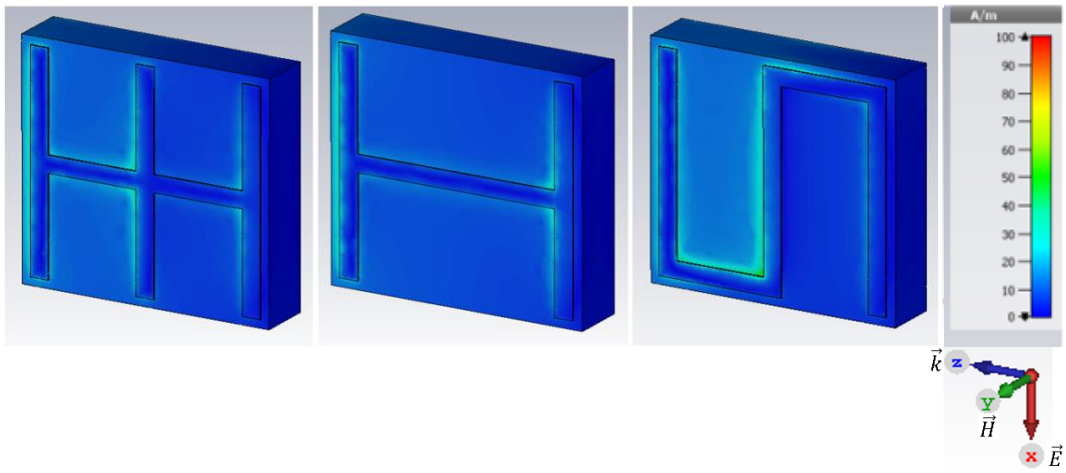

Figure 3.39. Magnetic field distribution for three different unit cell topologies at 6 GHz

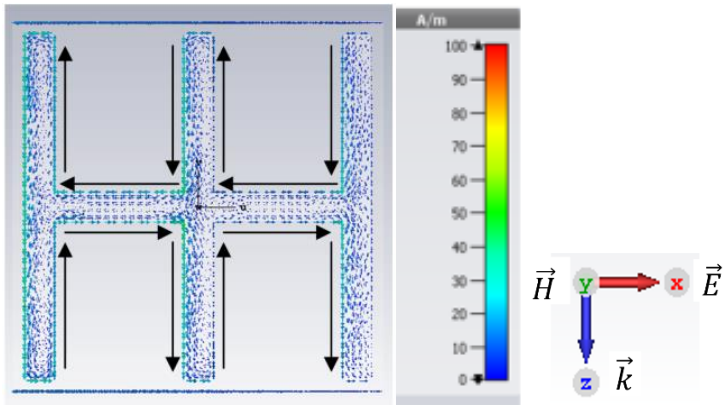

Figure 3.40. Surface current distribution for the CIWS unit cell topology at 6 GHz

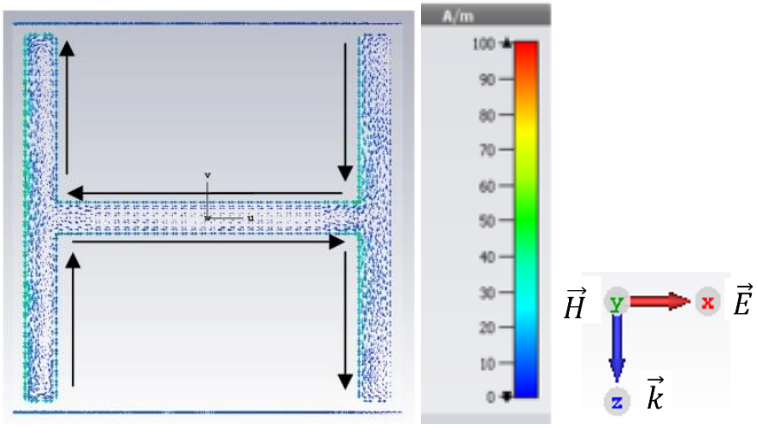

Figure 3.41. Surface current distribution for the CI unit cell topology at 6 GHz

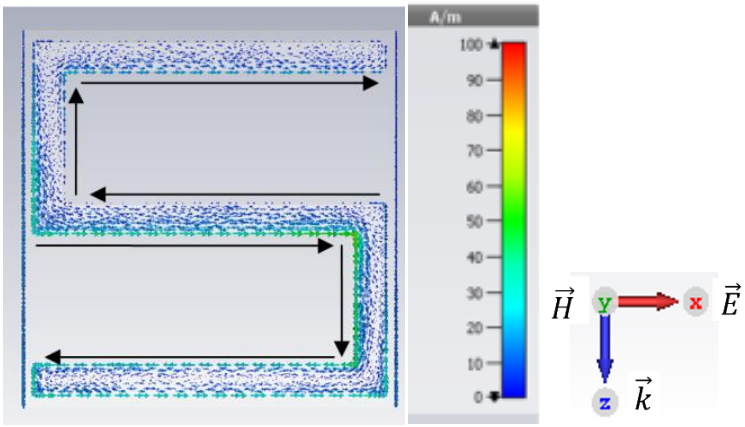

Figure 3.42. Surface current distribution for the ML unit cell topology at 6 GHz

For all specimens, the electric field is concentrated along –x-axis, at the short edges of structures. The incident EM wave is –x polarized and propagates along–z-axis. Incident upon metallic inclusion, EM wave excites positive and negative charges on the surface of the unit cell which in response accumulate alongside the opposite edges of structure to create a countering electric field against the incident field. Accumulated charges form a dipole which is similar to the physics of natural materials. Instead of molecular dipoles, meta-atom (unit cells) dipoles come into existence. As seen in surface current plots, excited charges move towards the edges thereby creates a surface current over metallic inclusion. Positive and negative charges accumulated along the edges create a strong electric field with opposite sign charges of neighboring unit cell edges. This effect is clearly shown in electric field

distribution plots for all specimens where E-field is hugely concentrated along the short edges of the unit cells. Compared to the resonant configuration, a considerably smaller area contains a concentrated electric field. Retrieved effective permittivity is larger in the resonant case for the entire bandwidth which coincides with the results of electric field distributions. Magnetic field plots are in good agreement with the resonant case. There is no area of confinement over the unit cell since counter-rotating surface currents create canceling magnetic fields analogous to the resonant case. Therefore, we can conclude that these structures in this excitation configuration are indeed electrically resonant. This conclusion is supported by the retrieved parameters of the unit cells where permittivity of the structures increase with frequency and permeability is fairly stable along the operation bandwidth. However, as suggested by frequency dispersion plots of constitutive parameters, the amplitude of the electrical response is greater for the resonant case due to the orientation. Although it provides the advantage of a higher refractive index, the resonance frequency is lower which can limit the bandwidth of the system incorporating the cells. Conversely, broadband oriented cells can operate in larger bandwidth at the expense of lower refractive index.

3.5. Metasurface Integrated Antipodal Vivaldi Antenna

In this section, the design of the substrate integrated metasurface lens will be elaborated. Lens structure will be incorporated into the wideband Vivaldi antenna explained in the first chapter. Various properties including unit cell structure, lens geometry, unit cell orientation, lens/unit cell sizes and lens positioning concerning the antenna were tested. Specimen with optimum efficiency and best directivity characteristics are selected for the GPR system.

An example placement of the metasurface lens into the antenna system is given in Figure 3.43. Antenna and metasurface lens are etched to the same dielectric substrate and are physically close to each other. Since metasurface lens is definitely in the

near-field of the antenna, behavior of EM wave traveling in this area must be known to synthesize a working lens. As explained previously in this chapter, the polarization of the incident wave is critical to metamaterial EM response.

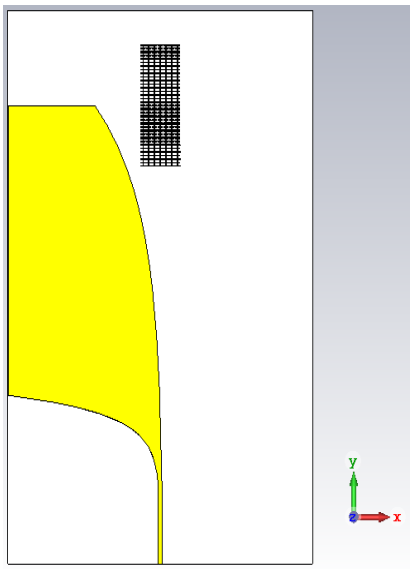

Figure 3.43. A generic layout for metasurface lens integrated antenna

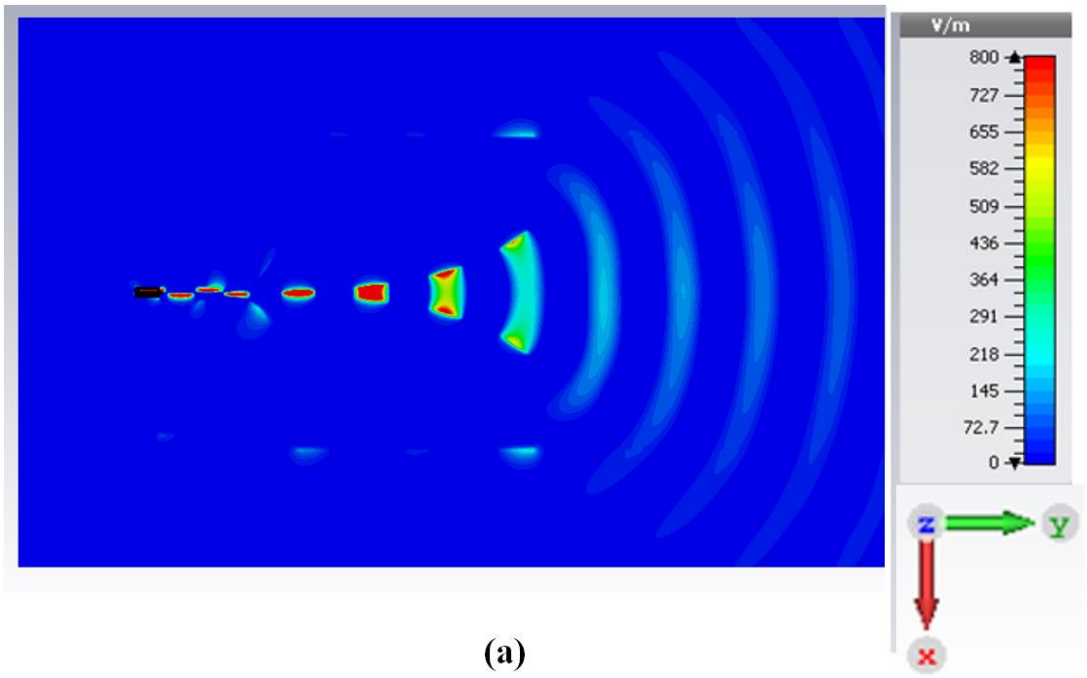

(a)

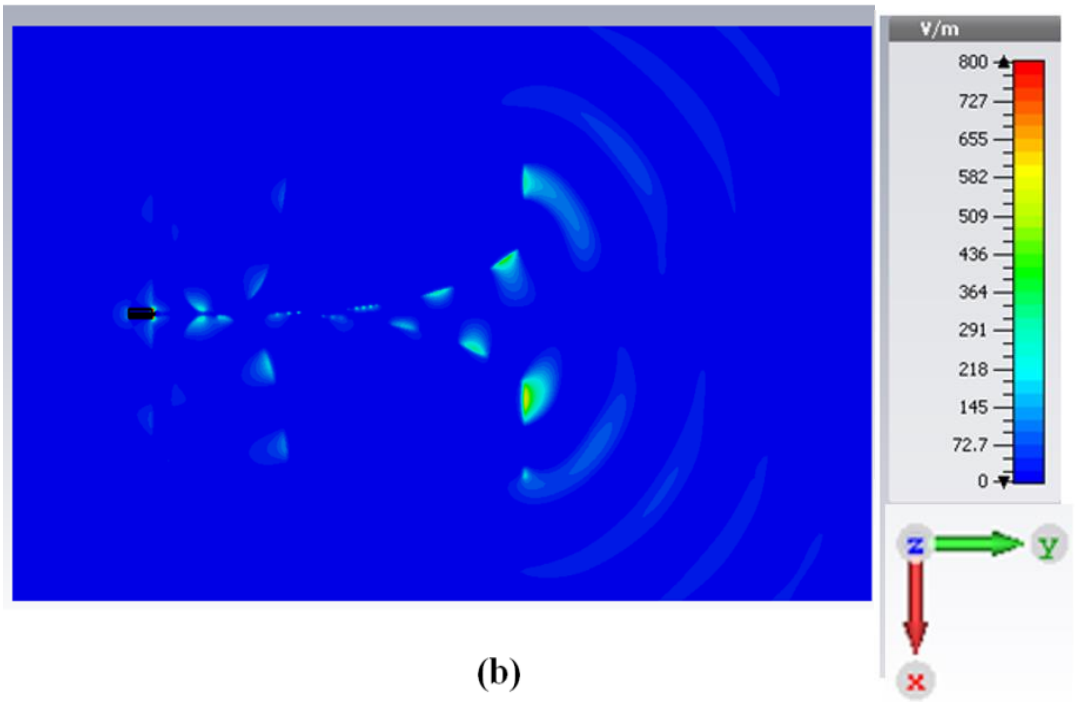

(b)

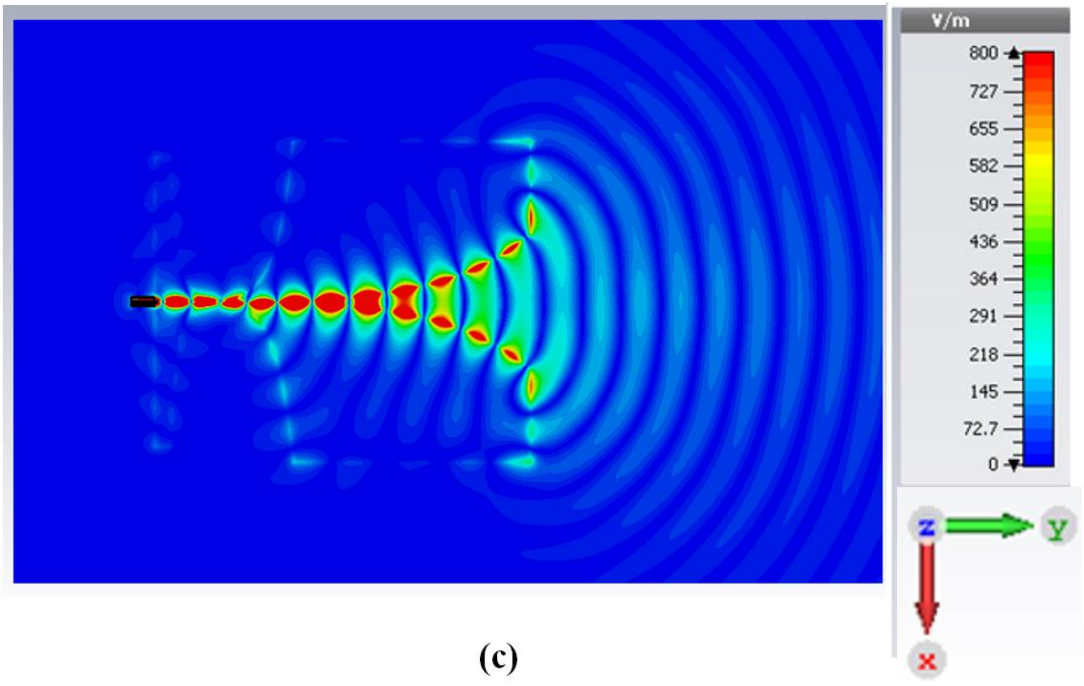

(c)

Figure 3.44. Electric field distribution of Vivaldi antenna for vector components at 6 GHz, (a) –x-component, (b) –y-component, (c) absolute value of E-field

Observations on the electric field plots clearly show that bulk of the radiated power is –x polarized. It is natural to observe electric field polarized in the propagation direction since the plot illustrates the near field of the antenna. Nevertheless, initial design steps should be taken acknowledging –x polarized field. The orientation of the cells will be by a broadband configuration where longer sides of the unit cells are parallel to the incident wave. Since broadband orientation offers greater bandwidth before resonance, it is utilized as a primary placement pattern in this work.

3.6. Metasurface-Antenna Near-Field Interaction

The underlying physics of the interaction between antenna and lens should be elucidated to design a lens for antenna systems. In this case, the metasurface body is used as radiation enhancer which may be quite different from the standard lenses in terms of EM properties. Only after gaining intuition about the interaction can engineer design an optimized system. Two identical antennas are simulated with different lens geometries. Positions of the lenses differ whereas unit cells are the same. For reference purposes, specimens will be addressed as the small and the large lenses.

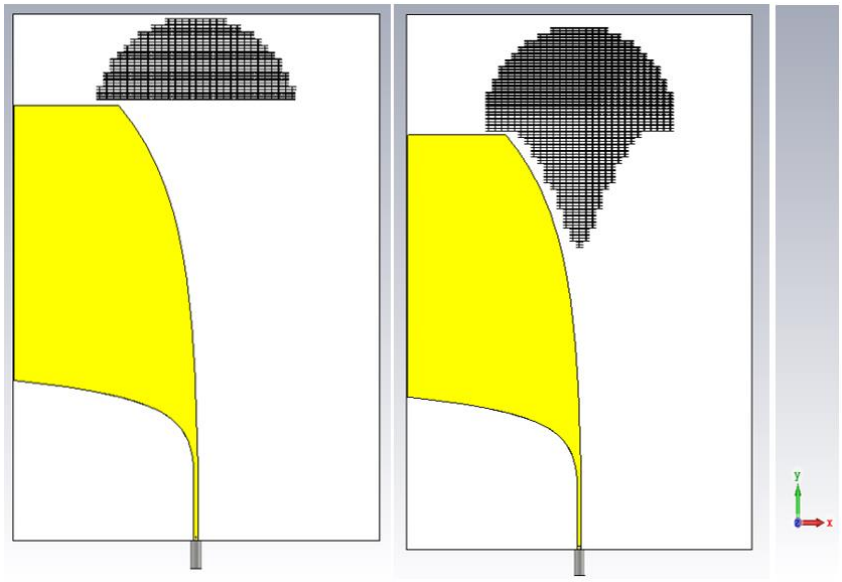

Figure 3.45. Substrate integrated lens structures with different properties, small lens (on the left), large lens (on the right)

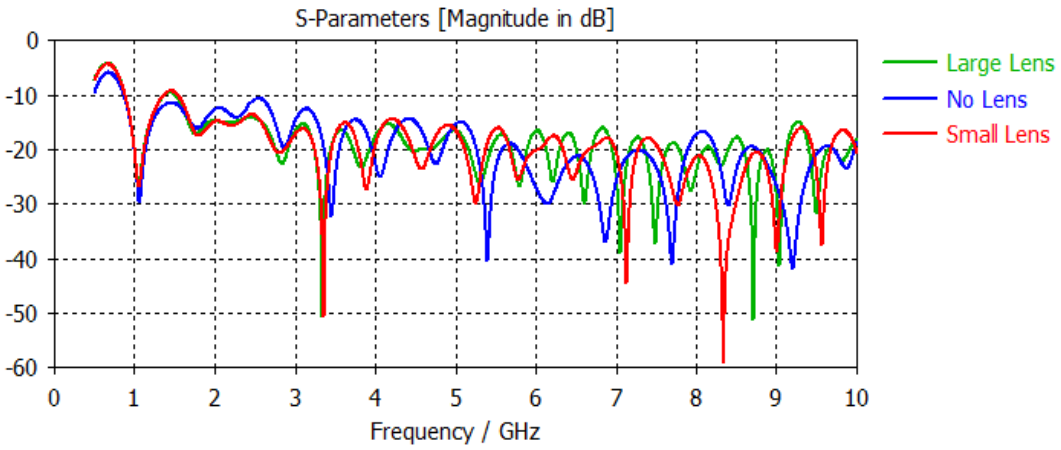

Figure 3.46. Return loss characteristics for antennas with different lens structures

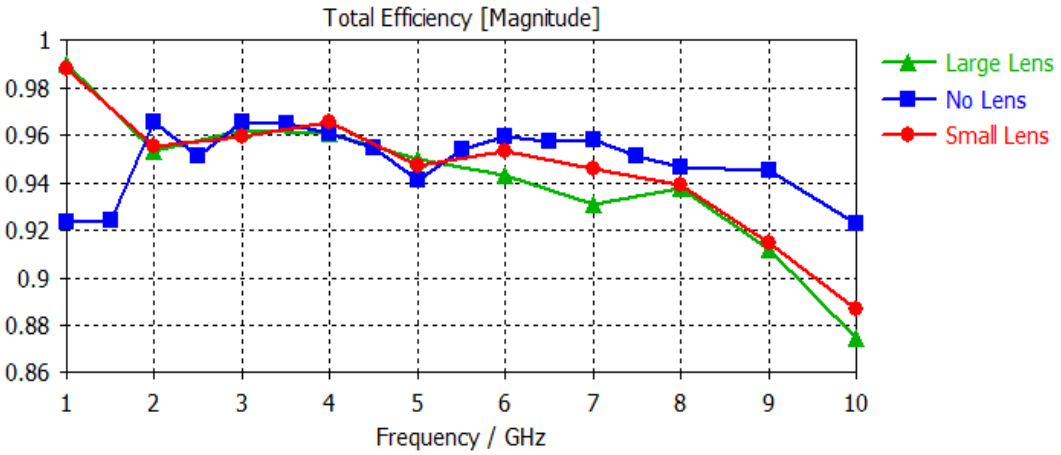

Figure 3.47. Total efficiencies for antennas with different lens structures

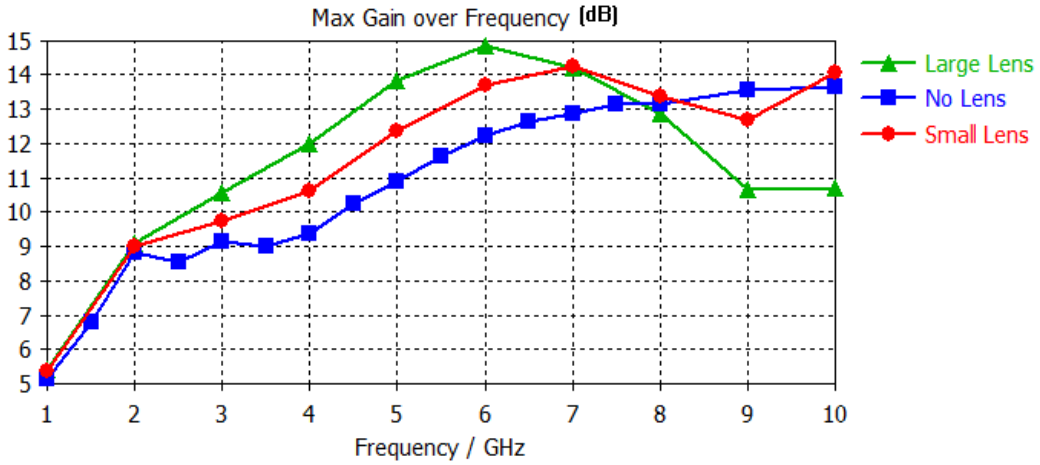

Figure 3.48. Realized gain for antennas with different lens structures

Efficiency and return loss characteristics for the three antenna systems are fairly close in 1-6 GHz bandwidth. In 1-2 GHz bandwidth, original antenna (antenna without any metasurface lens) has slightly better efficiency over antennas with metasurface lens structure while the vice versa is valid in the 2-6Ghz bandwidth. Although return loss characteristics compare in the same manner, antennas with lensing structure experience a marked drop in the efficiency after 6 GHz. This trend shows its effect in the gain dispersion where metasurface integrated structures start a decline in the gain at 6GHz which is followed by the takeover approximately at 8 GHz where the standard Vivaldi antenna has higher gain. After 2 GHz, an antenna with a larger lens has the highest gain followed by a smaller lens and original design. Interestingly, the decline in the gain for a larger lens starts before the smaller lens integrated antenna which assumes the same value at 7 GHz. Electric field distribution chosen at 2 distinct frequencies is investigated to understand the underlying EM interaction which causes positive and negative effects of the lensing structure depending upon the operation frequency.

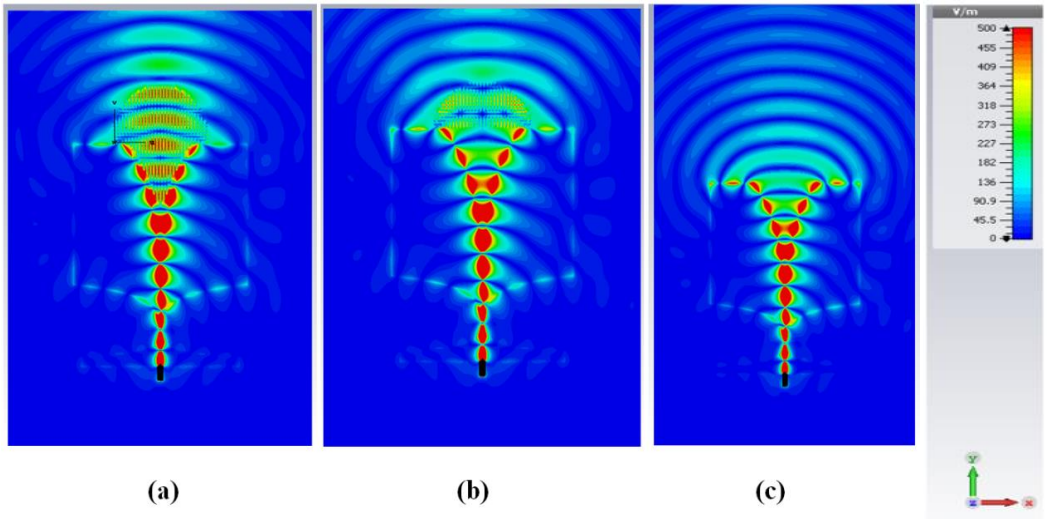

Figure 3.49. Electric field distributions of the antennas at 5 GHz, top view, (a) large lens, (b) small lens, (c) original antenna

Phase front in the original design expands cylindrically in E and H- planes. Electric field expands as it moves along the space and amplitude of the wave decreases proportionally with the cube of the traveled distance. The antenna with a smaller

metasurface lens has somewhat more planar expanding wave compared to the original design in the E-plane. The Effect of the lens is more distinct in the H plane in which the outer edges of the incident phase front starts to bend inwards and flatten the wave. In other words, the middle part of the wave which interacts most with the metallic inclusion has lower phase velocity so that field at the edges can reduce the path length difference. This phenomenon is more intense in the antenna with a larger metasurface lens.

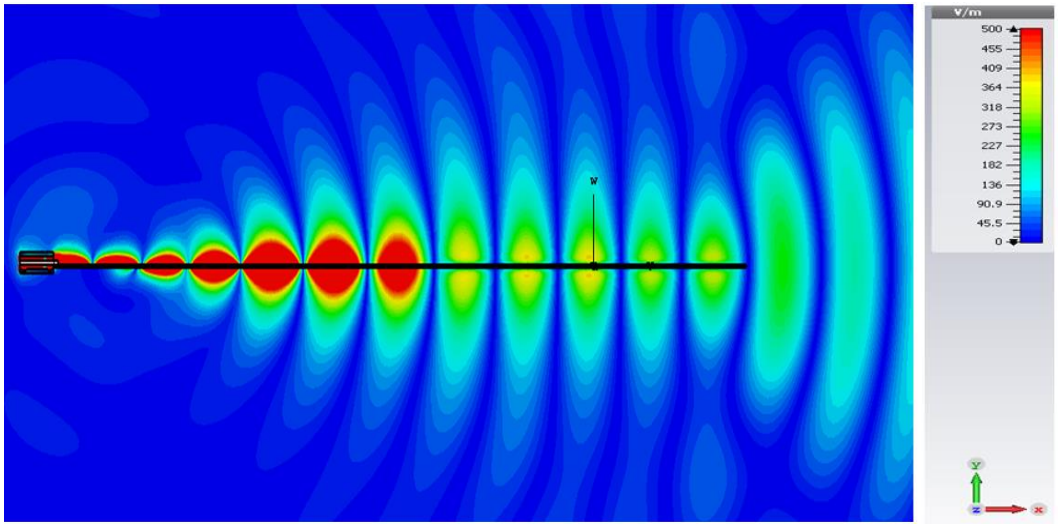

(a)

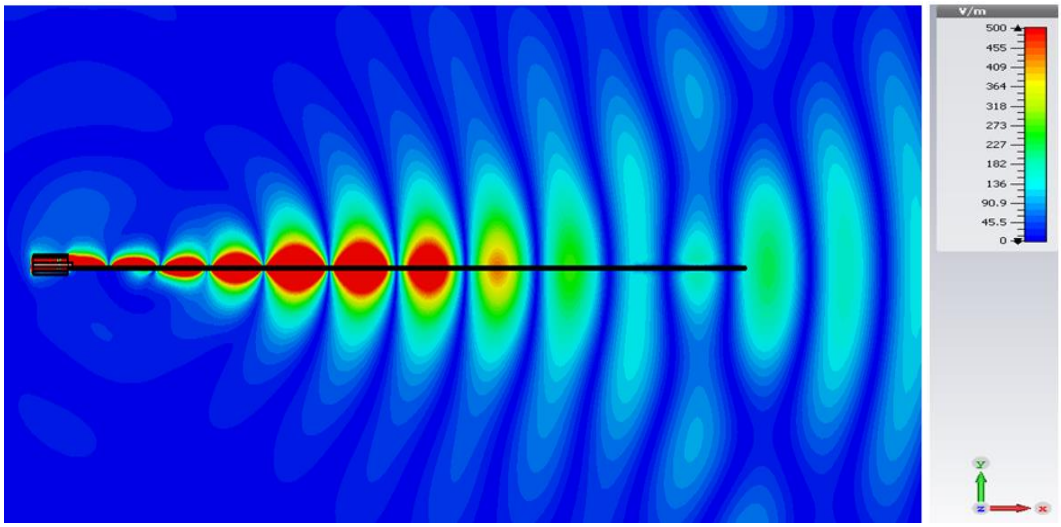

(b)

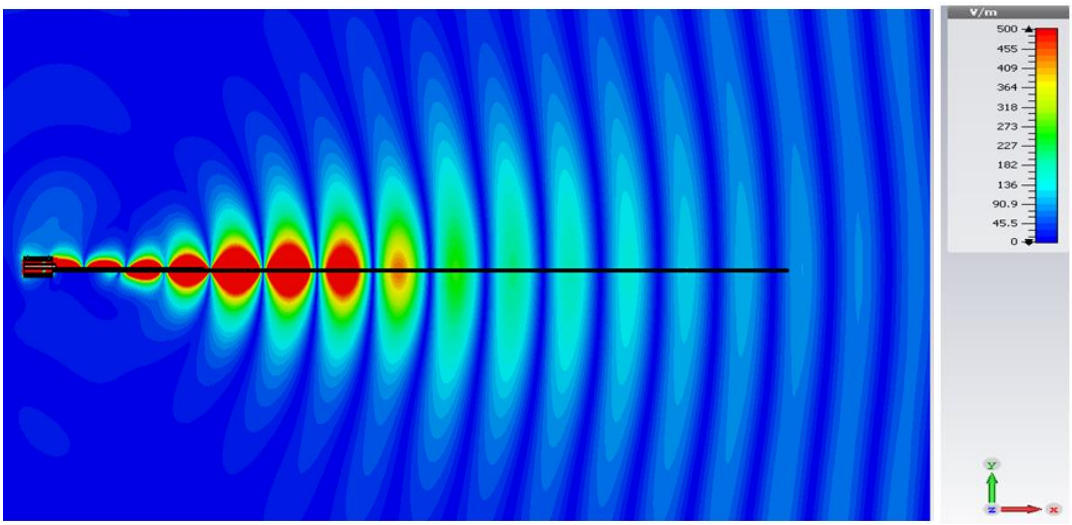

(c)

Figure 3.50. Electric field distributions of the antennas at 5 GHz, side view, (a) larger lens, (b) smaller lens, (c) original antenna

Phase front in the E-plane is nearly planar. In the H-plane, wave flattens in the same manner with E-plane, and the effective length of the wavefront decreases as the wave travels along the lens. This extraordinary behavior of the wave stems from the interaction between metasurface and EM field. Incident upon metallic inclusion, EM field excites surface currents which then creates strong localized electric fields between the unit cells. This mechanism repeats cell after cell as the wave travels across the metasurface. The manner of transmission of the wave is analogous to transmission in the waveguide. Therefore, in this thesis, this phenomenon is refered the waveguiding effect. Essentially, a significant amount of the power of incident EM field is confined between metallic inclusions so that EM field cannot expand as spherically as it did in the original antenna. This physical mechanism is the underlying reason for the performance enhancement of the antenna by the metasurface lens structure.

In the smaller lens antenna, the metasurface structure starts at the end of the flares of the Vivaldi antenna. The field in the H-plane experiences a split towards the end of the lensing structure. Outer edges of the wave tend to detach from the main

wavefront throughout the lens. This effect is considerably mitigated in the antenna with a larger lens where lensing structure starts between metallic flares of the Vivaldi antenna. This phenomenon is a direct result of the waveguiding effect. In the antenna with a larger lens, metasurface interacts with a less spherically expanded wave compared to the other case. Therefore, a greater portion of the field is confined between the unit cells which results in a more homogenous phase velocity distribution along the wavefront. In the antenna with a shorter lens, a smaller portion of the wave is confined and slowed down, and the field at the edges are less affected by the metallic inclusions which means that their phase velocity is not reduced by the same amount. Thus, the outer edges of the field detaches from the wavefront creates a split in the electric field distribution. Depending upon the severity of the divergence, radiated beams can split which can severely deteriorate the antenna performance. Consequently, it is more advantageous to place the beginning of the metasurface deeper in the antenna.

In order to further elaborate on the underlying physical mechanisms here, a homogenous dielectric slab having similar EM properties to metasurface lens is placed into antipodal Vivaldi antenna.

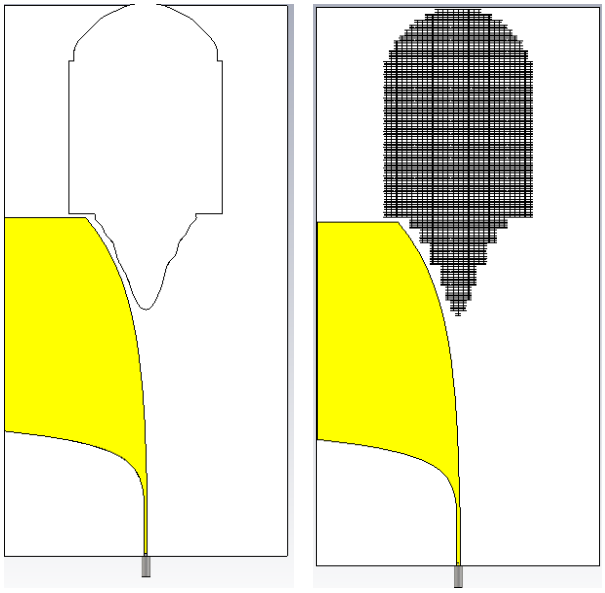

Figure 3.51. Metasurface and dielectric lens integrated Vivaldi antennas

In Figure 3.51, metasurface and dielectric lens loaded antipodal vivaldi antennas are shown. The antennas are identical except the lens strucutures. In the dielectric lens integrated antenna, black outlines indicate the borders for dielectric lens. Substrate material for the dielectric lens is Alumina which has 9.4 dielectric constant and 0.004 loss tangent at 10 GHz.

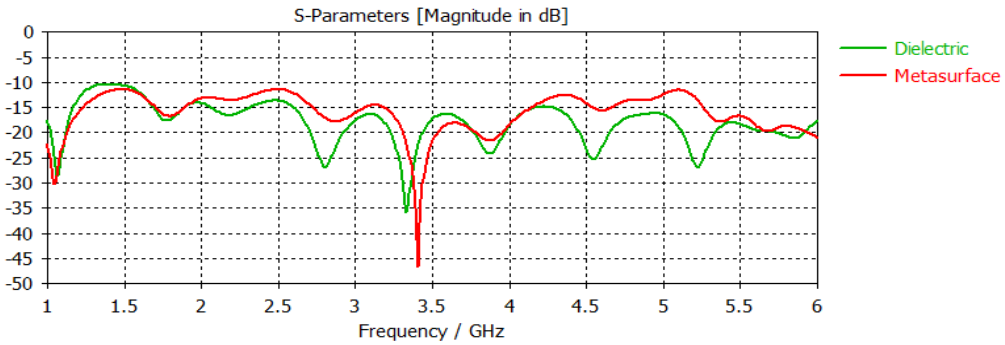

Figure 3.52. S-parameters for dielectric and metasurface lens integrated Vivaldi antennas

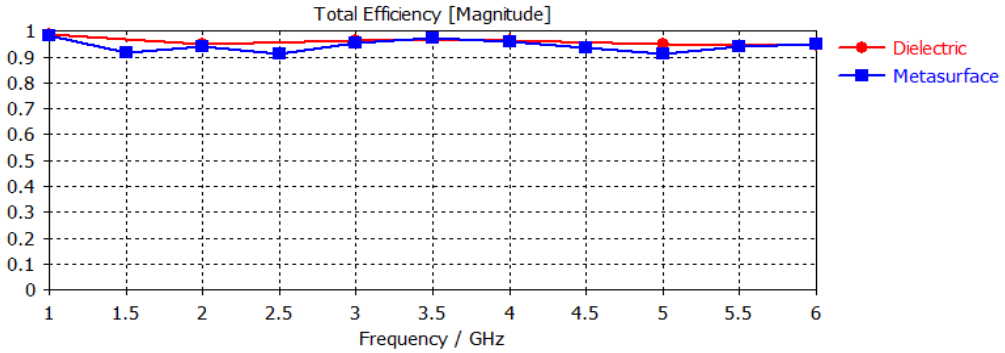

Figure 3.53 Total efficiencies for dielectric and metasurface lens integrated Vivaldi antennas

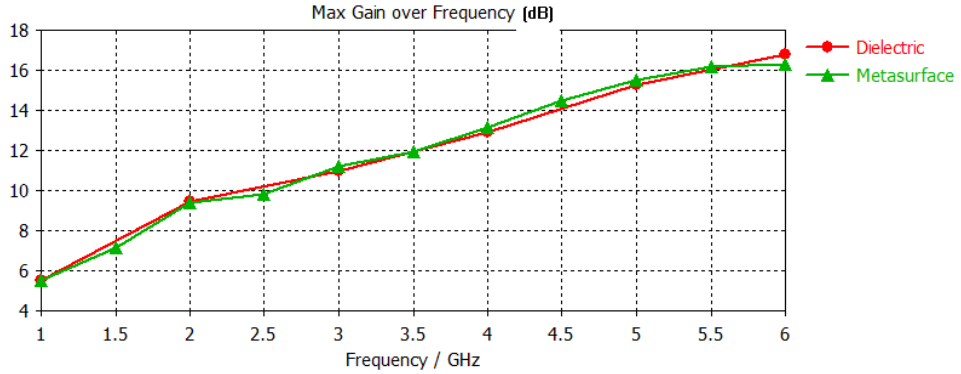

Figure 3.54. Gain dispersion for dielectric and metasurface lens integrated Vivaldi antennas

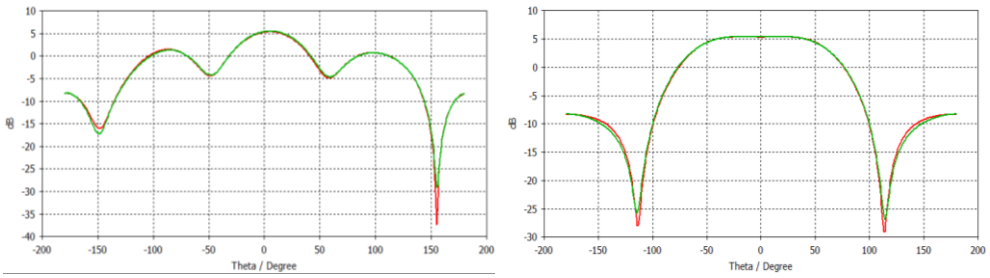

Figure 3.55. Far-field radiation patterns for dielectric and metasurface lens integrated Vivaldi antennas in azimuth (left) and elevation (right) planes at 1 GHz, red and green lines indicate dielectric and metasurface lens integrated antenna patterns, respectively.

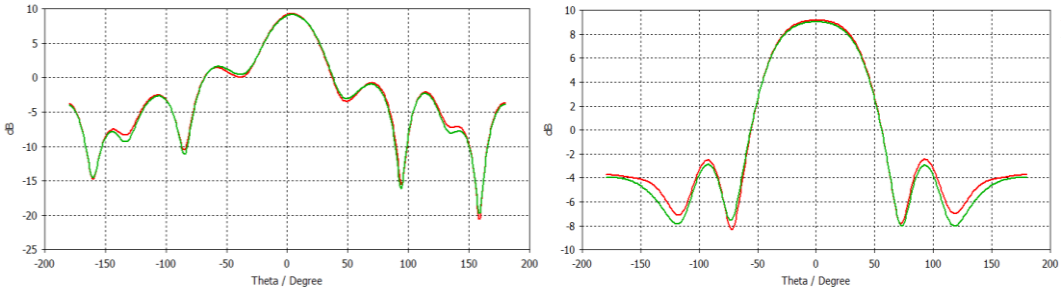

Figure 3.56. Far-field radiation patterns for dielectric and metasurface lens integrated Vivaldi antennas in azimuth (left) and elevation (right) planes at 2 GHz, red and green lines indicate dielectric and metasurface lens integrated antenna patterns, respectively.

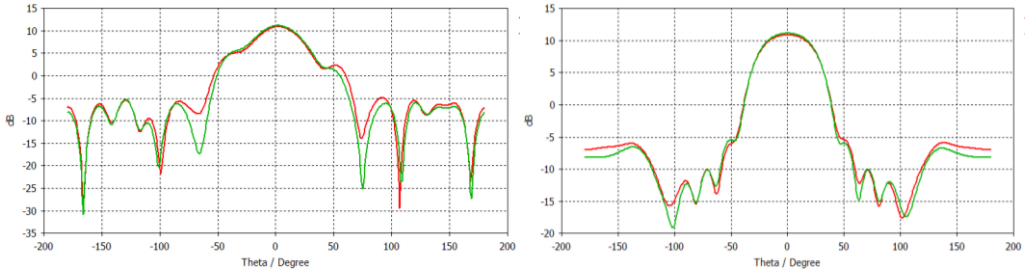

Figure 3.57. Far-field radiation patterns for dielectric and metasurface lens integrated Vivaldi antennas in azimuth (left) and elevation (right) planes at 3 GHz, red and green lines indicate dielectric and metasurface lens integrated antenna patterns, respectively.

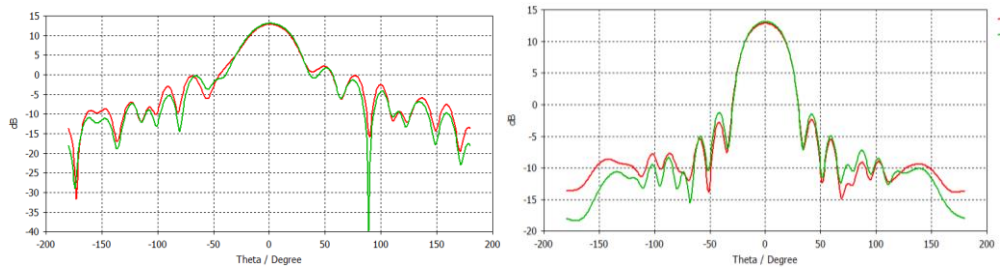

Figure 3.58. Far-field radiation patterns for dielectric and metasurface lens integrated Vivaldi antennas in azimuth (left) and elevation (right) planes at 4 GHz, red and green lines indicate dielectric and metasurface lens integrated antenna patterns, respectively.

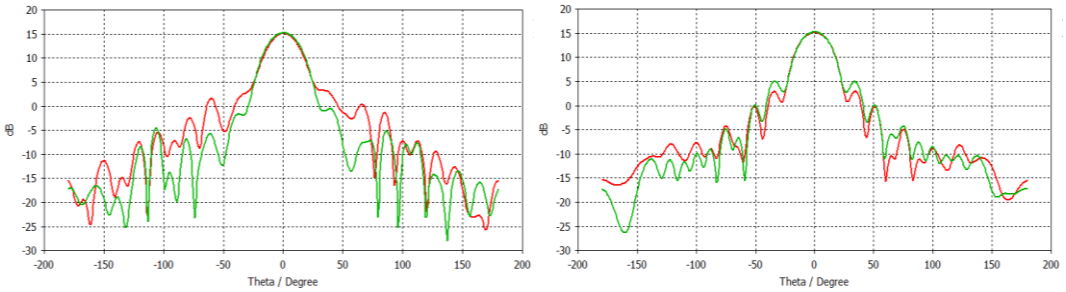

Figure 3.59. Far-field radiation patterns for dielectric and metasurface lens integrated Vivaldi antennas in azimuth (left) and elevation (right) planes at 5 GHz, red and green lines indicate dielectric and metasurface lens integrated antenna patterns, respectively.

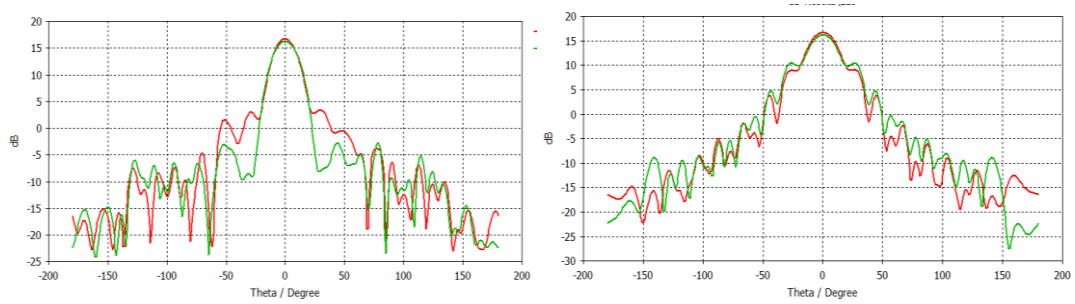

Figure 3.60. Far-field radiation patterns for dielectric and metasurface lens integrated Vivaldi antennas in azimuth (left) and elevation (right) planes at 6 GHz, red and green lines indicate dielectric and metasurface lens integrated antenna patterns, respectively.

S-parameters and efficiency characteristics for both antennas are fairly close in the operation bandwidth. Gain dispersion of the antennas are exceptionally close as illustrated in Figure. 3.54. Radiation patterns in E and H-planes are nearly the same as depicted in Figure.3.55-60. Small discrepancies in the results stem from the marginal differences in EM properties of the dielectric and metasurface lens. These results verify that metasurface lens interacts with antenna near-field in the same

manner with a dielectric lens where relatively higher refractive index material collimates the incident field due to Snell's law of refraction.

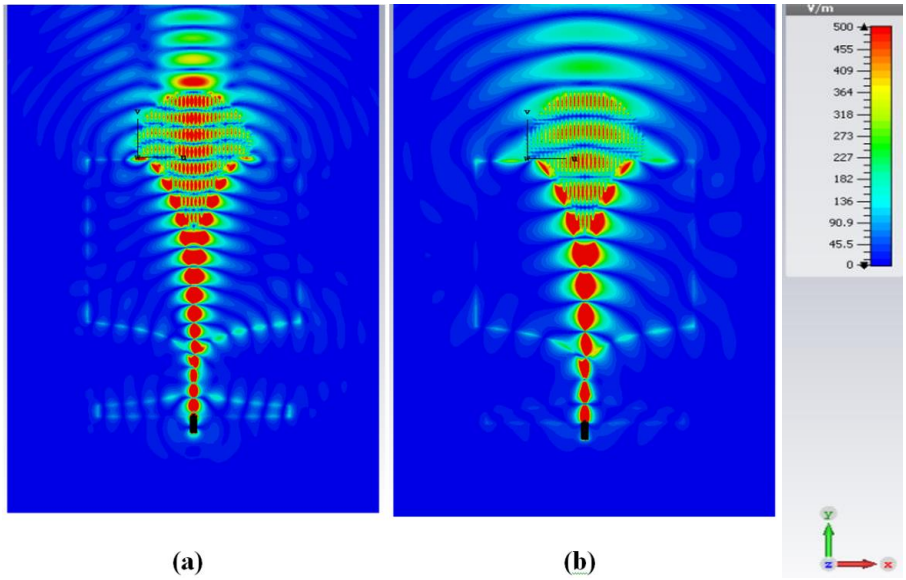

Figure 3.61. Electric field distributions of the antenna with larger lens at different frequencies, top view, (a) at 8 GHz, (b) at 5 GHz

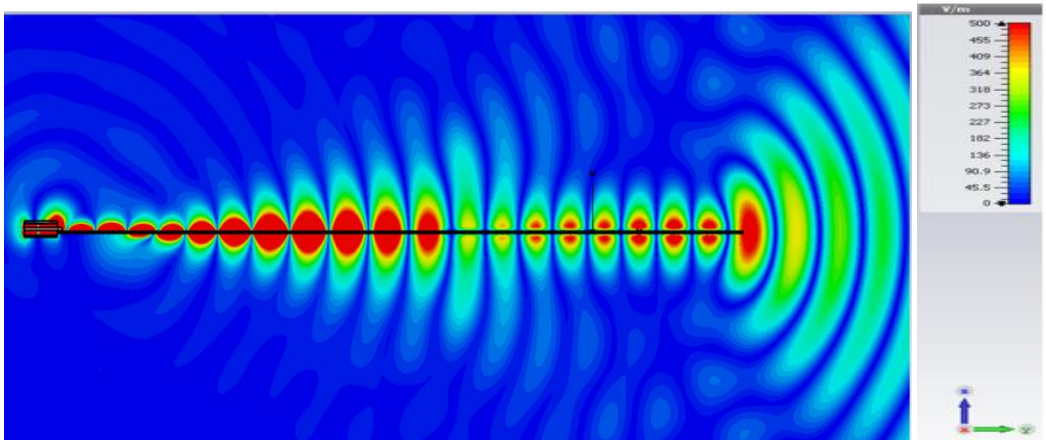

(a)

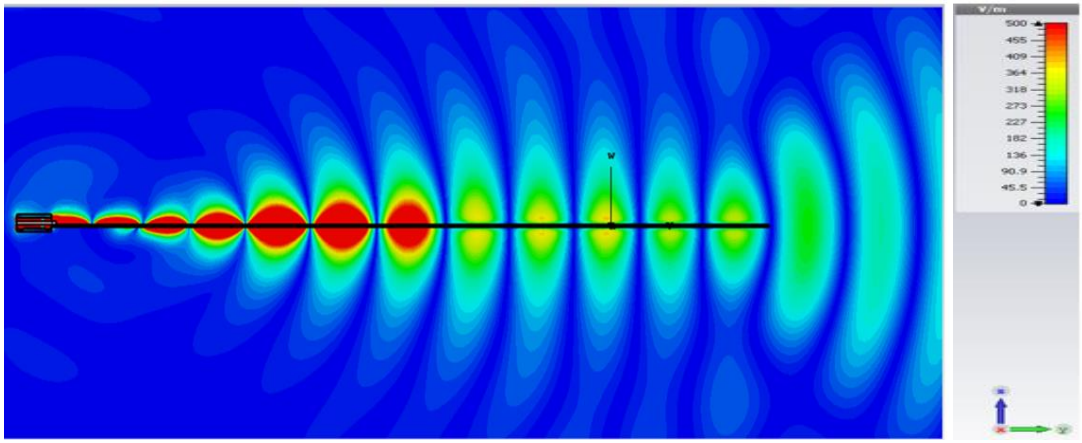

(b)

Figure 3.62. Electric field distributions of the antenna with larger lens at different frequencies, side view, (a) at 8 GHz, (b) at 5 GHz

Electric field distributions in two different planes are given in Figure 3.61 and Figure 3.62 for the antenna with a larger lens. In Figure 3.61(b), in the E-plane, field propagates along the metasurface without any separation in the wavefront at 5 GHz. Conversely, there is a split in the wavefront at 8 GHz in the same plane as shown in Figure 3.61(a). The same issue takes place in the other plane (side view) as well with increased severity in the manner of division as shown in Figure 3.62. This result stems from the identical physical mechanism explained above when comparing metasurfaces with different sizes. In this instance, instead of the position and size of the metasurface, spatial dispersion is at play. Strong spatial dispersion effects the phase velocity of the wave dissimilarly for different points in the space. Analysis of the unit cells for all three specimens shows a steady increase in the refractive index with the frequency. Therefore, fields near the metasurface experience more forceful retardation compared to the fields at the outer edges. In the extreme cases, fields in the outer edges detach from the wavefront and separate into multiple different waves. Far-field patterns at these frequencies display this effect quite clearly.

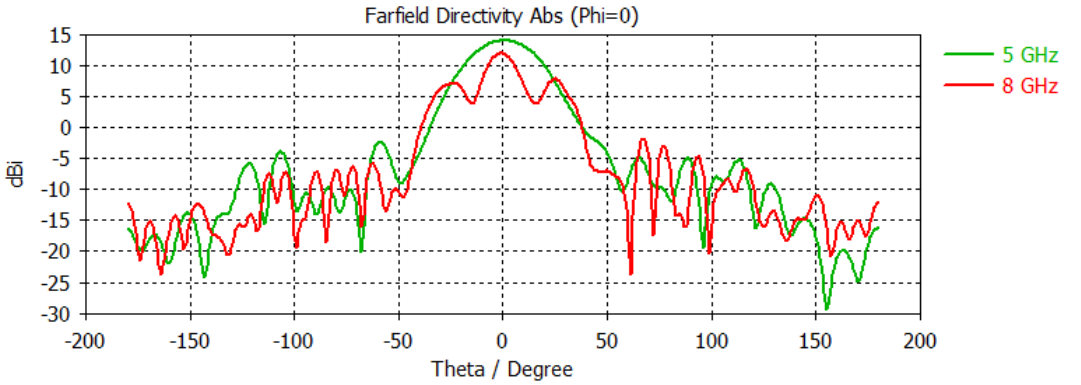

Figure 3.63. Far-field pattern azimuth cuts (E-plane) for the antenna with larger metasurface lens at 5 and 8 GHz

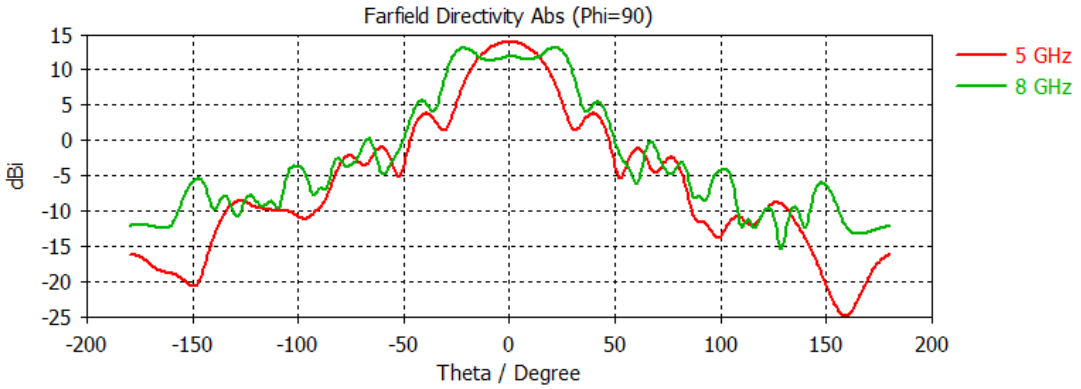

Figure 3.64. Far-field pattern elevation cuts (H-plane) for the antenna with larger metasurface lens at 5 and 8 GHz

In Figure 3.63-64, the beam split is present for both planes (azimuth and elevation) at 8 GHz in contrast with radiation pattern at 5 GHz where the beam is intact. This kind of split in the beam can be detrimental to the microwave imaging process which cannot be tolerated by the prerequisites of this work. Thus, a trade-off reveals itself as the result of this analysis. Metasurfaces constituted by unit cells with the higher refractive index can confine more EM field to the proximity of the antenna and result in more directive patterns at the expense of the operation bandwidth due to occurrence of beam splits at higher frequencies. In conclusion, metasurface must be designed giving the optimum operation bandwidth with the best radiation performance.

3.7. Effects of Unit Cell Topology on Metasurface Lens

Three different unit cell topologies analyzed previously in this chapter were integrated to Vivaldi antenna as metasurface lens. Overall metasurface geometry and size is identical for each unit cell structure. In this section, broadband orientation is chosen as the cell placement method in which 3 parallel strips of the unit cells are parallel to incident electric field.

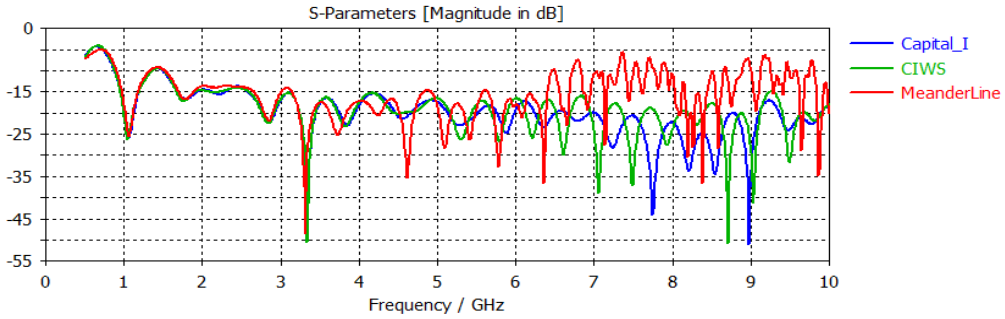

Figure 3.65. Return loss characteristics for metasurface integrated antennas with different unit cells

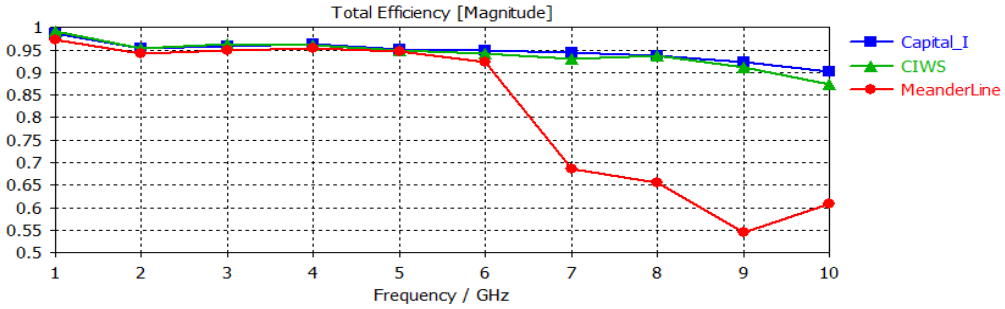

Figure 3.66. Total efficiencies for metasurface integrated antennas with different unit cells

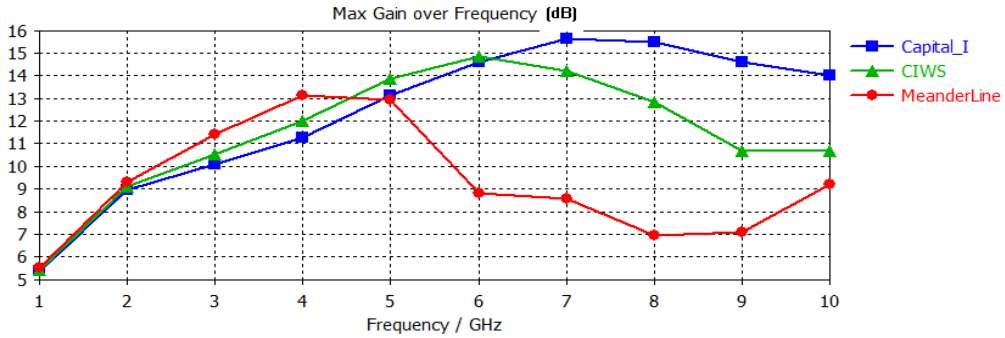

Figure 3.67. Maximum gain over frequency for metasurface integrated antennas with different unit cells

S11 graphs for the antennas are tracking closely up to 6 GHz after which metasurface consisting of meanderline unit cells diverge immensely. At certain frequency bands, a considerable portion of the input energy is reflected by the input port. CIWS and CI unit cell topologies posses a good return loss characteristic in 1-10 GHz bandwidth. This effect is naturally visible in total efficiency plots where ML structure declines with an accelerating rate over the frequency range. Interestingly, return loss characteristics in 7-8 GHz, and 9-10 GHz bandwidths are similar, yet total efficiency is markedly better in the 7-8 GHz bandwidth which means a different physical phenomenon is at play here. ML metasurface has the highest gain up to approximately 4.5 GHz. After this frequency, CIWS structure has the highest gain for nearly another 2 GHz bandwidth. All three structures experience a decline in the gain after certain frequency points. Far-field patterns of the antennas seen in Figure 3.68 explain the anomalies in the gain and efficiency graphs. ML structure radiates an erratic beam which transmits power in multiple directions. CIWS and CI metasurfaces have a regular pencil beam pattern. Beam-split begins to develop for CIWS structure. This circumstance is the results of spatial dispersion explained previously. Each unit cell structure possesses different frequency dispersion.

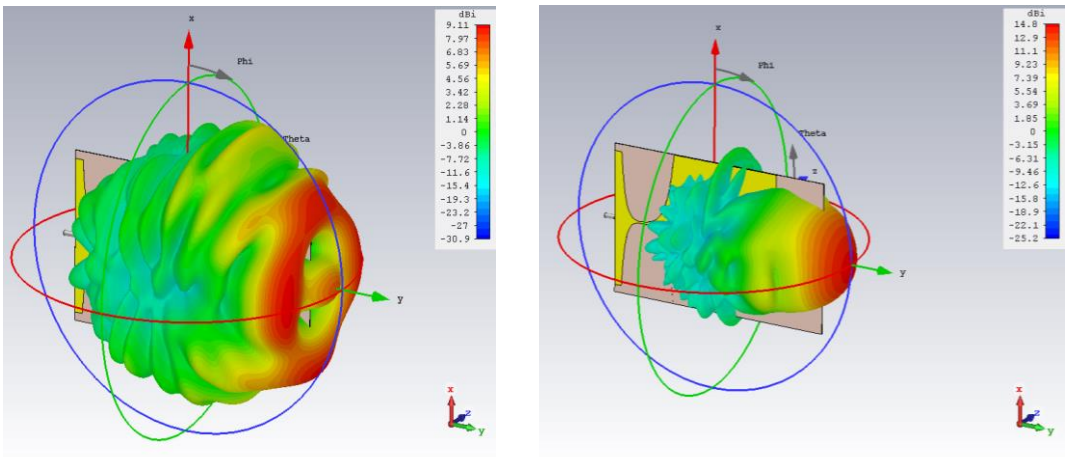

(a) (b)

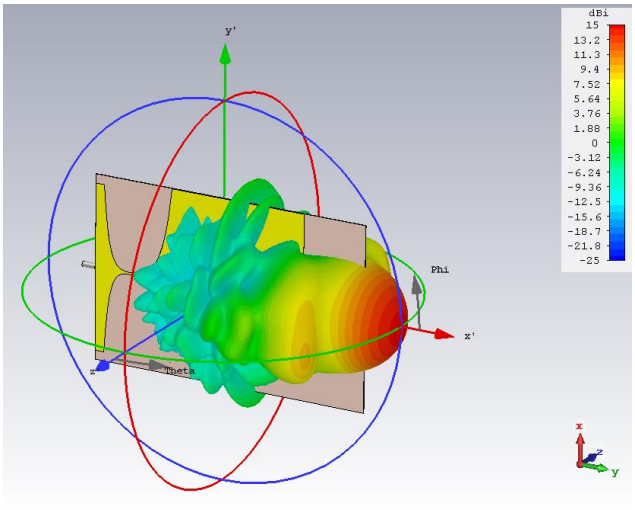

(c)

Figure 3.68. 3-D Far field patterns for metasurface integrated antennas with different unit cell structures at 6 GHz, (a) ML metasurface lens, (b) CI metasurface lens, (c) CIWS metasurface lens

Therefore, separation of the wavefront caused by spatial dispersion takes place at varying frequencies for different unit cell structures. In the ML case, the radiation pattern is deteriorated by the metasurface inside the designated operation bandwidth (1-6 GHz) for the GPR system. Although CI metasurface has a larger bandwidth in terms of increasing gain, the CIWS metasurface antenna is more directive in the operating bandwidth. For the given sizes of the unit cell structures, CIWS topology provides the optimum radiation characteristics in the bandwidth.

3.8. Effects of Unit Cell Orientation on Metasurface Lens

The orientation of the unit cell concerning incident wave polarization and magnetic field direction is an important factor determining the EM properties of the engineered material. Metasurface incorporating CIWS unit cells are tested with the Vivaldi antenna for two different orientations. Since the bulk of the radiated electric field is in –x-direction, the author would address to the orientation of the unit cell where long sides are perpendicular and parallel to the –x-direction as the resonant and broadband orientations, respectively. In the analysis previously made in this chapter, the unit cell in resonant orientation has a larger refractive index compared to

the broadband case. This feature is the determining criterion between the two configurations.

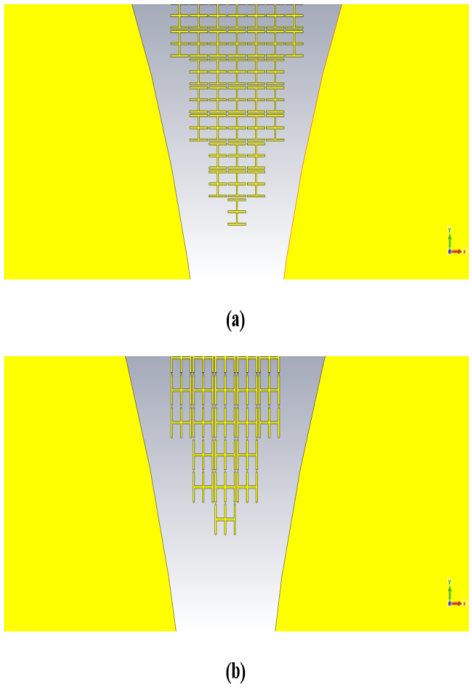

Figure 3.69. Unit cell orientations with respect to Vivaldi antenna, (a) broadband orientation, (b) resonant orientation

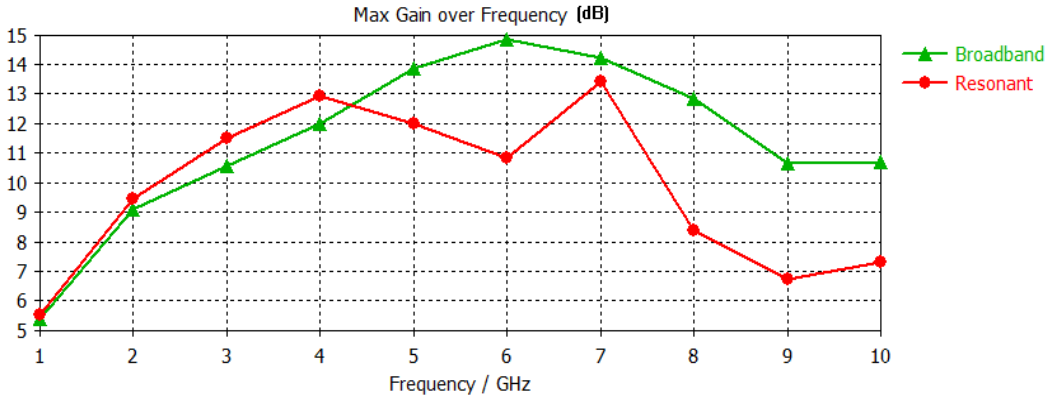

Figure 3.70. Maximum gain over frequency for metasurface antennas with different unit cell orientations

Resonant orientation enhances the directivity of the antenna in the earlier frequency band. Due to the strong spatial dispersion, EM wave traveling along the antenna splits into multiple wavefronts as depicted by Figure 3.72(b) in the operating

bandwidth. As a result, the beam split is present for the far-fields in the bandwidth. For the given sizes of the unit cell, the broadband configuration is a better orientation for the metasurface application of this work due to larger operation bandwidth without beam split.

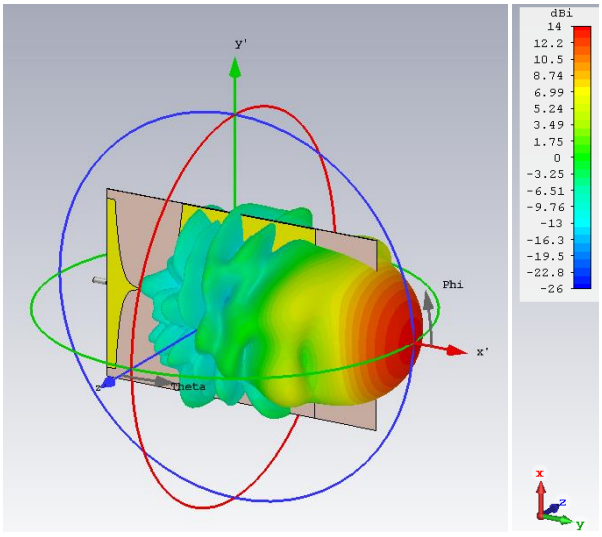

(a)

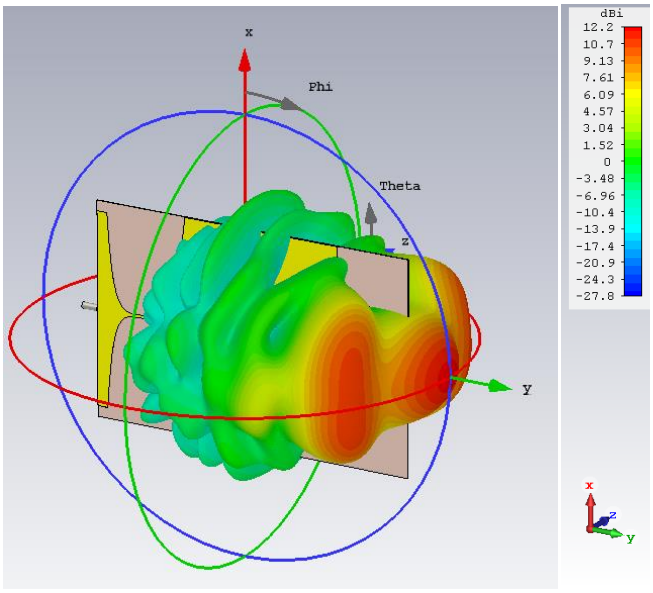

(b)

Figure 3.71. 3-D Far-field patterns for metasurface integrated antennas with different unit cell orientations at 6 GHz, (a) broadband orientation, (b) resonant orientation

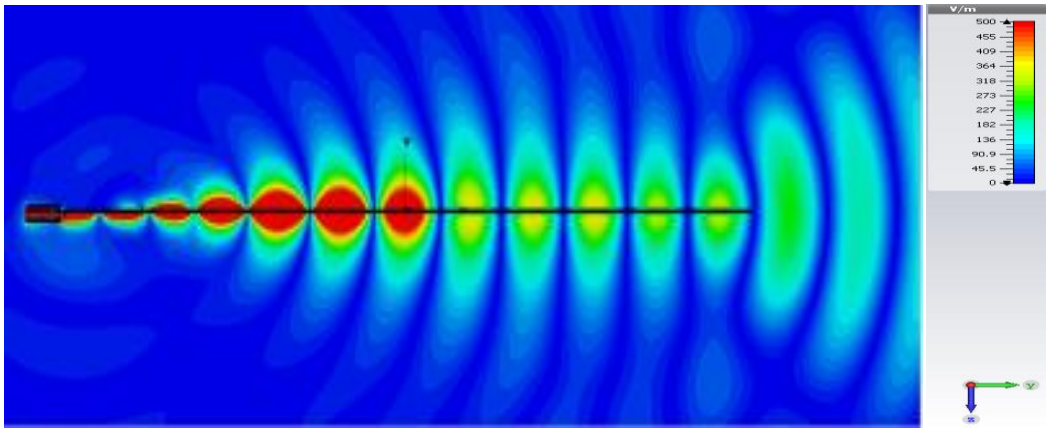

(a)

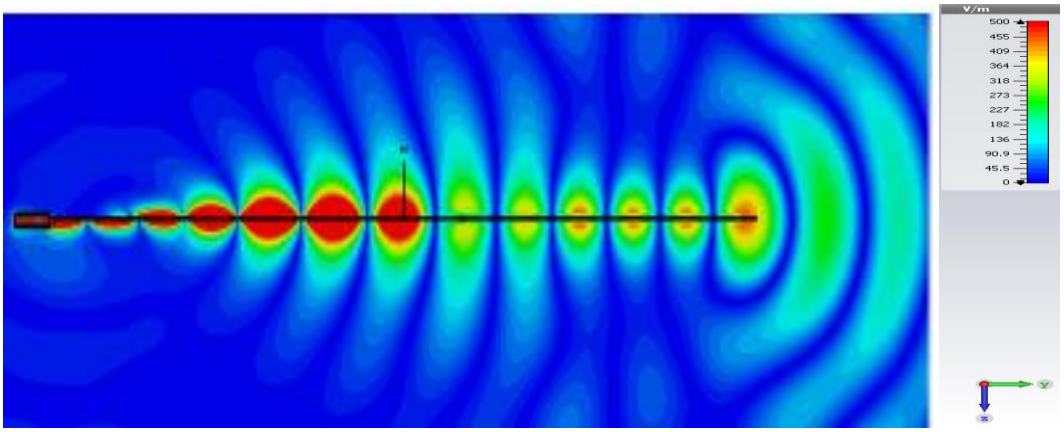

(b)

Figure 3.72. Electric field distributions for metasurface integrated antennas with different unit orientations at 5 GHz, side view, (a) broadband orientation, (b) resonant orientation

3.9. Effects of Metasurface Lens Geometry and Size on Overall Antenna Performance

Besides the features of the unit cell, the physical shape of the metasurface lens structure is another critical factor determining overall radiating system performance. Different geometric patterns and lens sizes are analyzed to obtain the best radiation performance out of the lensing structure. In Figure 3.73, the Vivaldi antenna with different length metasurface lenses is illustrated. Neither the antenna nor the lens

geometry is changed except the lens length in –y-direction. Length of the lens altered without changing the spherical pattern at the end of the lens.

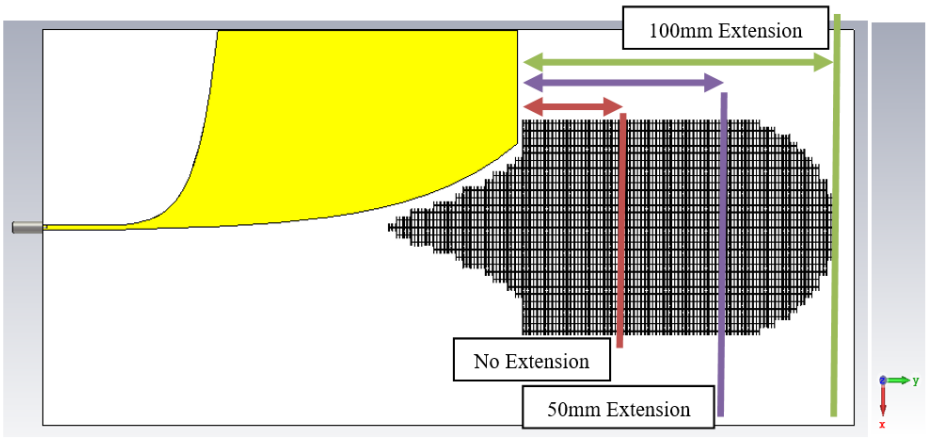

Figure 3.73. Metasurface lenses with different lengths

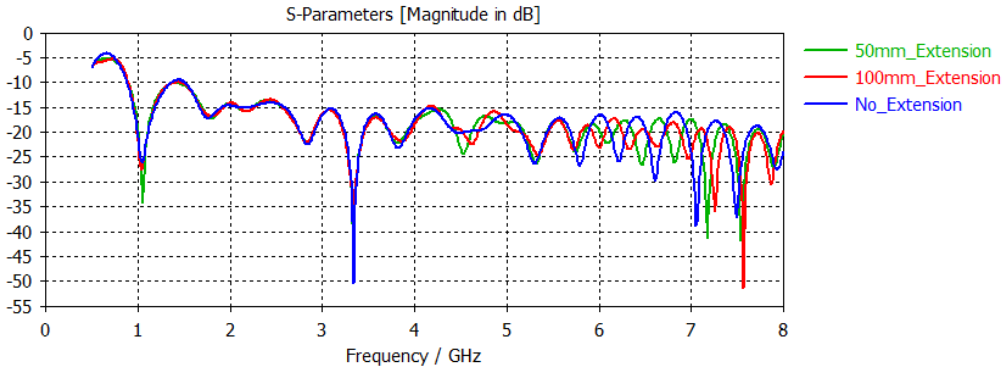

Figure 3.74. Return loss characteristics for metasurface integrated antennas with different metasurface lens lengths

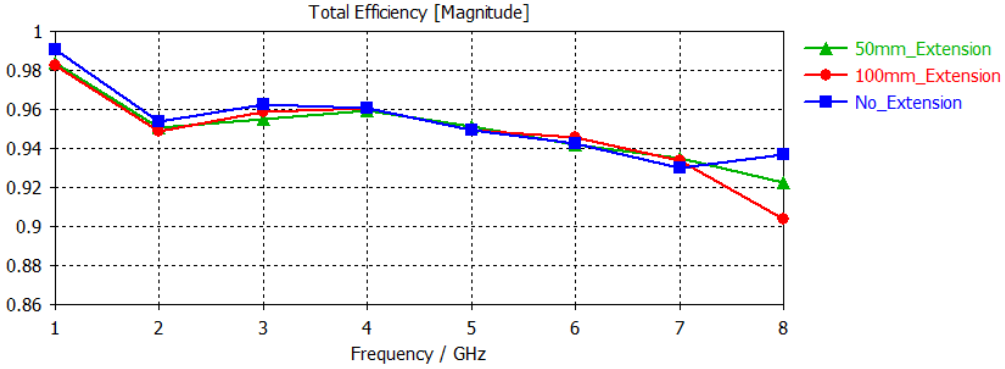

Figure 3.75. Total efficiencies for metasurface integrated antennas with different metasurface lens lengths

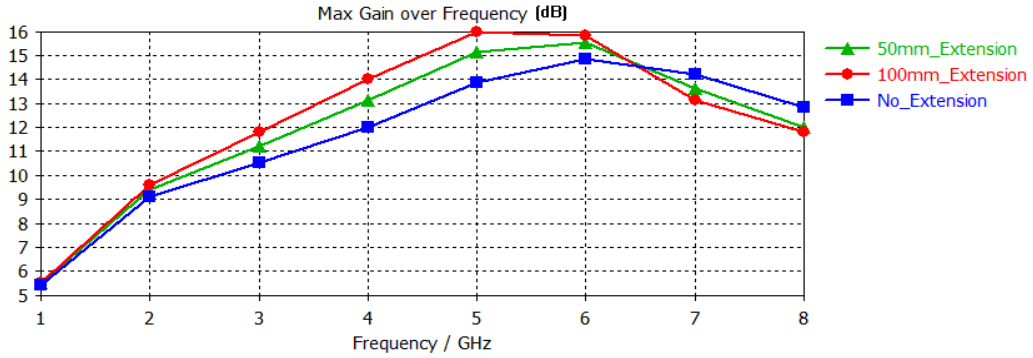

Figure 3.76. Maximum gain over frequency for metasurface antennas with different metasurface lens lengths

All three specimens possess a similar return loss and efficiency characteristics in 1-8 GHz bandwidth. The gain of the antennas increases proportionally with the length of the metasurface up to approximately 6GHz. After this point, the antenna with the shortest lens has a higher gain with a small margin (1dB at 8 GHz). The interesting point is that all three specimens begin to decline in the gain graph at the same frequency (6 GHz). Different behavior in their decline pattern is the rate at which gain deteriorates. Longer the lens, faster the radiation characteristics deterioriates for the antennas. Therefore, it can be concluded that the length of the metasurface lens increases the directivity of the antenna without any cost at other performance characteristics in the operating bandwidth. Sole trade-off present for this parameter is between volume and the gain of the antenna.

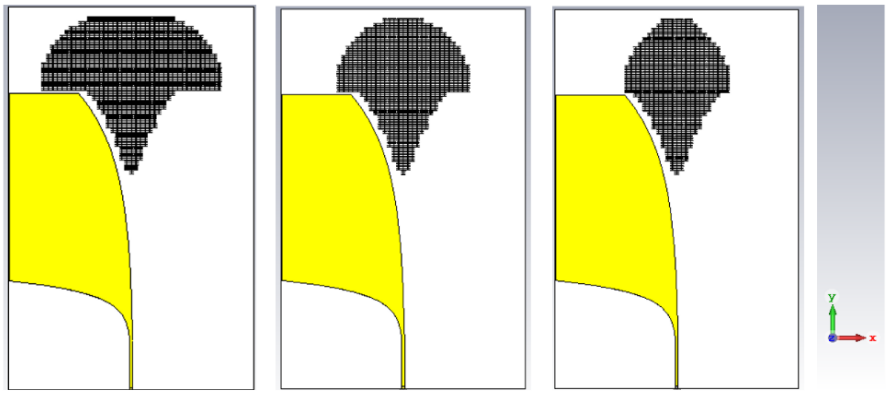

Figure 3.77. Metasurfaces with different widths, (a) 146mm, (b) 108.5mm, (c) 86mm

The same procedure is applied to the width of the metasurface lens. Specimens with identical metasurfaces besides the width of the overall lens are simulated. As shown in Figure 3.80, the width of the lens is altered starting from the upper end of the metallic flares. In all other physical aspects, specimens are identical.

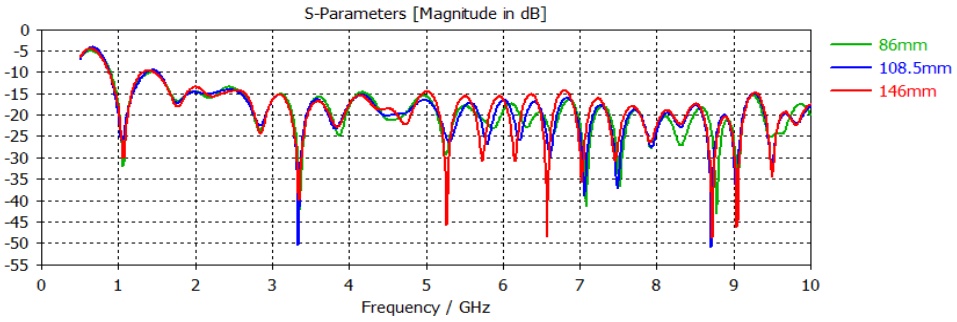

Figure 3.78. Return loss characteristics for metasurface integrated antennas with different lens widths

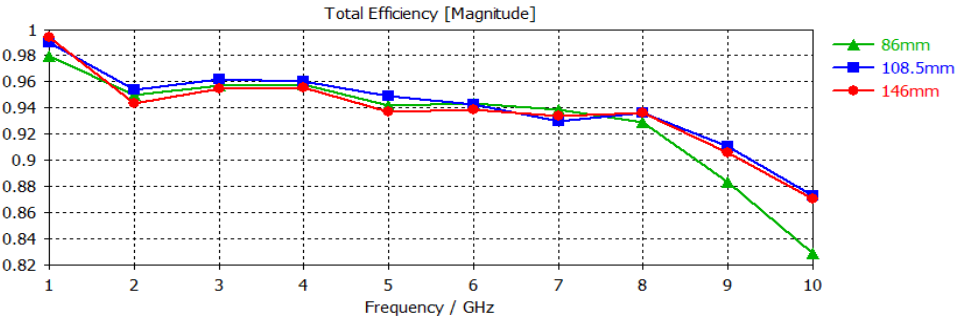

Figure 3.79. Total efficiencies for metasurface integrated antennas with different lens widths

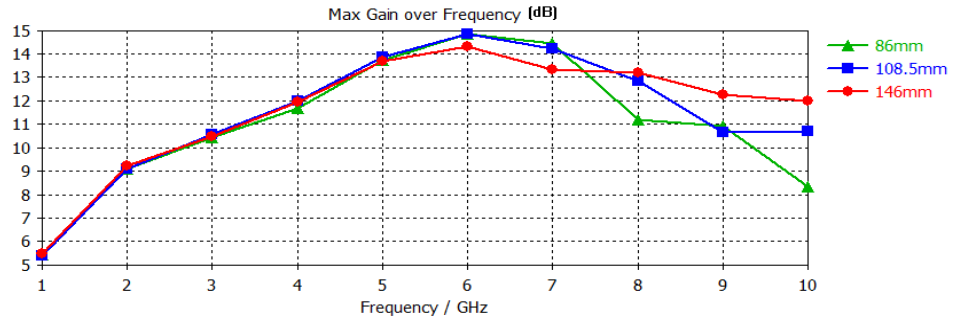

Figure 3.80. Maximum gain over frequency for metasurface integrated antennas with different lens widths

Return loss and total efficiency characteristics for the specimens with three different widths are quite similar in 1-8 GHz. After 8 GHz, the efficiency of the specimen

with the narrow metasurface diverges from the other two antenna systems. Gain plots display a lead for the specimen with 108.5mm width in 3-6GHz bandwidth where the peak is observed at 6 GHz. Although the margin is very narrow (0.5dB), it is worthwhile to optimize the width of the lens to obtain maximum performance enhancement out of the metasurface lens.

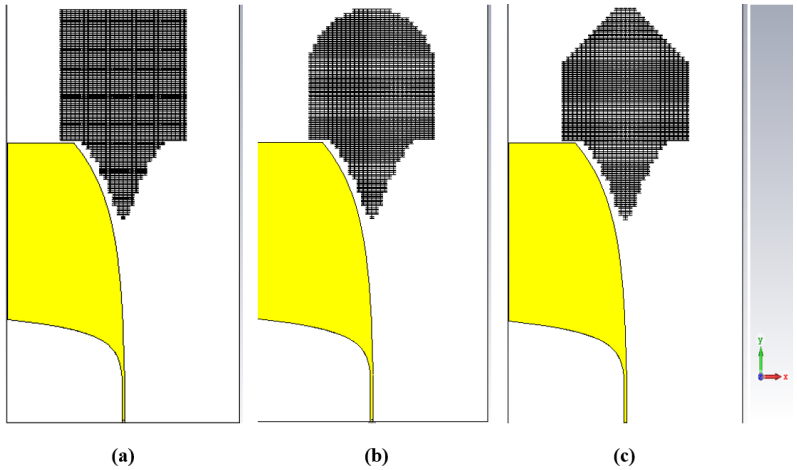

Figure 3.81. Metasurface lenses with different finish patterns, (a) rectangular, (b) hemi-spherical, (c) triangular

Last analysis on the geometry of the overall lens is dedicated to the lens finish pattern. Three different finish patterns are tested and compared. Triangular, rectangular and hemi-spherical finish patterns of the metasurface lens are shown in Figure 3.81.

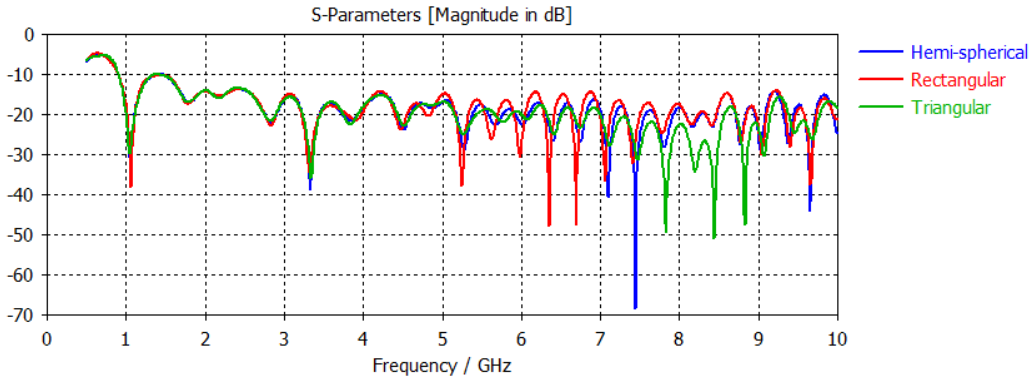

Figure 3.82. Return loss characteristics for metasurface integrated antennas with different lens finish patterns

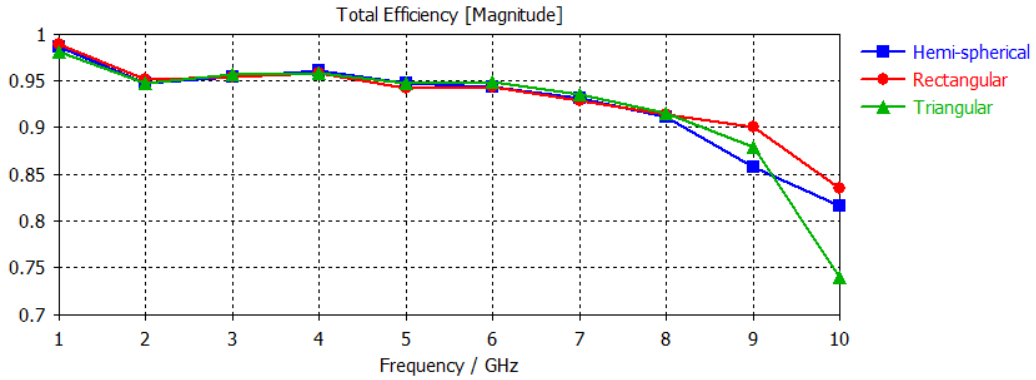

Figure 3.83. Total efficiencies for metasurface integrated antennas with different lens finish patterns

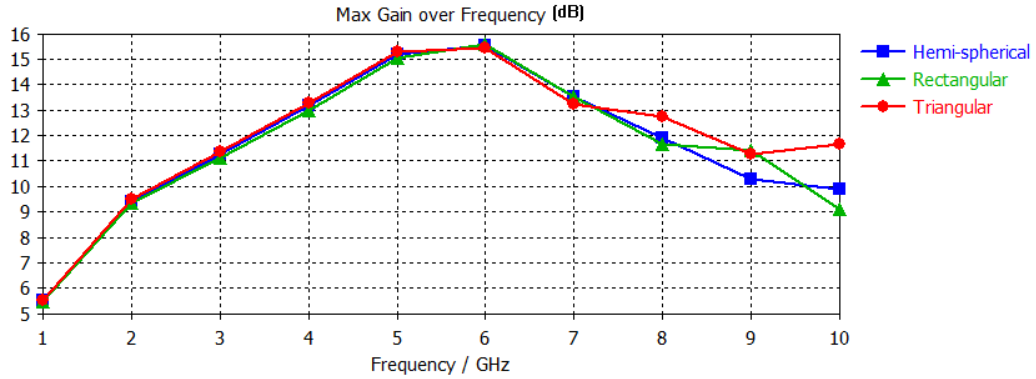

Figure 3.84. Maximum gain over frequency for metasurface integrated antennas with different lens finish patterns

All three finish patterns possess a similar behavior in 1-8GHz bandwidth in terms of total efficiency. Gain plots track together invariably in the same bandwidth only to diverge between 8-10 GHz. In conclusion, the length and width of the metasurface lens are important factors determining radiation characteristics of the overall system whereas finishing pattern is nearly ineffectual.

3.10. Antipodal Vivaldi Antenna with Substrate Integrated Metasurface Lens Design and Simulation Results

The last iteration of the metasurface antenna design is depicted in Fig 3.85. The design procedure is heavily informed by the analysis given throughout this chapter. Unit cell topology, overall lens position, and size, unit cell orientation are carefully

engineered to maximize radiation performance without exacerbating efficiency characteristics.

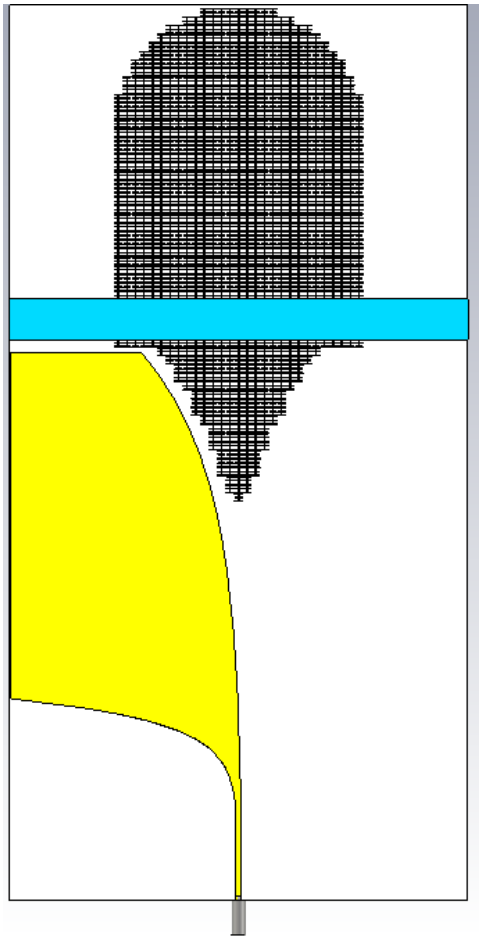

Figure 3.85. Antipodal Vivaldi Antenna with substrate integrated metasurface

The design is also influenced by production capabilities available. In the figure, the blue line represents an adhesive used to glue two separate parts of the antenna. The limitations of the fabrication facilities necessitated this assembly method. Overall, the antenna is fed by the connector at the bottom which excites surface currents on the metallic flares creating a tightly bound EM wave between them. The wave propagates along the metasurface lens and radiates at the physical end of the structure.

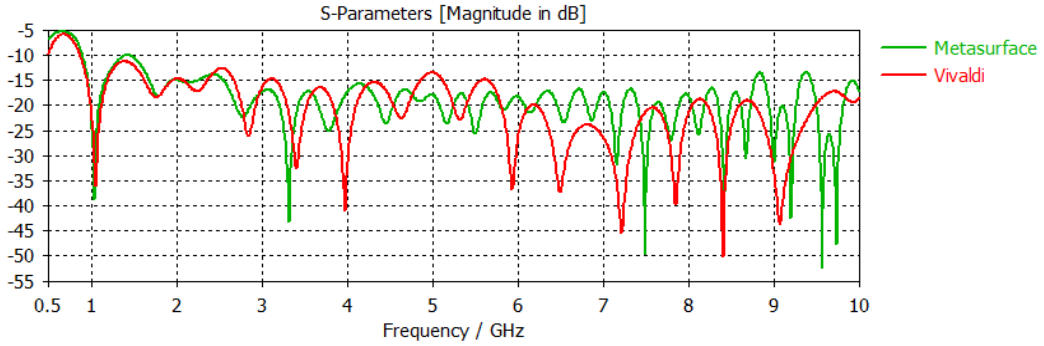

Figure 3.86. Return loss characteristics for metasurface integrated and standard Vivaldi antennas

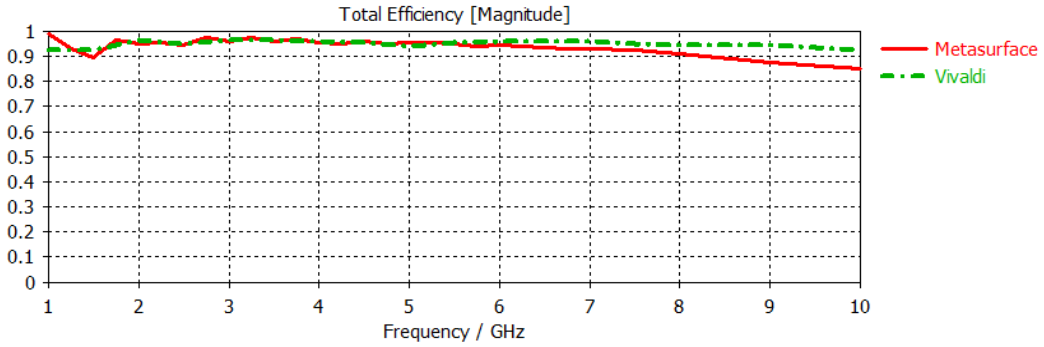

Figure 3.87. Total efficiencies for metasurface integrated and standard Vivaldi antennas

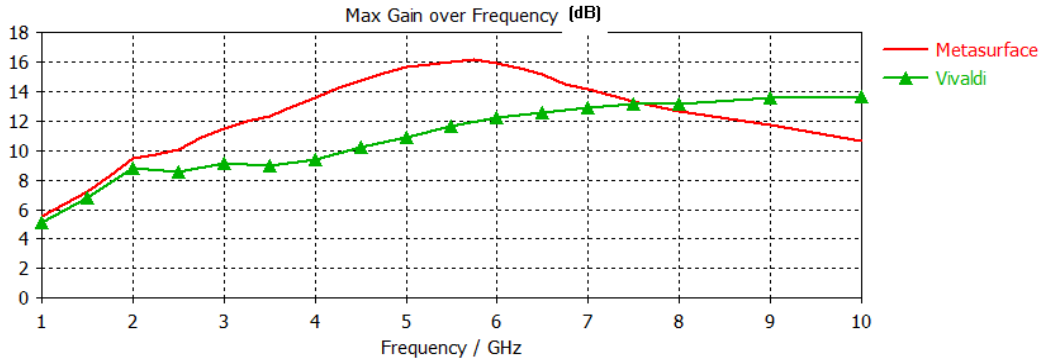

Figure 3.88. Maximum gain over frequency for metasurface integrated and standard Vivaldi antennas

Throughout the operation bandwidth, metasurface and Vivaldi antennas are meeting return loss requirements (S11<-10 dB) and possess similar characteristics. By expectations, return loss for metasurface antenna deteriorates after 6 GHz where metasurface deteriorates antenna performance overall as explained previously in this chapter. The same trend is also valid for efficiency characteristics. Up to 6 GHz,

efficiency levels for both structures are close. After this point, the Vivaldi antenna has better efficiency. Gain dispersion for the antennas indicates a considerable improvement on the part of metasurface. Gain difference peaks approximately around 5 GHz ranging up to 4.8 dB. Gain differential increases proportionally with frequency since incident wave interacts with metasurface more intensely for smaller wavelengths. Naturally, gain enhancement stops at the desired frequency (around 6 GHz) where interaction between incident wave and unit cell causes wavefront to divide into multiple parts due to strong spatial dispersion. After 7.5 GHz, the Vivaldi antenna has higher gain. 3 dB beamwidth for the structure reduces drastically with frequency producing a directive beam compared to original Vivaldi antenna design. Around 6 GHz, sidelobes reach values close to the main beam in elevation direction which indicates that metasurface is at the end of its useful bandwidth. Therefore, we can conclude that the metasurface lens is optimized to maximize radiation performance in the operational bandwidth.

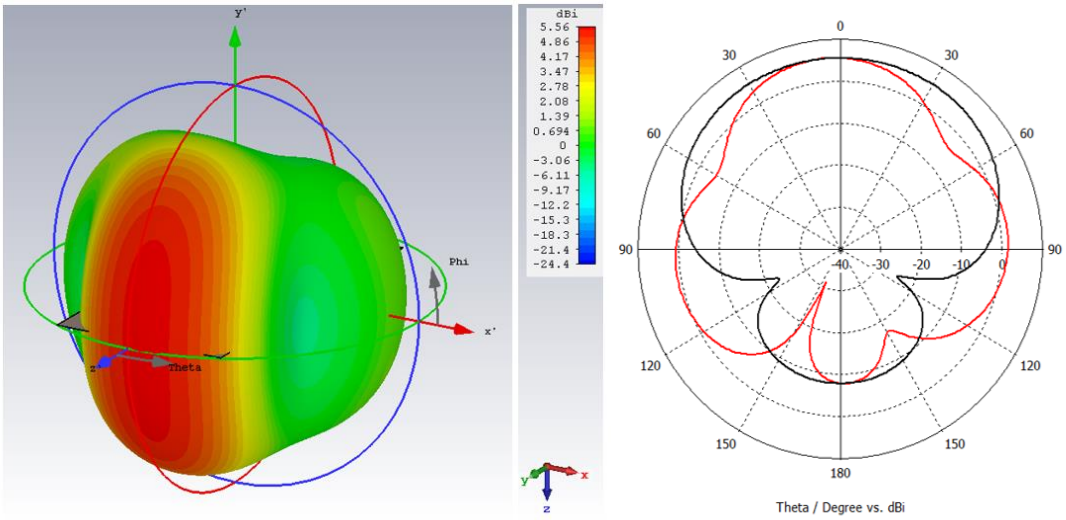

Figure 3.89. 3-D and polar far-field patterns of designed metasurface integrated *Vivaldi* antenna at 1 GHz (red line azimuth cut and black line elevation cut)

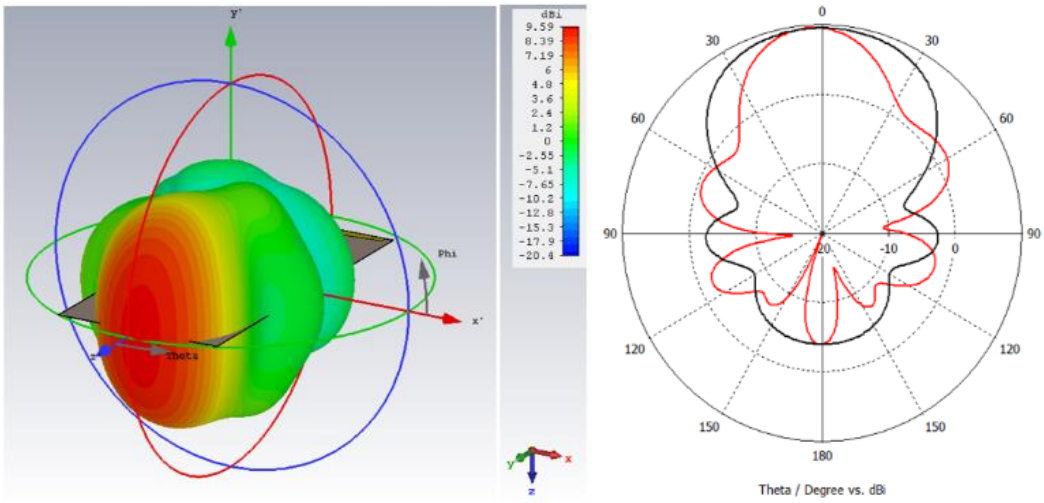

Figure 3.90. 3-D and polar far-field patterns of designed metasurface integrated *Vivaldi* antenna at 2 GHz (red line azimuth cut and black line elevation cut)

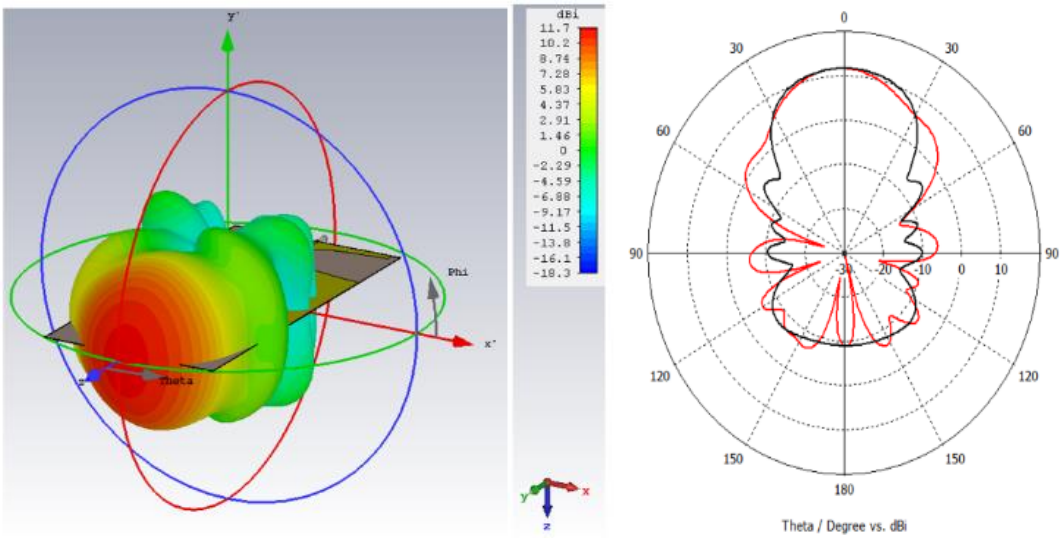

Figure 3.91. 3-D and polar far-field patterns of designed metasurface integrated *Vivaldi* antenna at 3 GHz (red line azimuth cut and black line elevation cut)

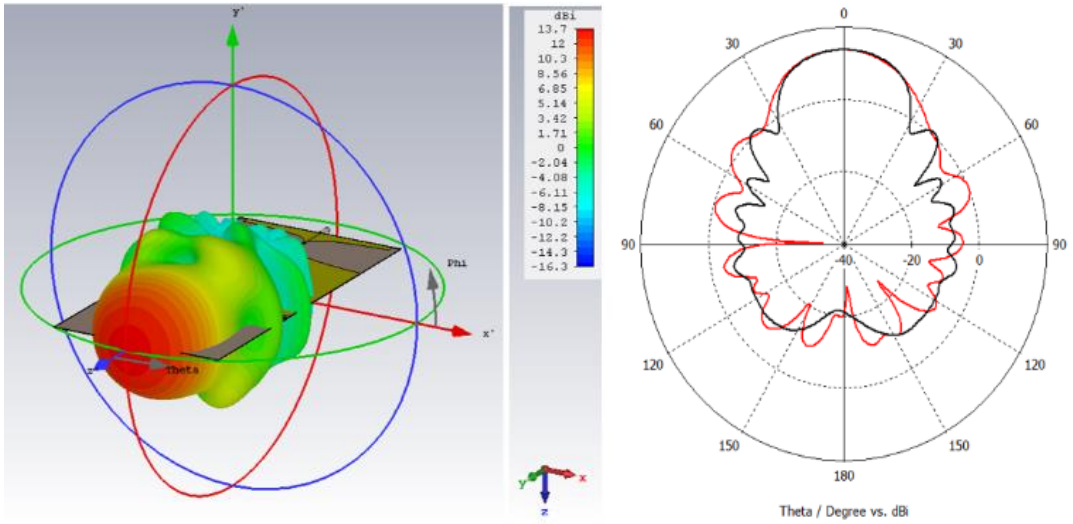

Figure 3.92. 3-D and polar far-field patterns of designed metasurface integrated *Vivaldi* antenna at 4 GHz (red line azimuth cut and black line elevation cut)

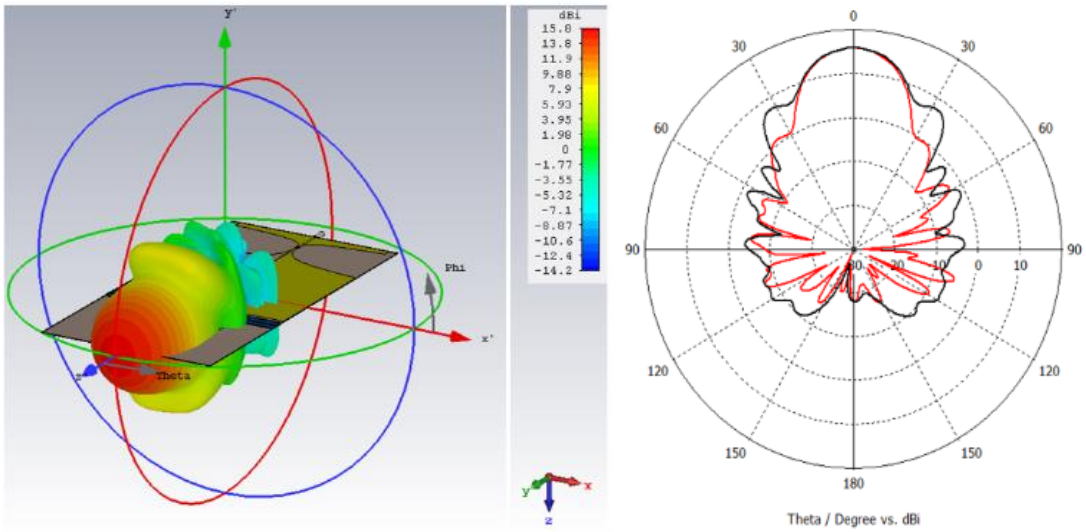

Figure 3.93. 3-D and polar far-field patterns of designed metasurface integrated *Vivaldi* antenna at 5 GHz (red line azimuth cut and black line elevation cut)

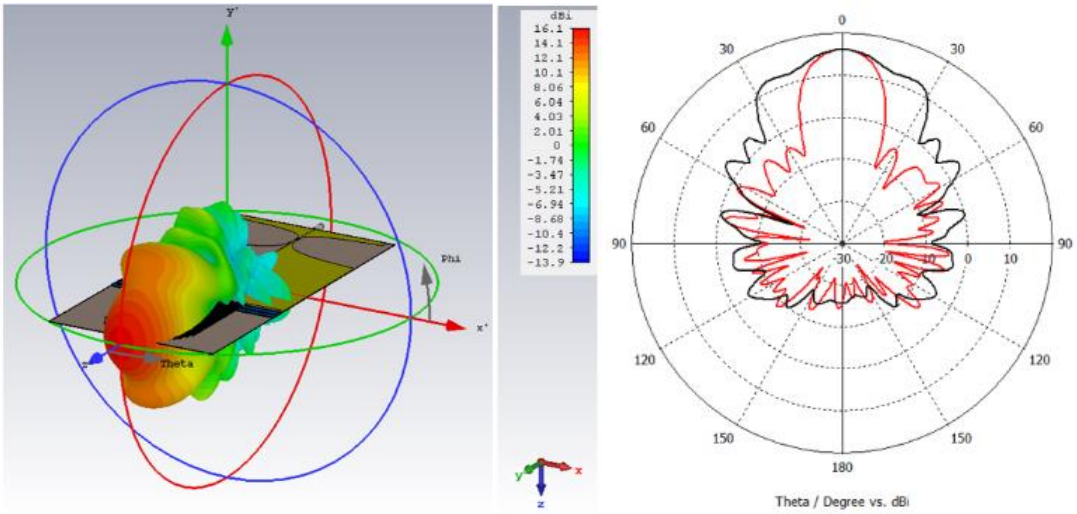

Figure 3.94. 3-D and polar far-field patterns of designed metasurface integrated *Vivaldi* antenna at 6 GHz (red line azimuth cut and black line elevation cut)

Table 3.1. *3-dB beamwidth for metasurface integrated Vivaldi antenna versus frequency*

Frequency (GHz)	**Azimuth 3dB BW (degree)**	**Elevation 3dB BW (degree)**
1	55.8	131
2	39.2	75.1
3	39.8	48.9
4	34.8	34.7
5	25.9	27.4
6	19.3	26.8

CHAPTER 4

FABRICATION AND MEASUREMENT RESULTS

Both antennas are very low profile structures which have 0.8mm length in broadside direction. Fabrication method was to apply laser etching over the dielectric substrate covered with a copper sheet. Dielectric substrate for both antennas is Arlon Iso 917 of Rogers Corporation. The material has $\varepsilon = 2.2$ and $tand = 0.0013$ at 10 GHz. Substrate thickness is 0.762mm (30 mil) and copper thickness is 0.001778mm. Laser etching procedure is carried out with the LPKF ProtoLaser R laser structuring machine with an ultrafast laser source. Metasurface antenna is engraved over two separate substrate sheets due to the limited range of processing for the laser machine. Two disjoint plates are attached to each other via non-conducting glue and cured for 24 hours at room temperature. In the last step, a 50 ohm connector is soldered to the antennas.

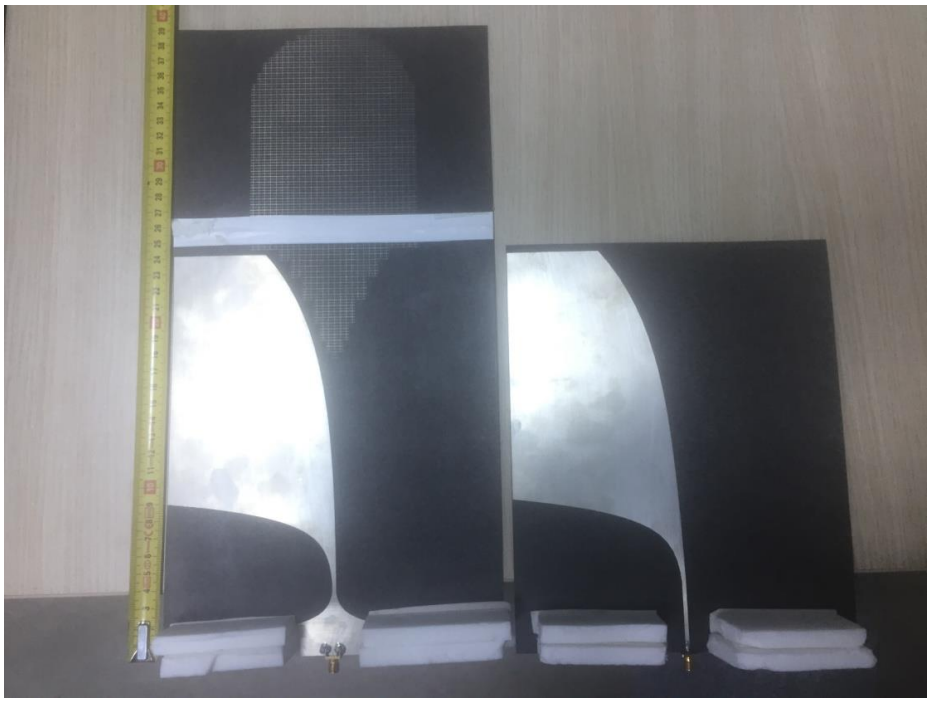

Figure 4.1. Fabricated metasurface integrated and standard Vivaldi antennas

Measurement and simulation results of return loss characteristics for both antennas are given in Figure 4.2. Simulation and measurement results are in good agreement for the entire bandwidth. As depicted in the figure, the metasurface lens has no negative impact in terms of return loss. Both simulation and measurements result display S11 levels lower than -10 dB in the entire bandwidth which was the designated requirement of this work.

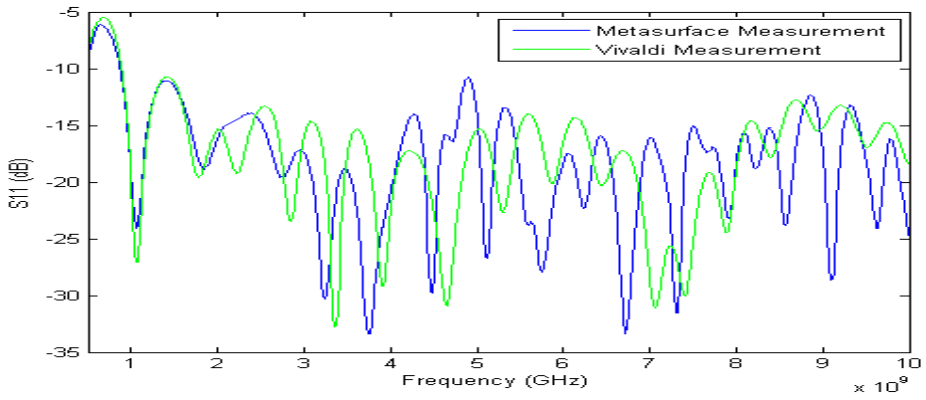

Figure 4.2. Return loss characteristics of fabricated metasurface integrated and standard Vivaldi antennas

Antenna radiation characteristics are measured in near-field measurement anechoic chamber of the company Near-Field System Incorporated. The measurement system utilizes a rollover azimuth scanner scheme which is ideal for characterizing medium and low gain antennas. In this setup, electric field amplitude and phase around the near-field of the antenna under test (AUT) is measured and processed digitally. Later, near-field information is translated into far-field properties of the antenna by near-field/far-field transformation methods. The two-antenna method is used to measure the gain of the antenna. For this method, two measurements are required to obtain gain information of the AUT. Initially, a standard gain antenna with known gain characteristics with the measuring probe is tested. Later, using the same probe, AUT is measured, and gain of the antenna is calculated with the aid of standard gain measurements. The distance between AUT and measuring probe is longer than 3 wavelengths at the lowest frequency of the measurement which ensures correct results by the system capabilities.

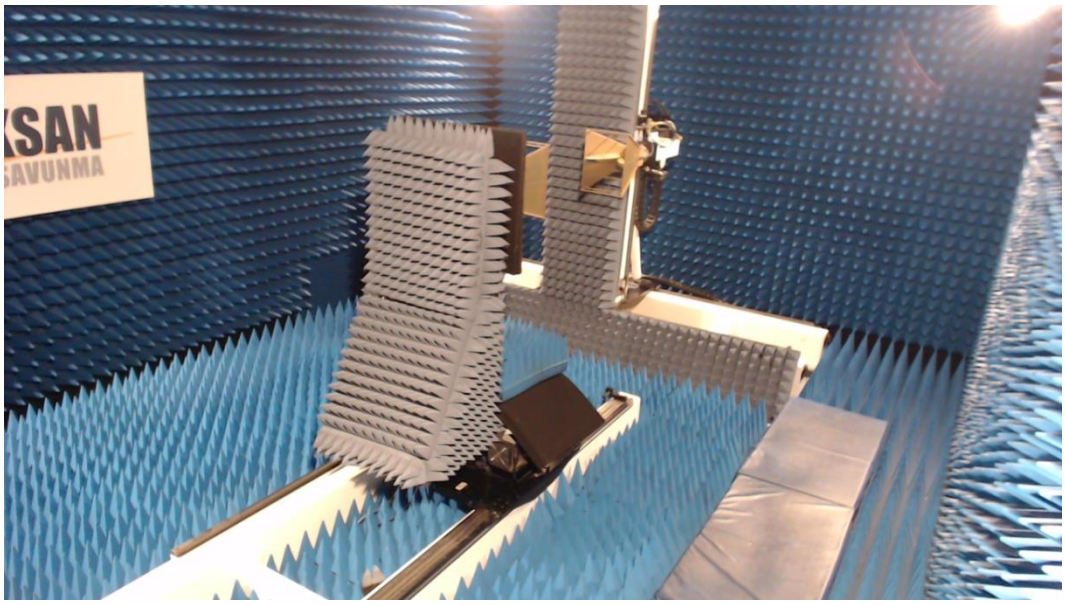

Figure 4.3. Near-field measurement anechoic chamber

In the measurements of this work, a double-ridged horn antenna operating in 0.5-6 GHz bandwidth is utilized as a standard gain antenna. After characterizing the probe antenna, Vivaldi and metasurface antennas are measured in the near-field system as shown in Figure 4.3.

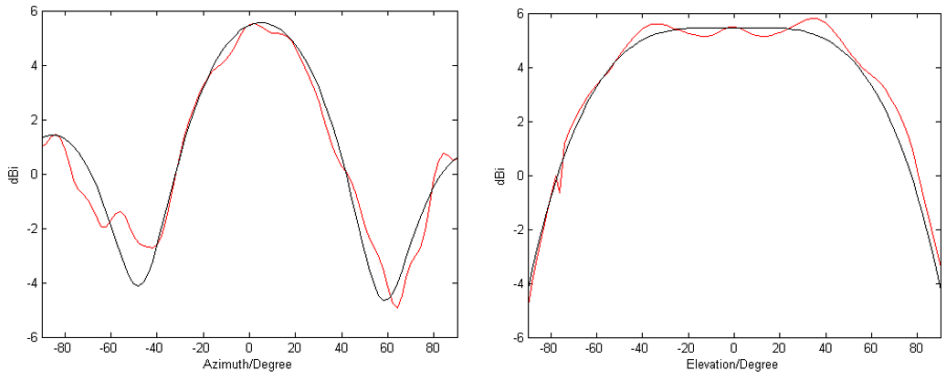

Figure 4.4. Far-field radiation pattern results for metasurface integrated Vivaldi antenna at 1 GHz for, (red line measurement, black line simulation,) for (a) azimuth cut, (b) elevation cut

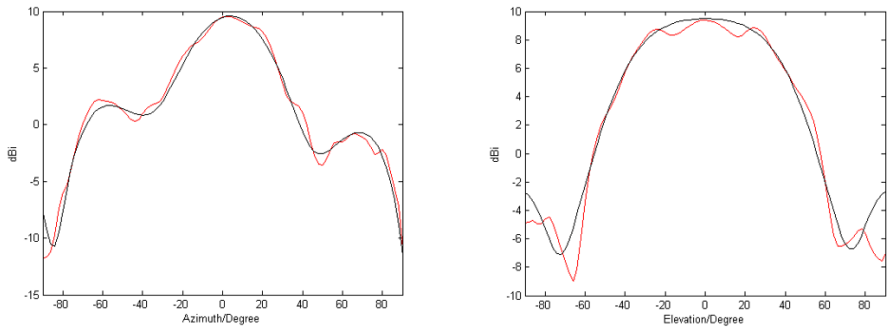

(a) **(b)**

Figure 4.5. Far-field radiation pattern results for metasurface integrated Vivaldi antenna at 2 GHz for, (red line measurement, black line simulation,) for (a) azimuth cut, (b) elevation cut

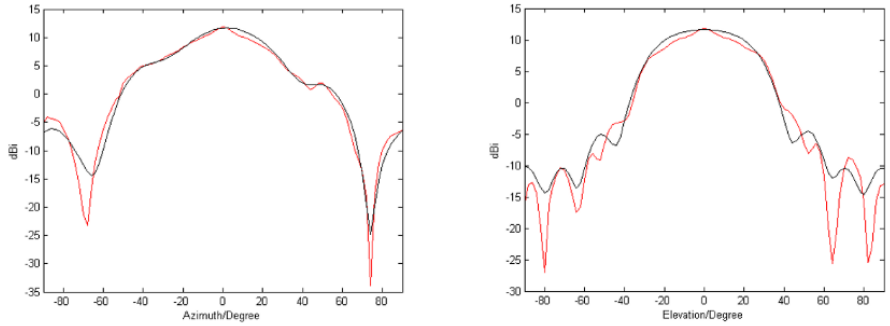

(a) **(b)**

Figure 4.6. Far-field radiation pattern results for metasurface integrated Vivaldi antenna at 3 GHz for, (red line measurement, black line simulation,) for (a) azimuth cut, (b) elevation cut

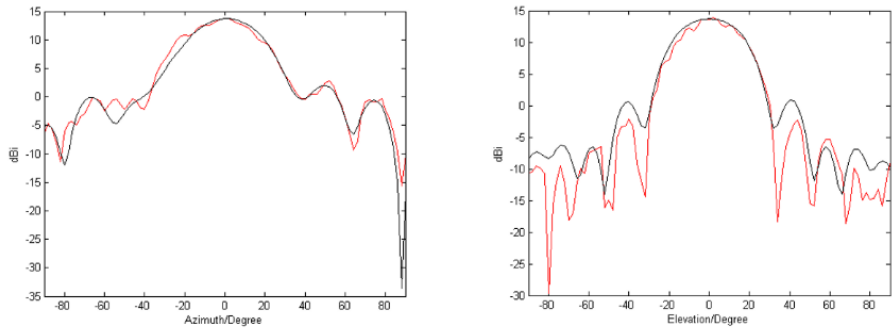

(a) **(b)**

Figure 4.7. Far-field radiation pattern results for metasurface integrated Vivaldi antenna at 4 GHz for, (red line measurement, black line simulation,) for (a) azimuth cut, (b) elevation cut

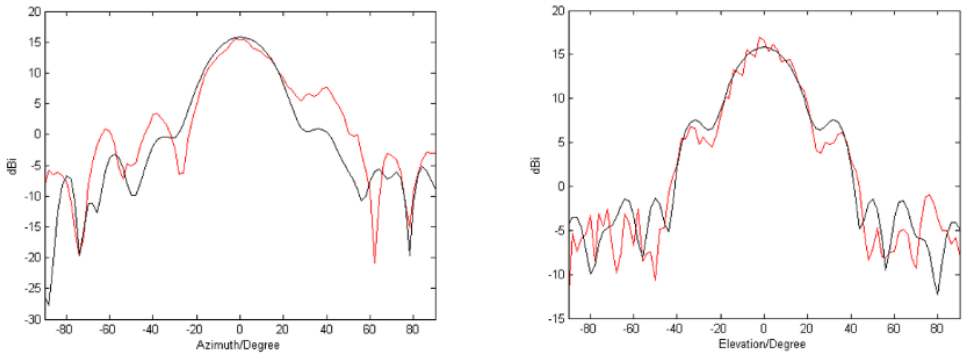

Figure 4.8. Far-field radiation pattern results for metasurface integrated Vivaldi antenna at 5 GHz for, (red line measurement, black line simulation,) for (a) azimuth cut, (b) elevation cut

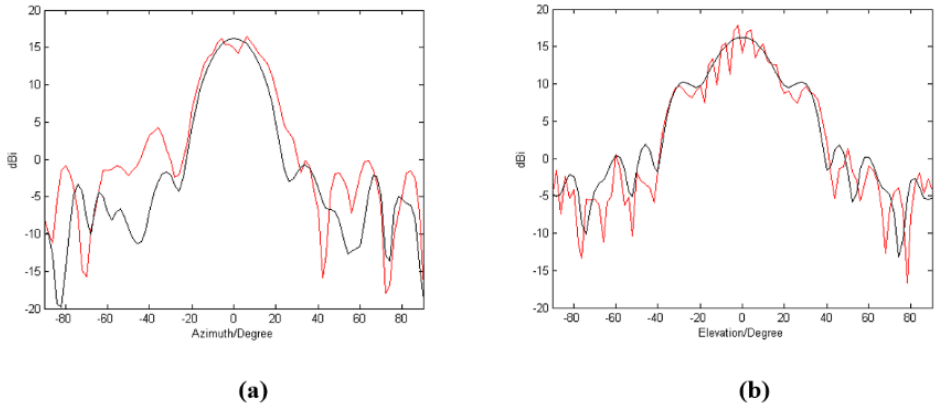

Figure 4.9. Far-field radiation pattern results for metasurface integrated Vivaldi antenna at 5.5 GHz for, (red line measurement, black line simulation,) for (a) azimuth cut, (b) elevation cut

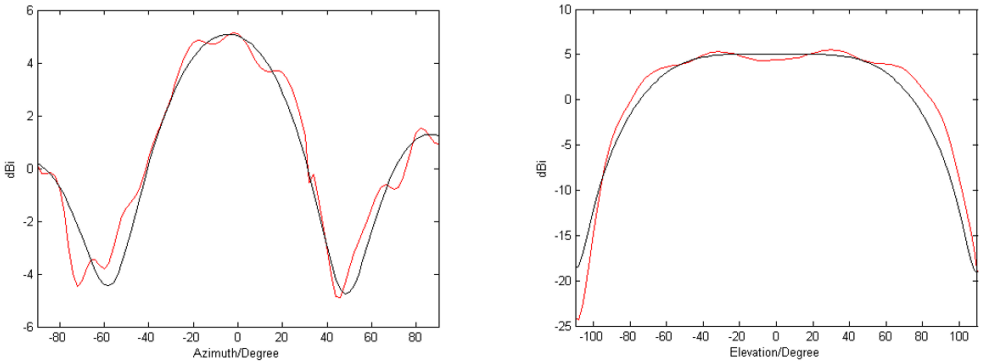

Figure 4.10. Far-field radiation pattern results for standard Vivaldi antenna at 1 GHz for, (red line measurement, black line simulation,) for (a) azimuth cut, (b) elevation cut

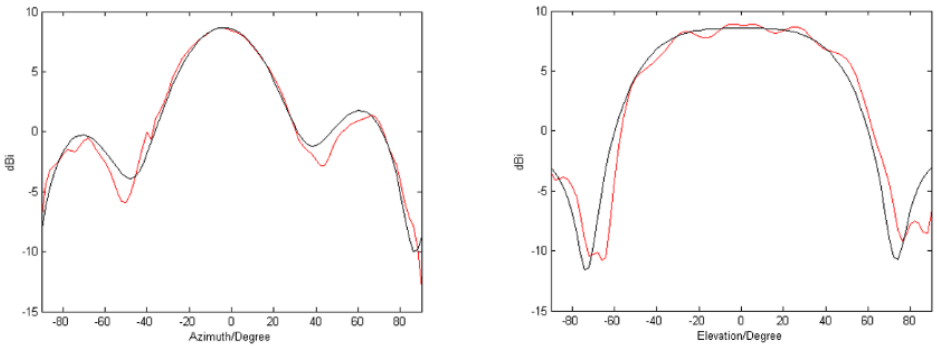

Figure 4.11. Far-field radiation pattern results for standard Vivaldi antenna at 2 GHz for, (red line measurement, black line simulation,) for (a) azimuth cut, (b) elevation cut

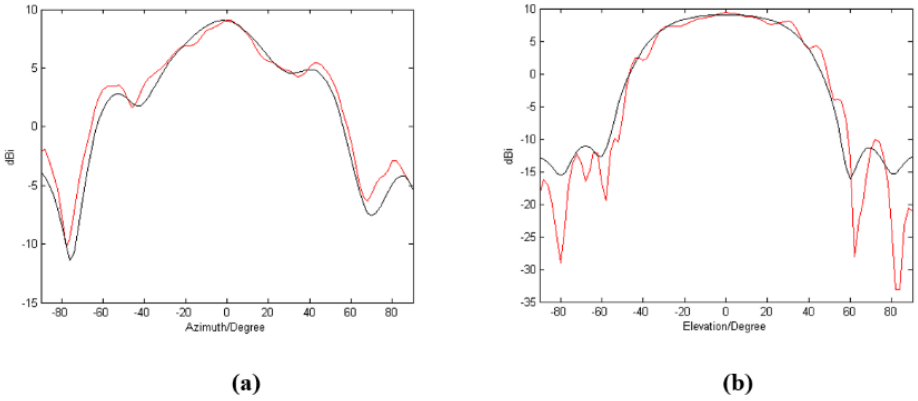

Figure 4.12. Far-field radiation pattern results for standard Vivaldi antenna at 3 GHz for, (red line measurement, black line simulation,) for (a) azimuth cut, (b) elevation cut

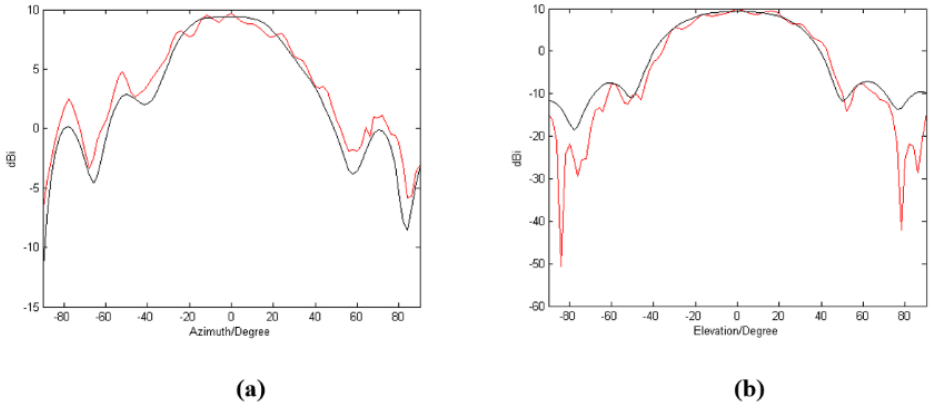

Figure 4.13. Far-field radiation pattern results for standard Vivaldi antenna at 4 GHz for, (red line measurement, black line simulation,) for (a) azimuth cut, (b) elevation cut

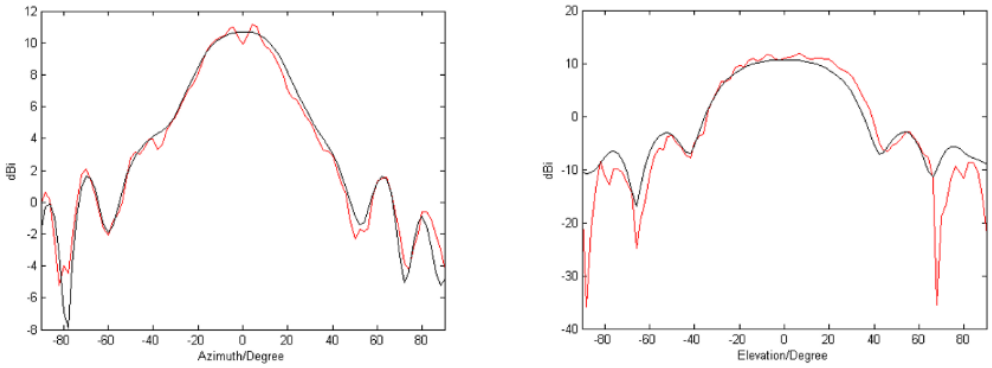

Figure 4.14. Far-field radiation pattern results for standard Vivaldi antenna at 5 GHz for, (red line measurement, black line simulation,) for (a) azimuth cut, (b) elevation cut

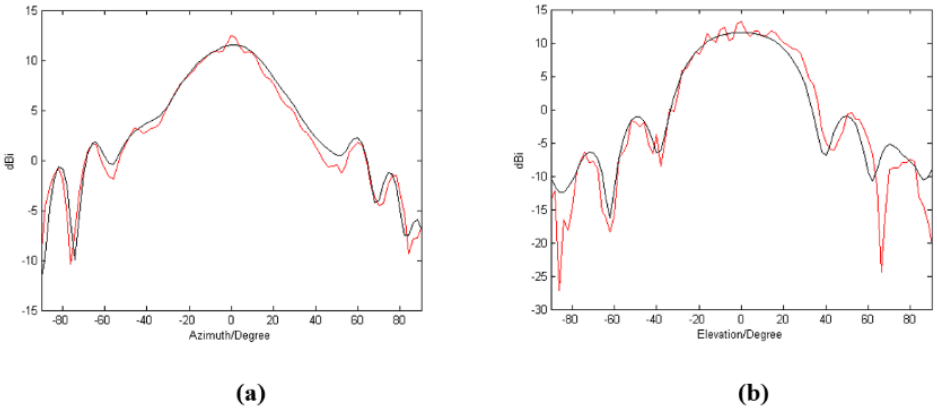

Figure 4.15. Far-field radiation pattern results for standard Vivaldi antenna at 5.5 GHz for, (red line measurement, black line simulation,) for (a) azimuth cut, (b) elevation cut

Radiation patterns obtained from simulations and measurements for both standard Vivaldi antenna and the metasurface loaded Vivaldi antenna are in good agreement as shown in Figure 4.4 through Figure 4.15. Result of experimental radiation pattern display jittery behavior for all frequencies due to oscillations of the antenna during the measurement. In the lower end of the bandwidth, fluctuations in the pattern are less impactful.

On the other hand, higher frequency bandwidth fluctuations increase. The primary reason for this phenomenon is related to measurement setup and physical properties of the antenna. Although precautions are taken, the vibration of the nearly 2-D

structure is an impactful problem. Due to oscillation of the antenna during measurement, amplitude and phase of the received signal vary by the vibrations. Received amplitude levels may not change drastically. However, the phase of the received signal can change more rapidly which will be more influential at shorter wavelengths.

When we compare the results in Figure 4.4 through Figure 4.9 for metasurface loaded Vivaldi antenna with those in Figure 4.10 through Figure 4.15 for standard Vivaldi antenna, we see that the metasurface antenna has a more directive radiation pattern as observed in both simulation and measurement results. HPBW of the metasurface loaded Vivaldi antenna is considerably reduced in the 2-6 GHz bandwidth. Therefore, it is expected to acquire microwave images with better resolution using the metasurface integrated antenna as a sensor compared to the standard Vivaldi antenna.

4.1. Microwave Subsurface Imaging with Substrate Integrated Metasurface Antenna

Subsurface imaging in the microwave band are known to provide feasible solutions to detect obstructed targets such as objects buried under ground or within/behind walls [95, 96]. Use of ultra-wideband sensor system enables us to extract features of the detected target while more directive sources provide better resolution of the received target image. In our experiment, a conducting object is buried into fine soil and a GPR-like system is utilized to extract 2-D microwave image of the target. The experiments are conducted in the "SUBSURFACE TARGET RECOGNITION LABORATORY" in the "Ayaslı Research Center" in the Department of Electrical and Electronics Engineering of METU. Two set of experiments are conducted to compare resolution performance of the metasurface integrated and standard Vivaldi antennas. S11 measurements are recorded in the mechanically scanned sandbox of the laboratory. Measurements are recorded with a

portable Keysight Field Fox N9917A Network Analyzer. Retrieved samples are transmitted to a computer in real time to be stored. Network analyzer is controlled by a 3rd party software called BenchVue of Keysight Technologies via the computer. Power supplied by the network analyzer is 0 dBm (1 mW). Input signal bandwidth is 3-6 GHz. 1001 samples are recorded without averaging over the measurement bandwidth with a frequency step of 3 MHz.

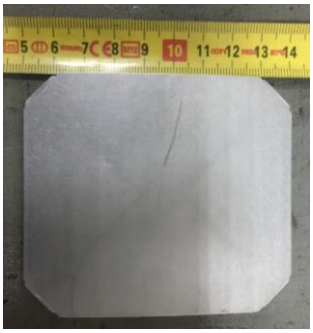

Figure 4.16. Aluminum plate used as target object

In the first experiment, the target is an aluminum plate with dimensions of 8x9cm. There are four identical chamfer features around the edges of the target at the corners which are 1 cm long. Target is buried 2 cm under the ground and antennas are placed 8cm above the air-soil boundary. Distribution of the water content inside soil varies marginally along the measured area. Therefore, soil composition is slightly inhomogeneous. Target is buried inside a square shaped area of size 27x27cm. Measurements are recorded in 3cm spatial steps both in down-track and cross track directions.

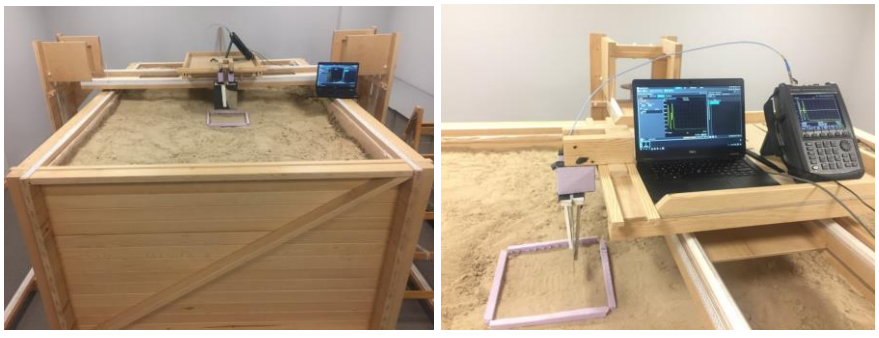

Figure 4.17. Measurement setup for subsurface imaging

The recorded A-scan signals provide useful information in time domain about position of the buried object within soil with respect to air-ground boundary. A-scan signals for three different cases are depicted in Figure. 4.18 and Figure 4.19; for a measurement taken at the center of the target at the point $p_1(7,4)$, another measurement recorded close to the target edge at the point $p_2(7,5.5)$, and finally a measurement taken far away from the target at the point $p_3(4,4)$. These data are retrieved with standard Vivaldi antenna. The coordinates of the points p_1, p_2 and p_3 are defined using the contour plot in Figure 4.21(b) showing the constructed target image. Figure 4.18 shows unprocessed (raw) A-scan signals in these three points where reflections from the antenna and from the air-soil boundary are not removed yet.

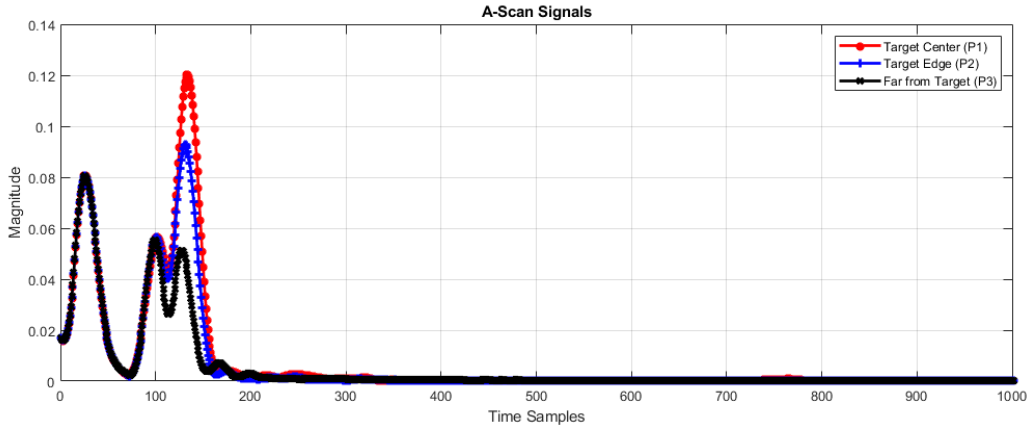

Figure 4.18. A-scan signals for different points

In order to eliminate reflections due to the antenna from the A-scan signals, the preprocessing method introduced in [104] is employed. As seen in Figure 4.18, the reflections coming from the antenna present itself from the beginning up to 78th time sample which are independent from the presence of ground and the target. After removing these antenna reflections from the A-scan curve of Figure 4.18, we obtain the processed A-scan signals of Figure 4.19. The A-scan signals shown in this figure still contains the undesired ground reflections which need to be removed as well. Around the 134th time sample, reflected energy spikes indicating the presence of the

target. We also observe two individual spikes close to each other at point p_3 which is far away from the target. These spikes indicate the refection from the buried object. Since the target is shallowly buried, air-ground reflection and target signals are superposed. Also, some signal coming from the target is still captured by the antenna as the HPBW of the standard Vivaldi antenna is not small enough.

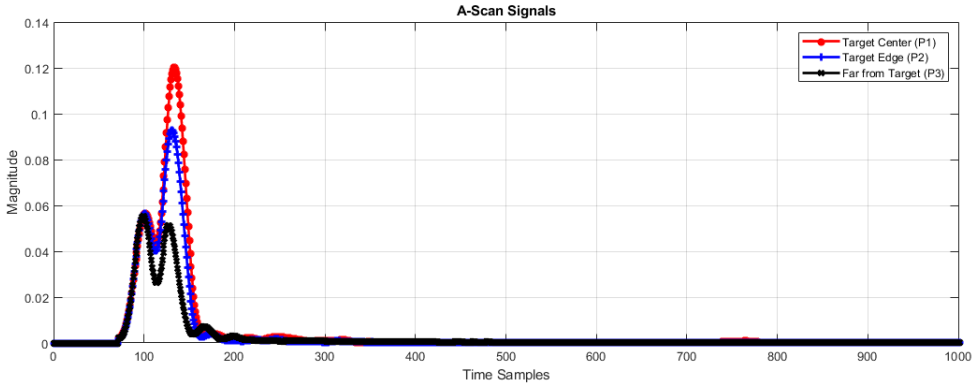

Figure 4.19. A-scan signals for different points without antenna internal reflection

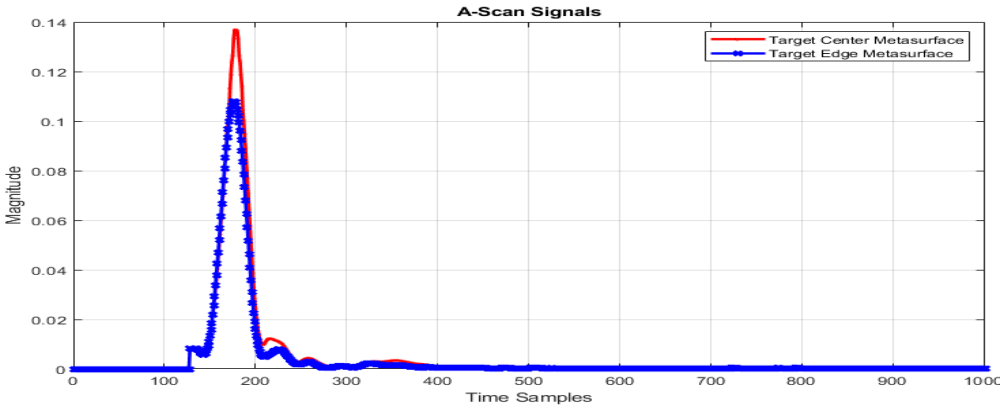

Figure 4.20. A-scan signals measured by metasurface loaded Vivaldi antenna for different points

In Figure 4.20, the A-scan signals measured with metasurface lens integrated antenna are shown at points p_1 and p_2 defined earlier. Maximum reflection is obtained approximately at the 170th time sample which indicates a slight shift in time compared to measurement obtained with the standard Vivaldi antenna. The main reason for this shift is due to the fact that the metasurface lens integrated antenna is longer and has a different phase center location. It can also be seen from the plots

that A-scan signal retrieved by metasurface lens integrated antenna yields a higher maximum power reflected from the target. This results expected as the metasurface integrated Vivaldi antenna has a higher gain as compared to the standard Vivaldi antenna.

Cumulated energy curves and total energy values of A-scan GPR signals are useful quadratic features increasing the contrast between the target signatures and the background effects, in general [97,102]. Total cumulative energy curve $E(t)$ of a given A-scan signal $x(\tau)$ measurement at a given spatial test point is computed as

$$E(t) = \int_0^t |x(\tau)|^2 d\tau \tag{28}$$

as defined originally in [105]. The total energy of the signal is obtained from equation (28) for $t \to \infty$. Prior to the computation of total energy of an A-scan signal, undesired effects such as the initial reflections from the soil-air boundary and the antenna reflections should be eliminated. The antenna effects can be removed as discussed earlier, or both effects can be removed as follows: The A-scan signals are measured at a number of arbitrarily selected points without the buried target. Average of the total energies computed for each reference A-scan data is subtracted from the total energy of the testing A-scan data used in image formation. Then, the 2-D images shown in Figure 4.21 are constructed by contour plotting the calibrated total energy values over the measurement domain that spans an area of 27cm by 27cm. In these measurements, the target is buried 2 cm below the ground surface and the antenna is 8 cm above the surface. Hence, the antenna and the target are separated by 10cm in air-soil composite medium. The black frame in the illustrations show the location and size of the buried object. As illustrated in Figure 4.21, measurements with a metasurface integrated antenna yielded a microwave image with better resolution as compared to the Vivaldi antenna. The edges at the corners of the target are not clear in the image created by the standard Vivaldi antenna measurements whereas these edge effects are more obvious in the image obtained by the metasurface antenna measurements. Overall, the resemblance of the image to the

actual target is improved in the measurements with the metasurface lens integrated antenna. Also, the target image obtained by the standard Vivaldi antenna is considerably larger having the size of 9.5x12cm as compared to the actual size of the target which is 8x9cm. On the other hand, the target image is nearly the same size as the actual target based on the metasurface lens integrated antenna measurements.

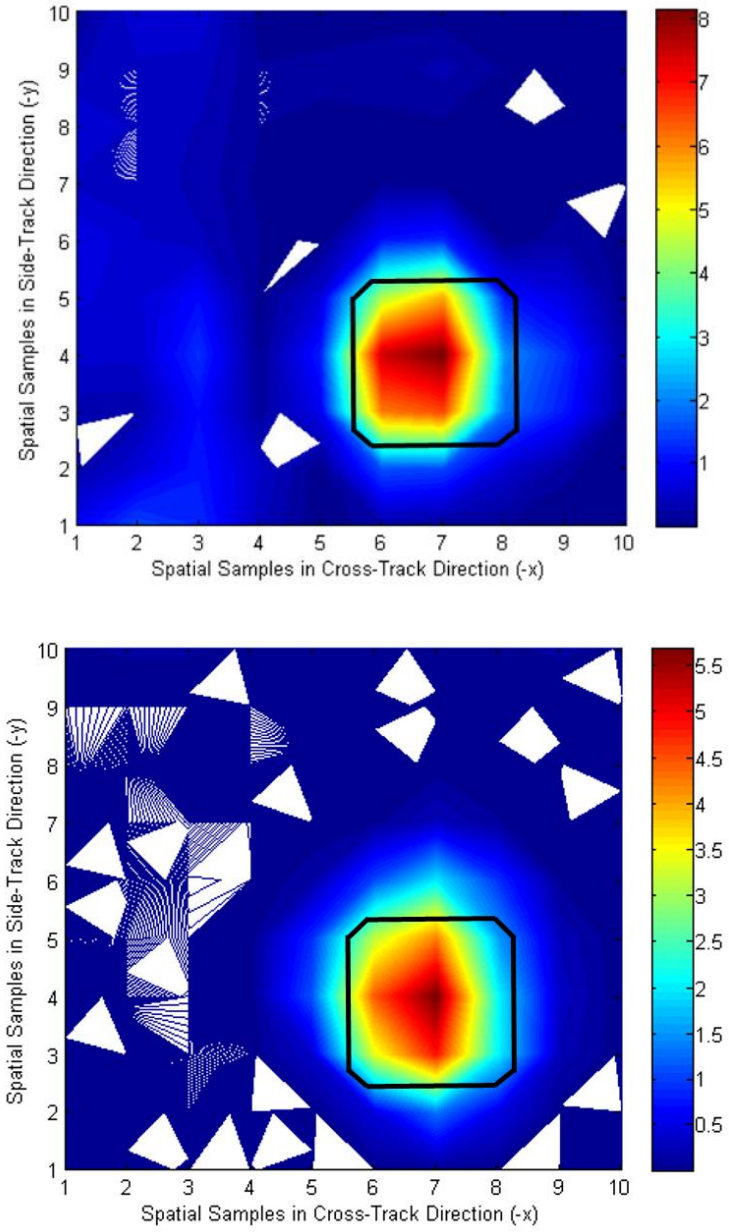

Figure 4.21. 2-D Microwave images of the buried target, (on the top) Metasurface integrated Vivaldi antenna measurement, (at the bottom) standard Vivaldi antenna measurement

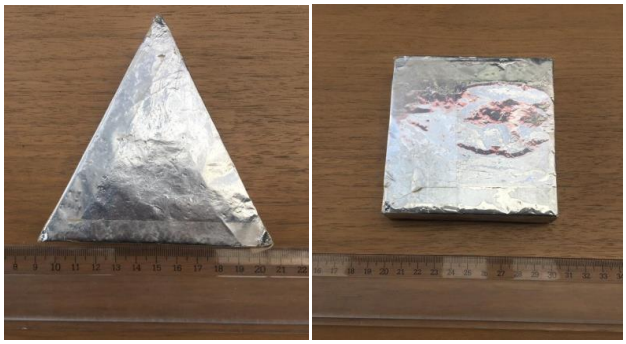

Figure 4.22. Aluminum folio covered cardboard objects as target

In the second experiment, two different conducting targets (a square shaped target and a triangular shaped target) are buried into fine soil in a measurement area of size 30x30cm. The square shaped target has 10cm side lengths while the triangular target's base length and height are both 10 cm. Targets are made of thin cardboard prisms which are covered by aluminum foil. The objects are buried 2 cm below the ground level. Antenna height with respect to ground level is 8 cm. Spatial sampling interval is 2 cm in both down-track and cross-track directions. The experiments are conducted in the same setup composed of the sandbox and network analyzer.

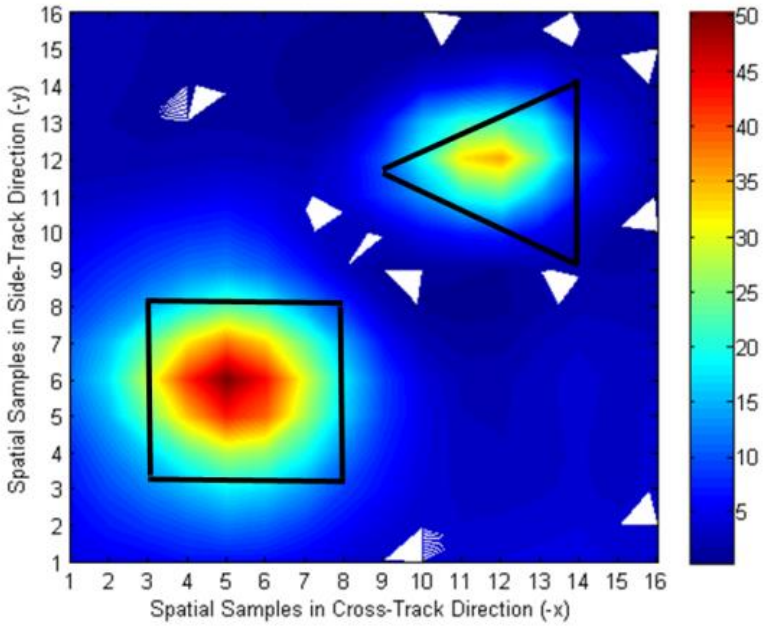

(a)

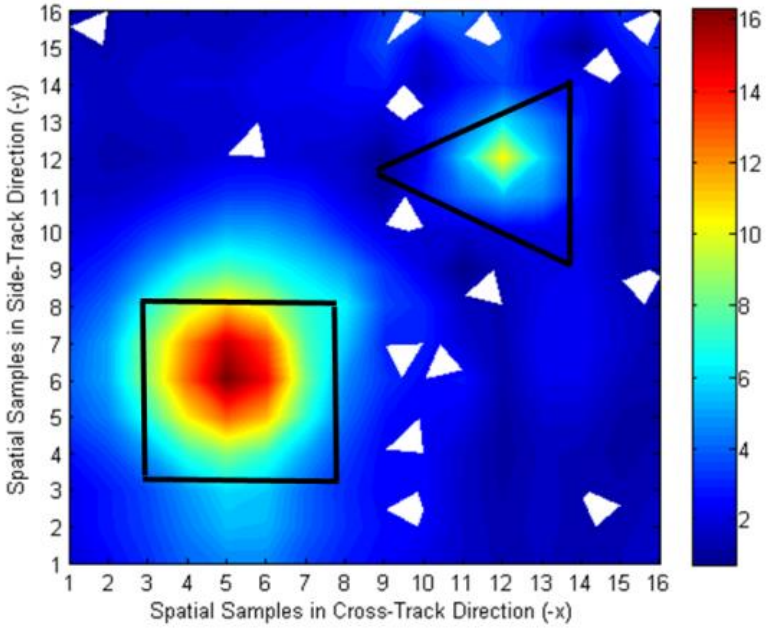

(b)

Figure 4.23. 2-D Microwave images of buried targets, (a) Metasurface integrated Vivaldi antenna measurement, (b) standard Vivaldi antenna measurement

Figure 4.23 displays the retrieved images of the targets using both standard and metasurface integrated antennas. Images obtained for the rectangular target is larger than the actual target size in both measurements. However, the triangular target is barely seen in the measurements taken by the standard Vivaldi antenna. On the other hand, image of the triangular target is captured by metamaterial lens integrated antenna with a larger footprint compared to the actual size of the object. Compared to results of the first experiments, image resolution obtained in the second experiment is dramatically reduced. Two main reasons may explain the deterioration experienced in these results. Firstly, aluminum foil is very thin (tens of microns) with respect to the incident wavelength. Therefore, surface currents are not excited as well as in the case of aluminum plate. As a result, reflected power levels are lower. Near the edges, reflection level is closer to ground reflection level which precludes detection of edges. Secondly, for the thin discs covered by aluminum film,

the edge diffractions are formed differently as compared to the solid metal plate of the first experiment, which has sharp edges and larger metal thickness.

When the metasurface integrated antenna is used in the measurements, the resolution of the target images are observed to improve noticeably due to both higher gain and smaller HPBW of this antenna as compared to image obtained by the standard Vivaldi antenna, as seen in Figure 4.23.

These results can be explained with the physical expectations since the antenna with a larger beamwidth can collect power from larger angles and distances. In this case, energy radiated by the antenna and reflected from the target can be received from farther away distances to the target which can result in the enlargement of the target's 2-D image size. Thus, we can conclude that the inclusion of the metasurface lens in the antenna design can improve the resolution of the microwave images.

CHAPTER 5

CONCLUSION

With the advent of the metamaterials, numerous microwave components including antennas are evolved and enhanced in terms of performance characteristics. Numerous applications utilize metamaterials to reduce antenna size, lower operation bandwidth and improve radiation pattern characteristics. Radiation characteristics of the sensors are critical factors for the resolution quality in image construction. Numerous imaging systems experience improper performance due to poor directivity characteristics of their antennas. In this thesis, a broadband metamaterial-inspired lensing device is designed to improve directivity characteristics of an ultra-wideband antenna, which is used for microwave imaging applications.

In Chapter 2 of the thesis, an ultra-wideband antenna (a standard antipodal Vivaldi antenna) with relatively average directivity characteristics is designed. This antenna is a traveling wave type antenna which can operate over very large bandwidths making it a candidate for wideband imaging applications. The antenna has a compact size and low weight. In this chapter, the parametric design of the antenna is given. Each physical parameter is investigated in terms of their effects over antenna performance characteristics such as the lower/higher end of operation bandwidth, radiation/total efficiency characteristics, half power beamwidth in E and H field planes and gain dispersion. Design iterations had been carried out until the optimum balance between the antenna performance and the physical size of the structure. Designed antipodal Vivaldi antenna is a compact sensor which can operate in 1-6 GHz designated operation bandwidth with high efficiency and medium directivity characteristics. In the first part of Chapter 3, the unit cell design for the metasurface lens is undertaken. Initially, three different unit cell topologies are chosen as candidate structures for the lens. Return and insertion loss characteristics are

calculated via commercial EM software CST. Afterwards, constitutive parameters of the unit cells are retrieved by a method based on scattering parameters which also makes use of the Kramers-Kronig relationship. Eigenmode analysis of the same structures is also performed and with the results of both methods are cross-checked to test the accuracy of the results. Constitutive parameters retrieved by both methods yielded very close results at frequencies far from the resonances of the metasurfaces. Later on, electric field, magnetic field and surface current distributions of the unit cells are inspected to understand the physical mechanism underlying unit cell's electromagnetic response which provided useful insight in the metasurface lens design. Then, the same procedure is repeated with a different unit cell orientation to characterize the response of the unit cell for varying incident field polarization. Later in the antenna design process, this analysis is used to decide about the unit cell orientation to be used in the metasurface lens.

In the second part of Chapter 3, the chosen unit cell topology is integrated into the designed antipodal Vivaldi antenna. The metasurface of unit cells and the antenna are printed over the same substrate which ensured to protect the compact size characteristics of the antenna design. Computational experiments provided information about the interaction mechanisms between unit cells and the radiated near field of the antenna. Electric field distributions of the antenna with and without metasurface lens are examined to understand how the inclusion of the metasurface lens produces a more directive radiation pattern. Later in this chapter, the effects of the unit cell topology and its orientation are inspected. Decision making in antenna design is based on the dispersion characteristics of the unit cell and its particular orientation to yield optimal results for antenna gain and directivity over the designated bandwidth. In the last part of this section, the geometry and physical size of the overall lens structure is studied. It was found that the metasurface lens requires an optimum width for the given antenna size. On the other hand, the directivity of the antenna increases proportional to the length of the lens. The overall

shape of the lens found to be immaterial concerning antenna performance as long as the length and width of the lens are adjusted correctly.

In the last chapter of the thesis, fabrication and measurement results of the designed antennas are given. Two identical antipodal Vivaldi antennas are fabricated by a laser etching method over dielectric substrates. Metasurface lens is integrated to one of the antennas and the performance of the two antennas are compared experimentally. The return losses of the antennas are measured by a network analyzer and their radiation characteristics are measured with a near-field anechoic chamber. Simulation and measurement results are found in good agreement indicating an increase in the directivity for the metasurface integrated antenna over the operation bandwidth of 1-6 GHz. Also, it was found that the metasurface lens does not deteriorate the efficiency characteristics of the antenna.

Lastly, microwave imaging of a metal plate buried under the soil is constructed using both antenna structures. Measurements are conducted in identical experimental setups where network analyzer is used as a transmitting and receiving unit which transferred measurement results to a computer database via a 3rd party software. Later, total energy of time signals measured at each spatial sampling point are obtained and processed to create a 2-D image of the buried targets. The image resolution of the targets obtained by the antenna with a metasurface lens yielded higher resolution compared to the standard antipodal Vivaldi antenna measurments. Thus, it has been shown that metamaterial loaded antennas can enhance the resolution of microwave imaging systems.

Future work of this thesis divides into two pathways. Unit cells with different EM properties such as having zero or negative index can be used antenna design to enhance capabilities of microwave imaging systems. Challenge in this research path is the characterization of the unit cell’s constitutive parameters correctly since most characterization methods fail to yield correct and physically acceptable results near and after the resonance frequency of the unit cell. The second pathway for the future

work is the application of the designed metasurface structure to different types of antennas. 3-D antenna structures such as aperture and wire antennas have potential for metamaterial application. Following a similar approach presented in this work, metamaterial lenses can be designed to enhance the radiation performance of various 3-D antennas for applications including subsurface imaging.

REFERENCES

[1] V. G. Veselago, "The electrodynamics of substances with simultaneously negative values of ε and μ," Sov Pyhs-Usp, vol. 10, no.4, pp. 509–514, 1968.

[2] J. B. Pendry, A. J. Holden, D. J. Robbins, and W. J. Stewart, "Low frequency plasmons in thin-wire structures," J. Phys. Condens. Matter, vol. 10, no. 22, pp. 4785-4809, 1998.

[3] J. B. Pendry, A. J. Holden, D. J. Robbins, and W. J. Stewart, "Magnetism from conductors and enhanced nonlinear phenomena," IEEE Trans. Microw. Theory Tech., vol. 47, no. 11, pp. 2075–2084, 1999.

[4] D. R. Smith, W. J. Padilla, D. C. Vier, S. C. Nemat-Nasser, and S. Schultz, "Composite medium with simultaneously negative permeability and permittivity," Phys. Rev. Lett., vol. 84, no. 18, pp. 4184–4187, 2000.

[5] R. A. Shelby, D. R. Smith, S. Schultz, "Experimental verification of a negative index of refraction," Science, vol. 292, no. 5514, pp. 77–79, 2001.

[6] D. R. Smith, D. C. Vier, W. Padilla, S. C. Nemat-Nasser, and S. Schultz, "Loopwire medium for investigating plasmons at microwave frequencies," Appl. Phys. Lett., vol. 75, no. 10, pp. 1425-1427, 1999.

[7] J. Huangfu, L. Ran, H. Chen, X. Zhang, K. Chen, T. M. Grzegorczyk, and J. A. Kong, "Experimental confirmation of negative refractive index of a metamaterial composed of Ω-like metallic patterns," Appl. Phys. Lett., vol. 84, no. 9, pp. 15371539, 2004.

[8] J. D. Baena, L. Jelinek, R. Marqués, and J. Zehentner, "Electrically small isotropic three-dimensional magnetic resonators for metamaterial design," Appl. Phys. Lett., vol. 88, no. 13, pp. 134108(1)-(3), 2006.

[9] Ekmekci and G. Turhan-Sayan, "Comparative investigation of resonance characteristics and electrical size of the double-sided SRR, BC-SRR and conventional SRR type metamaterials for varying substrate parameters," Progress In Electromagnetics Research B, Vol. 12, 35-62, January 2009.

[10] Ekmekci, K. Topalli, T. Akin and G. Turhan-Sayan, "A Tunable Multi-Band Metamaterial Design Using Micro-Split SRR Structures," Optics Express, Vol.17, No.18, pp.16046-16058, July 2009.

[11] Y. Z. Cheng, Y. Nie, Z. Z. Cheng, X. Wang, and R. Z. Gong, "Chiral metamaterials with giant optical activity and negative refractive index based on complementary conjugate-swastikas structure," J. Electromagn. Waves Appl., vol. 27, no. 8, pp. 1068–1076, 2013.

[12] H. Chen and C. T. Chan, “Acoustic cloaking in three dimensions using acoustic metamaterials,” Appl. Phys. Lett., vol. 91, no. 18, pp. 183518(1)-(3), 2007.

[13] Y. Wu and J. Li, “Total reflection and cloaking by zero index metamaterials loaded with rectangular dielectric defects,” Appl. Phys. Lett., vol. 102, no. 18, pp. 183105(1)-(4), 2013.

[14] J. B. Pendry, “Negative refraction makes a perfect lens,” Phys. Rev. Lett., vol. 85, no. 18, pp. 3966-3969, 2000.

[15] S. Xiao, Q. He, X. Huang, and L. Zhou, “Super imaging with a plasmonic metamaterial: Role of aperture shape,” Metamaterials, vol. 5, no. 2–3, pp. 112– 118, 2011

[16] R. W. Ziolkowski, P. Jin and C. Lin, "Metamaterial-inspired engineering of antennae," Proc IEEE, vol. 99, pp. 1720-1731, 2011.

[17] Nader Engheta and R. W. Ziolkowski, "A positive future for double-negative metamaterials," in IEEE Transactions on Microwave Theory and Techniques, vol. 53, no. 4, pp. 1535-1556, April 2005.

[18] R. W. Ziolkowski and A. D. Kipple, "Application of double negative materials to increase the power radiated by electrically small antennae," Antennae and Propagation, IEEE Transactions On, vol. 51, pp. 2626-2640, 2003.

[19] R. W. Ziolkowski and A. Erentok, "Metamaterial-based efficient electrically small antennae," Antennae and Propagation, IEEE Transactions On, vol. 54, pp. 2113-2130, 2006.

[20] A. Erentok and R. W. Ziolkowski, "Metamaterial-inspired efficient electrically small antennae," Antennae and Propagation, IEEE Transactions On, vol. 56, pp. 691-707, 2008.

[21] R. Greegor, C. Parazzoli, J. A. Nielsen, M. H. Tanielian, D. Vier, S. Schultz, C. L. Holloway and R. W. Ziolkowski, "Demonstration of impedance matching using a mu-negative (MNG) metamaterial," Antennae and Wireless Propagation Letters, IEEE, vol. 8, pp. 92-95, 2009.

[22] H. R. Stuart and A. D. Yaghjian, "Approaching the lower bounds on Q for electrically small electric-dipole antennae using high permeability shells," Antennae and Propagation, IEEE Transactions On, vol. 58, pp. 38653872, 2010.

[23] S. R. Best, "Low Q electrically small linear and elliptical polarized spherical dipole antennae," Antennae and Propagation, IEEE Transactions On, vol. 53, pp. 1047-1053, 2005.

[24] A. Sanada, M. Kimura, I. Awai, C. Caloz and T. Itoh, "A planar zeroth-order resonator antenna using a left-handed transmission line," in Microwave Conference, 2004. 34th European, 2004, pp. 1341-1344.

[25] A. Lai, K. M. Leong and T. Itoh, "Infinite wavelength resonant antennae with monopolar radiation pattern based on periodic structures," Antennae and Propagation, IEEE Transactions On, vol. 55, pp. 868-876, 2007.

[26] M. A. Antoniades and G. V. Eleftheriades, "A folded-monopole model for electrically small NRI-TL metamaterial antennae," Antennae and Wireless Propagation Letters, IEEE, vol. 7, pp. 425-428, 2008.

[27] Y. Dong, H. Toyao and T. Itoh, "Compact Circularly-Polarized Patch Antenna Loaded With Metamaterial Structures," in IEEE Transactions on Antennas and Propagation, vol. 59, no. 11, pp. 4329-4333, Nov. 2011.

[28] Fan Yang and Y. Rahmat-Samii, "Reflection phase characterizations of the EBG ground plane for low profile wire antenna applications," IEEE Transactions on Antennae and Propagation, vol. 51, pp. 2691-2703, 2003.

[29] A. E. Lamminen, A. R. Vimpari and J. Saily, "UC-EBG on LTCC for 60GHz frequency band antenna applications," Antennae and Propagation, IEEE Transactions On, vol. 57, pp. 2904-2912, 2009.

[30] Y. Dong, H. Toyao and T. Itoh, "Miniaturized zeroth order resonance antenna over a reactive impedance surface," 2011 International Workshop on Antenna Technology (iWAT), Hong Kong, 2011, pp. 58-61.

[31] F. Yang, K. Ma, Y. Qian and T. Itoh, "A uniplanar compact photonicbandgap (UC-PBG) structure and its applications for microwave circuit," Microwave Theory and Techniques, IEEE Transactions On, vol. 47, pp. 1509-1514, 1999.

[32] D. Sievenpiper, Lijun Zhang, R. F. J. Broas, N. G. Alexopolous and E. Yablonovitch, "High-impedance electromagnetic surfaces with a forbidden frequency band," IEEE Trans. Microwave Theory Tech., vol. 47, pp. 2059-2074, 1999.

[33] H. Mosallaei and K. Sarabandi, "Antenna miniaturization and bandwidth enhancement using a reactive impedance substrate," Antenna and Propagation, IEEE Transactions On, vol. 52, pp. 2403-2414, 2004.

[34] A. P. Feresidis, G. Goussetis, S. Wang and J. C. Vardaxoglou, "Artificial magnetic conductor surfaces and their application to low-profile high-gain planar antennae," Antennae and Propagation, IEEE Transactions On, vol. 53, pp. 209215, 2005.

[35] M. Moosazadeh, S. Kharkovsky,J. T. Case, and B. Samali, “Miniaturized UWB antipodal Vivaldi antenna and its application for detection of void inside concrete specimens,”IEEEAntennasWirelessPropag.Lett.,vol.16, pp. 1317–1320, 2017.

[36] I. T. Nassar and T. M. Weller, “A novel method for improving antipodal Vivaldi antenna performance,” IEEE Trans. Antennas Propag., vol. 63, no. 7, pp. 3321–3324, Jul. 2015.

[37] B. Zhou, H. Li, X. Y. Zou, and T. J. Cui, “Broadband and high gain planar Vivaldi antennas based on inhomogeneous anistropic zero index metamaterial,” Prog. Electromagn. Res., vol. 120, pp. 235–247, 2011

[38]A.R.H.Alhawari,A.Ismail,M.A.Mahdi,andR.S.A.R.Abdullah,“Antipodal Vivaldi antenna performance booster exploiting sung-in negative index metamaterial,” Prog. Electromagn. Res. C, vol. 27, pp. 265–279, 2012.

[39] C.Balanis, "Antenna theory-analysis and design", John Wiley &Sons Inc. , pp.533-534 , 2016.

[40] T.A. Milligan, "Modern Antenna Design." John Wiley &Sons Inc. , pp.475-481 , 2005.

[41] R.Q. Lee and R.N. Simons, “Advances in Microstrip and Printed Antennas”, John Wiley &Sons Inc, 1997.

[42] K. S. Yngvesson, T. L. Korzeniowski, Y. -. Kim, E. L. Kollberg and J. F. Johansson, "The tapered slot antenna-a new integrated element for millimeter-wave applications," in IEEE Transactions on Microwave Theory and Techniques, vol. 37, no. 2, pp. 365-374, Feb. 1989.

[43] P. J. Gibson, "The Vivaldi Aerial," 1979 9th European Microwave Conference, Brighton, UK, 1979, pp. 101-105.

[44] H. Holter, "Dual-Polarized Broadband Array Antenna With BOR-Elements, Mechanical Design and Measurements," in IEEE Transactions on Antennas and Propagation, vol. 55, no. 2, pp. 305-312, Feb. 2007.

[45] R. W. Kindt and W. R. Pickles, "Ultrawideband All-Metal Flared-Notch Array Radiator," in IEEE Transactions on Antennas and Propagation, vol. 58, no. 11, pp. 3568-3575, Nov. 2010.

[46] L. R. Lewis, M. Fasset and J. Hunt, “A Broadband Stripline Array Element,” IEEE Antennas Propagat. Symposium Digest, pp. 335–337, 1974.

[47] W. F. Croswell, T. Durham, M. Jones, D. Schaubert, P. Friedrich and J. G. Maloney, “Wideband Arrays,” Chapter 12 in Modern Antenna Handbook (C. A. Balanis, editor), John Wiley & Sons, Publishers, 2008.

[48] E. Gazit, “Improved Design of the Vivaldi Antenna,” IEE Proceedings Microwaves, Antennas and Propagation, Vol. 135, No. 2, pp. 89–92, April 1988.

[49] J. D. S. Langley, P. S. Hall and P. Newham, "Novel ultrawide-bandwidth Vivaldi antenna with low cross polarization," in Electronics Letters, vol. 29, no. 23, pp. 2004-2005, 11 Nov. 1993.

[50] Jian Zhang, Xiaoxing Zhang, and Song Xiao, "Antipodal Vivaldi Antenna to Detect UHF Signals That Leaked Out of the Joint of a Transformer", International

Journal of Antennas and Propagation, vol. 2017, Article ID 9627649, 13 pages, 2017.

[51] N. Hamzah and K. A. Othman, "Designing Vivaldi antenna with various sizes using CST software", Proceeding of the World Congress on Engineering (WCE 2011), London – UK, 1-5, 2011.

[52] Y. W. Wang, G. M. Wang and B. F. Zong, "Directivity improvement of Vivaldi antenna using double-slot structure", IEEE Antennas and Wireless Propagation Letters,12, 1380–1383, 2013.

[53] T. Namas and M. Hasanovic, "Ultrawideband antipodal Vivaldi antenna for road surface scanner based on inverse scattering", Proc. 28th Annual Review of Progress in Applied Computational Electromagnetics, Columbus, Ohio, USA, 882–887, 2012.

[54] A. Dastranj, "Wideband antipodal Vivaldi antenna with enhanced radiation parameters" IET Microwave, Antennas and Propagation", 9(15), 1755–1760, 2015.

[55] A. Molaei, M. Kaboli, S. A. Mirtaheri and S. Abrishamian, "Beam-tilting improvement of balanced antipodal vivaldi antenna using a dielectric lens", Proc. 2nd Iranian Conference on Engineering Electromagnetics, Tehran, Iran, 577–581, 2014.

[56] P. Fei, Y. C. Jiao, W. Hu and F. S. Zhang, "A miniaturized antipodal Vivaldi antenna with improved radiation characteristics", IEEE Antenna and Wireless Propagation Letters, 10, 127–130, 2011.

[57] A. Molaei, M. Kaboli, S. A. Mirtaheri, and M. S. Abrishamian, "Dielectric lens balanced antipodal Vivaldi antenna with low cross-polarization for ultra-wideband applications", Institution of Engineering and Technology (IET), Microwaves, Antennas & Propagation, 8(14), 1137–1142, 2014.

[58] J. Bourqui, M. Okoniewski and E. Fear, "Dielectric director for near-field microwave imaging", Proc. 3rd European Conference on Antennas and Propagation, Berlin, Germany, 3327–3330, 2009.

[59] J. Bourqui, M. Okoniewski and E. Fear, "Enhanced directivity of a tapered slot antenna for near-field imaging", 13th International Symposium on Antenna Technology and Applied Electromagnetics and the Canadian Sciences Meeting, Toronto, ON, 1–3, 2009.

[60] R. Herzi, H. Zairi, and A. Gharsallah, "Antipodal Vivaldi antenna array with high gain and reduced mutual coupling for UWB applications", Proc. 16th International Conference on Sciences and Techniques of Automatic Control and Computer Engineering, Monastir, Tunisia, 789–792, 2015.

[61] I. T. Nassar and T. M. Weller, "A novel method for improving antipodal Vivaldi antenna performance", IEEE Transactions on Antennas and Propagation, 63(7), 3321–3324, 2015.

[62] Z. Li, X. Kang, J. Su, Q. Gua, Y. Yang and J. Wang, "A Wideband End-Fire Conformal Vivaldi Antenna Array Mounted on a Dielectric Cone", International Journal of Antennas and Propagation, 1–11, 2016.

[63] L. Li, X. Xia, Y. Liu and T. Yang, "Wideband balanced antipodal Vivaldi antenna with Enhanced radiation parameters", Progress In Electromagnetics Research C, 66, 163–171, 2016.

[64] N. Tevar, P. Mehta and K. Bhatt, "A review paper on conical corrugated horn antenna, Proc. IEEE International Conference on Wireless Communications", Signal Processing and Networking, Chennai, India, 889–892, 2016.

[65] T.J. Huang, C.Y. Chiang and H.T. Hsu, "Effect of corrugation profiles on the improvement of front-to-back ration for dual exponentially tapered slot antennas (DETSA)", Proc. of the Asia-Pacific Microwave Conference, Melbourne, Australia, 685–688, 2011.

[66] M. Moosazadeh and S. Kharkovsky, "Design of ultra-wideband antipodal Vivaldi antenna for microwave imaging applications", Proc. IEEE International Conference on Ubiquitous wireless Broadband, 1–4, 2015.

[67] A. M. De Oliveira, M. B. Perotoni, S. T. Kofuji, and J. F. Justo, "A palm tree antipodal Vivaldi antenna with exponential slot edge for improved radiation pattern", IEEE Antennas and Wireless Propagation Letters, 14, 1334–1337, 2015.

[68] X. Kang and Z. Li, "A modified UWB antipodal Vivaldi antenna with improved radiation characteristics", Proc. 6Th IEEE International Symposium on Microwave, Antenna, Propagation and EMC Technologies, Shanghai, China, 120–122, 2015.

[69] R. Singha and D. Vakula, "Corrugated antipodal Vivaldi antenna using spiral shape negative index metamaterial for ultra-wideband application," 2015 International Conference on Signal Processing and Communication Engineering Systems, Guntur, pp. 179-183, 2015.

[70] G. K. Pandey, H. S. Singh, P. K. Bharti, A. Pandey, and M. K. Meshram, "High gain Vivaldi antenna for radar and microwave imaging applications", International Journal of Signal Processing Systems, 3(1), 35–39, 2015.

[71] L. Yao, J. Xiao, H. Zhu, N. Li and X. Li, "A high gain UWB Vivaldi antenna with band notched using capacitive loaded loop (CLL) resonators", IEEE International Conference on Microwave and Millimeter wave Technology, 2, 820–822, 2016.

[72] T.J. Huang and H. T. Hsu, "Antipodal dual exponentially tapered slot antenna (DETSA) with stepped edge corrugations for front-to-back ration improvement", International Workshop on Electromagnetics, Applications and Student Innovation, Taipei, Taiwan, 45–51, 2011.

[73] Y. Yang, Y. Wang, and A. E. Fathy, "Design of Compact Vivaldi Antenna Arrays for UWB See through Wall Applications", Progress In Electromagnetics Research, Vol. 82, 401-418, 2008.

[74] Xianming Qing, Zhi Ning Chen, and Michael Yan Wah Chia, "Parametric Study of Ultra-Wideband Dual Elliptically Tapered Antipodal Slot Antenna", International Journal of Antennas and Propagation, vol. 2008, 267197, February 2008.

[75] J. Shan, A. Xu and J. Lin, "A parametric study of microstrip-fed Vivaldi antenna", 2017 3rd IEEE International Conference on Computer and Communications (ICCC), Chengdu, pp. 1099-1103, 2017.

[76] Cui, TJ, Smith, DR, and Liu, R. "Metamaterials: Theory, design, and applications.", December 2010.

[77] Alù, A. "First-principles homogenization theory for periodic metamaterials", Phys. Rev. B 84, 075153, 2011.

[78] J. D. Jackson. "Classical Electrodynamics. John Wiley and Sons", New York, NY, 3rd edition, 1999.

[79] Silveirinha, Mario & Belov, Pavel , “Spatial dispersion in lattices of split ring resonators with permeability near zero”, Phys. Rev. B. 77, 2008.

[80] Alù, Andrea, "First-Principle Homogenization Theory for Periodic Metamaterials", Phys. Rev. B. 84, 2010.

[81] O'Brien, S & B Pendry, J., "Magnetic activity at infrared frequencies in structured metallic photonic crystals", Journal of Physics: Condensed Matter. 14. 6383, 2002.

[82] R Smith, D & C Vier, D & Koschny, Th & Soukoulis, Costas, "Electromagnetic Parameter Retrieval from Inhomogeneous Metamaterials", Physical review. E, Statistical, nonlinear and soft matter physics, 71, 036617, 2005.

[83] Koschny, T., Markos, P., Smith, D., and Soukoulis, C., “Resonant and antiresonant frequency dependence of the effective parameters of metamaterials,” Phys. Rev. E 68(6), 065602, 2003.

[84] Depine, Ricardo & Lakhtkia, A., "Comment I on "Resonant and antiresonant frequency dependence of the effective parameters of metamaterials". Physical Review E. 70, 048601, 2004.

[85] L. Landau, E. Lifschitz, "Electrodynamics of Continuous Media", Butterworth-Heinemann, 1984.

[86] D.A. Powell, Y.S. Kivshar, "Substrate-induced bianisotropy in metamaterials", Appl. Phys. Lett. 97, 2010.

[87] Alù, A., "Restoring the physical meaning of metamaterial constitutive parameters", Phys. Rev. B, 83, 081102, 2011.

[88] C.R. Simovski, S. He, "Frequency range and explicit expressions for negative permittivity and permeability for an isotropic medium formed by a lattice of perfectly conducting Ω particles", Appl. Phys. Lett. 311, 254–263, 2003.

[89] C. Fietz and G. Shvets, "Current-driven metamaterial homogenization", Physica B 405, 2930, 2010.

[90] C. R. Simovski, "Material parameters of metamaterials: A review," Opt. Spectrosc., vol. 107, no. 5, pp. 726–753, 2009.

[91] Scher, A. D. and E. F. Kuester, "Extracting the bulk effective parameters of a metamaterial via the scattering from a single planar array of particles," Metamaterials, Vol. 3, No. 1, 44–55, 2009.

[92] Silveirinha, M. G., "Generalized Lorentz-Lorentz formulas for microstructured materials," Phys. Rev. B, Vol. 76, No. 24, 245117, 2007.

[93] V. M. Agranovich and V. Ginzburg, "Spatial Dispersion in Crystal Optics and the Theory of Excitons", Willey-Interscience, New York, 1966.

[94] Z. Szabo, G. Park, R. Hedge and E. Li, "A Unique Extraction of Metamaterial Parameters Based on Kramers–Kronig Relationship," in IEEE Transactions on Microwave Theory and Techniques, vol. 58, no. 10, pp. 2646-2653, Oct. 2010.

[95] Smith S., Glenn S., and Waymond R.S., "A scale model for studying ground penetrating radars", IEEE transactions on geoscience and remote sensing 27(4), 358-363, 1989.

[96] Verma P. K., Gaikwad A. N., Singh D., and Nigam M. J., "Analysis of clutter reduction techniques for through wall imaging in UWB range," Progress In Electromagnetics Research B, vol. 17, 29-48, 2009.

[97] Turhan-Sayan, Gonul & Doğan, Mesut & Yeşilyurt, Ömer, "Inside-the-wall detection of objects with low metal content using the GPR sensor: effects of different wall structures on the detection performance", 2. 10.1117/12.2304611, 2018.

[98] Kadir Üstün and Gönül Turhan-Sayan, "Ultra-broadband long-wavelength infrared metamaterial absorber based on a double-layer metasurface structure," J. Opt. Soc. Am. B 34, 456-462, 2017.

[99] Kadir Üstün and Gönül Turhan-Sayan, "Broadband LWIR and MWIR metamaterial absorbers with a simple design topology: almost perfect absorption and super-octave band operation in MWIR band", J. Opt. Soc. Am. B 34, D86-D94, 2017.

[100] O. Turkmen, G. Turhan-Sayan and R. W. Ziolkowski, "Metamaterial inspired, electrically small, GSM antenna with steerable radiation patterns and high radiation efficiency", 2013 IEEE Antennas and Propagation Society International Symposium (APSURSI), Orlando, FL, pp. 770-771, 2013.

[101] Turkmen, O. , Turhan- Sayan, G. and Ziolkowski, R. W., "Single- , dual- , and triple- band metamaterial- inspired electrically small planar magnetic dipole antennas", Microw. Opt. Technol. Lett., 56: 83-87, 2014.

[102] M. Dogan and G. Turhan-Sayan, "Investigation of simulated ground penetrating radar data for buried objects using quadratic time-frequency transformations", 2017 IEEE International Symposium on Antennas and Propagation & USNC/URSI National Radio Science Meeting, San Diego, CA, pp. 235-236, 2017.

[103] M. Dogan and G. Turhan-Sayan, "Investigation of the effects of buried object orientation in subsurface target detection by GPR", 2017 7th IEEE International Symposium on Microwave, Antenna, Propagation, and EMC Technologies (MAPE), Xi'an, pp. 475-479, 2017.

[104] Mesut Dogan, Gonul Turhan-Sayan, "Preprocessing of A-scan GPR data based on energy features", Proc. SPIE 9823, Detection and Sensing of Mines, Explosive Objects, and Obscured Targets XXI, 98231E, 2016.

[105] Turhan-Sayan, Gonul, "K pulse estimation and target identification", Electronic Thesis or Dissertation. Ohio State University, OhioLINK Electronic Theses and Dissertations, 1988.

[106] (2018). CST Studio Suite . Computer Simulation Technologies. [Online]. Available: https://www.cst.com/products/csts2 (Last accessed on December, 2018)